

DEVELOPMENT AND CHARACTERIZATION OF LOW-COST UNCOOLED
INFRARED SENSORS FOR COMMERCIAL APPLICATIONS

A THESIS SUBMITTED TO
THE GRADUATE SCHOOL OF NATURAL AND APPLIED SCIENCES
OF
MIDDLE EAST TECHNICAL UNIVERSITY

BY

FIRAT TANKUT

IN PARTIAL FULLFILLMENT OF THE REQUIREMENTS
FOR
THE DEGREE OF MASTER OF SCIENCE
IN
ELECTRICAL AND ELECTRONICS ENGINEERING

SEPTEMBER 2013

Approval of the thesis:

**DEVELOPMENT AND CHARACTERIZATION OF LOW-COST UNCOOLED
INFRARED SENSORS FOR COMMERCIAL APPLICATIONS**

submitted by **FIRAT TANKUT** in partial fulfillment of the requirements for the degree of
**Master of Science in Electrical and Electronics Engineering, Middle East Technical
University** by,

Prof. Dr. Canan Özgen
Dean, Graduate School of **Natural and Applied Sciences**

Prof. Dr. Gönül Turhan Sayan
Head of Department, **Electrical and Electronics Eng.**

Prof. Dr. Tayfun Akın
Supervisor, **Electrical and Electronics Eng. Dept., METU**

Dr. Selim Eminoğlu
Co-Supervisor, **Mikro-Tasarım San. ve Tic. Ltd. Şti.**

Examining Committee Members

Prof. Dr. Cengiz Beşikçi
Electrical and Electronics Eng. Dept., METU

Prof. Dr. Tayfun Akın
Electrical and Electronics Eng. Dept., METU

Dr. Selim Eminoğlu
Mikro-Tasarım San. ve Tic. Ltd. Şti.

Assoc. Prof. Dr. Haluk Külâh
Electrical and Electronics Eng. Dept., METU

Asst. Prof. Dr. Ali Kemal Okyay
Electrical and Electronics Eng. Dept., Bilkent University

Date: 03.09.2013

I hereby declare that all information in this document has been obtained and presented in accordance with academic rules and ethical conduct. I also declare that, as required by these rules and conduct, I have fully cited and referenced all material and results that are not original to this work.

Name, Last name: Fırat TANKUT

Signature:

ABSTRACT

DEVELOPMENT AND CHARACTERIZATION OF LOW-COST UNCOOLED INFRARED SENSORS FOR COMMERCIAL APPLICATIONS

Tankut, Fırat

M. Sc., Department of Electrical and Electronics Engineering

Supervisor: Prof. Dr. Tayfun Akin

Co-Supervisor: Dr. Selim Eminođlu

September 2013, 83 pages

This thesis reports the study on the development and characterization of low-cost uncooled microbolometer type infrared detectors, which are fabricated using standard CMOS and MEMS processes. Characterization of the detectors is the first step of developing infrared sensors with better performance. The characterized pixel has a 70 μm pitch and includes 4 serially connected diodes as the detector circuit. Thermal conductance (G_{th}), temperature sensitivity (TC) and, optical absorption are measured in scope of the characterization tests. The optical absorption of the detectors is measured by Fourier Transform Infrared Spectroscopy (FTIR) method and average absorption is found as 78 % for 7-14 μm wavelength range. The noise of the detector is characterized in detail. Test results show that, the predominant noise mechanism in the characterized low-cost infrared sensors is the Random Telegraph Signal (RTS) noise.

After characterizing the pixel, the readout electronics of the 70 μm pixel pitch QCIF (160x120) resolution Focal Plane Array (FPA) are improved for better performance. Three main revisions on the current design are made, and the revised readout circuits are verified with detailed tests in the scope of this thesis. In the first revision, power dissipation of the chip is decreased by changing the architecture of various blocks of the readout circuit. After this revision, the Noise Equivalent Temperature Difference (NETD) value is

improved to 280 mK. The second design revision decreased the impact of the column noise that was caused by the RTS mechanism. Lastly, a third revision is made in order to improve the temperature stability and noise rejection. These revised sensors are used in developing miniature thermal camera systems in the scope of another work, and the resulting miniature cameras are among the smallest thermal camera cores in the world.

As the final step, second generation low-cost uncooled microbolometer pixels are developed, where the pixel pitch is reduced to 50 μm while preserving the same performance level as the 70 μm pixels. In order to alleviate the performance degradation caused by the reduction of the area that absorbs radiation, more serially connected detector diodes and thinner support arms are used. Thermal parameters are simulated using Finite Element Method (FEM). The expected thermal conductance and the thermal time constant are calculated as 222 nW/K and 48.8 ms respectively from the simulations. Optical absorption is also simulated and the average optical absorption is calculated to be 77 % for 7-14 μm wavelength region from the simulations. The FPA chip utilizing second generation pixels is tested, and average pixel noise is measured as 9.8 μV_{RMS} including the readout circuit noise.

Keywords: uncooled infrared detectors, commercial infrared imaging, microbolometer characterization, low-cost microbolometers, microbolometer readout electronics

ÖZ

TİCARİ UYGULAMALAR İÇİN DÜŞÜK MALİYETLİ SOĞUTMASIZ KIZILÖTESİ ALGILAYICILARIN GELİŞTİRİLMESİ VE KARAKTERİZASYONU

Tankut, Fırat

Yüksek Lisans, Elektrik ve Elektronik Mühendisliği Bölümü

Tez Yöneticisi: Prof. Dr. Tayfun Akın
Ortak Tez Yöneticisi: Dr. Selim Eminoğlu

Eylül 2013, 83 sayfa

Bu tez, standart CMOS ve MEMS süreçleri kullanılarak üretilen mikrobolometre tipi soğutmasız kızılötesi algılayıcıların karakterizasyonu ve geliştirilmesi için yapılan çalışmaları rapor etmektedir. Detektörlerin karakterizasyonu, daha iyi performanslı kızılötesi algılayıcıların geliştirilmesi için ilk adımdır. Karakterize edilen piksel 70 µm büyüklüğündedir ve detektör devresi olarak 4 adet seri bağlanmış diyot içermektedir. Karakterizasyon testleri kapsamında, ısıl iletkenlik (G_{th}), sıcaklık hassasiyeti (TC) ve optik emilim ölçülmüştür. Detektörlerin optik emilimleri Fourier Dönüşüm Kızılötesi Spektroskopisi (FTIR) metodu ile ölçülmüştür ve ortalama emilim 7-14 µm dalga boyu aralığı için %78 olarak bulunmuştur. Detektör gürültüsü detaylıca karakterize edilmiştir. Test sonuçları göstermektedir ki, karakterize edilen düşük maliyetli detektörlerde baskın gürültü mekanizması Rastgele Telgraf Sinyali (RTS) gürültüsüdür.

Piksel karakterizasyonundan sonra, daha iyi performans için 70 µm piksel büyüklüğüne sahip QCIF (160x120) çözünürlüğündeki Odak Düzlem Matrisi'nin (FPA) okuma elektronikleri iyileştirilmiştir. Bu tez kapsamında, mevcut tasarım üzerinde üç ana revizyon gerçekleştirilmiş ve revize edilen okuma devrelerinin çalışmaları detaylı testler ile doğrulanmıştır. İlk revizyonda yonganın güç tüketimi okuma devrelerindeki çeşitli blokların mimarileri değiştirilerek düşürülmüştür. Bu revizyondan sonra, Gürültü Eşlenikli

Sıcaklık Farkı (NETD) 280 mK olarak elde edilmiştir. İkinci tasarım revizyonu, RTS mekanizmasının sebep olduğu sütun gürültüsünün etkisini azaltmıştır. Son olarak, ısı kararlılığı ve sistem gürültü reddini iyileştirmek amacıyla üçüncü revizyon gerçekleştirilmiştir. Revize edilen bu algılayıcılar, başka bir çalışma kapsamında, minyatür termal kamera geliştirilmesinde kullanılmıştır ve sonuçlanan minyatür kamera, dünyanın en küçük termal kamera çekirdeklerinden biridir.

Son basamak olarak, ikinci nesil düşük maliyetli soğutmasız mikrobolometre pikselleri tasarlanmıştır. 70 μm pikseller ile aynı performans seviyesi korunarak, piksel büyüklüğü 50 μm 'a düşürülmüştür. Küçülen ışıma emen alanın neden olduğu performans düşüşünü karşılamak için, seri bağlı detektör diyotlar artırılmış ve daha ince destek kolları kullanılmıştır. Isıl parametreler, Sonlu Eleman Metodu (FEM) kullanılarak simüle edilmiştir. Simülasyonlardan, beklenen ısı iletkenlik ve ısı zaman sabiti, sırasıyla 222 nW/K ve 48.8 ms olarak hesaplanmıştır. Ayrıca, optik emilim de simüle edilmiş ve simülasyonlardan ortalama emilim 7-14 μm dalgaboyu aralığı için %77 olarak hesaplanmıştır. İkinci jenerasyon pikselleri kullanan FPA yongası test edilmiş ve ortalama piksel gürültüsü okuma devreleri dahil 9.8 μV_{RMS} olarak bulunmuştur.

Anahtar Kelimeler: soğutmasız kızılötesi detektörler, ticari kızılötesi görüntüleme, mikrobolometre karakterizasyonu, düşük maliyetli mikrobolometreler, mikrobolometre okuma devreleri

To my parents,

ACKNOWLEDGEMENTS

First and foremost, I would like to express my sincere gratitude and appreciation to my advisor Prof. Dr. Tayfun Akin and my co-advisor Dr. Selim Eminođlu for their guidance and supervision throughout my thesis study. Working with them is a great opportunity.

I am very grateful to Dr. Murat Tepegöz for his tremendous assistance and guidance to me in every part of this study.

I would like to thank Orhan Akar and Asst. Prof. Dr. Yusuf Tanrikulu for their efforts in cleanroom processes.

I would like to thank Dinçay Akçören for sharing his experience and knowledge.

I would like to thank Alper Küçükkömürler and Ceren Tüfekçi for their help during testing. I would like to thank Zafer Zambođlu for his suggestions. I would like to thank Cavid Musayev and Nihan Eminođlu for providing a pleasant working environment and their moral support.

I would like to thank Şeniz Esra Küçük and Ozan Ertürk for their help during my simulations.

A special thanks to all members of MikroSens and METU-MEMS for their invaluable friendship.

Finally, yet importantly, I would like to express my deepest thanks to my beloved parents Sibel and Mehmet Tankut for their continuous encouragement, support, and assistance through all my life.

TABLE OF CONTENTS

ABSTRACT	v
ÖZ.....	vii
ACKNOWLEDGEMENTS	x
TABLE OF CONTENTS	xi
LIST OF FIGURES.....	xiii
LIST OF TABLES	xvi
1. INTRODUCTION.....	1
1.1. Uncooled Thermal Detectors	2
1.1.1. Microbolometers	2
1.1.2. Thermopile Detectors.....	5
1.1.3. Pyroelectric Detectors	5
1.2. Low-Cost Uncooled Thermal Imaging	6
1.2.1. Detector Fabrication.....	6
1.2.2. Vacuum Packaging	8
1.2.3. Miniature Camera	9
1.3. Performance Parameters	10
1.3.1. Temperature Sensitivity (TC)	10
1.3.2. Responsivity.....	11
1.3.3. Noise Equivalent Temperature Difference (NETD)	13
1.4. Research Objectives and Thesis Organization.....	13
2. PIXEL CHARACTERIZATION OF FIRST GENERATION LOW-COST INFRARED SENSORS	15
2.1. Current-Voltage (I-V) Characterization.....	16
2.2. Temperature Sensitivity (TC) Measurement.....	18
2.3. Thermal Conductance Measurement.....	19
2.4. Absorption Measurement	21
2.5. Detector Noise Characterization	23
2.5.1. Theory	23
2.5.2. Test Setup.....	28
2.5.3. Frequency Domain Measurement Results	30

2.5.4.	Time Domain Measurement Results	36
2.5.5.	Wafer Level RTS Noise Test	43
2.6.	Conclusion.....	45
3.	DEVELOPMENT AND TESTS OF FIRST GENERATION LOW-COST SENSOR ARRAY READOUT ELECTRONICS	47
3.1.	First Generation 160x120 Low-Cost Sensor	48
3.2.	First Design Revision for 160x120 Low-Cost Sensor.....	49
3.2.1.	Power Dissipation Optimization.....	50
3.2.2.	Test Setup & Results	51
3.3.	Second Design Revision for 160x120 Low-Cost Sensor	56
3.4.	Third Design Revision for 160x120 Low-Cost Sensor	59
3.5.	Summary of Revisions	60
4.	DEVELOPMENT OF SECOND GENERATION LOW-COST INFRARED SENSORS	63
4.1.	Pixel Optimization and Design.....	64
4.1.1.	Diode Number Optimization	64
4.1.2.	Pixel Pitch Optimization	65
4.1.3.	Pixel Layout Design and Cross Section	68
4.2.	Pixel Simulations.....	69
4.2.1.	Electrical Simulation	69
4.2.2.	Temperature Sensitivity Simulation	70
4.2.3.	Noise Simulation	71
4.2.4.	Thermal Simulation.....	72
4.2.5.	Optical Simulation.....	73
4.3.	Test Results	75
4.3.1.	Single Pixel I-V Test	75
4.3.2.	FPA Sensor Tests	76
4.4.	Conclusion.....	77
5.	CONCLUSIONS AND FUTURE WORK	79
	REFERENCES	81

LIST OF FIGURES

FIGURES

Figure 1.1: A representative drawing of a microbolometer detector pixel [9].	2
Figure 1.2: Cross sectional drawings of SOI Diode microbolometer pixels developed by Mitsubishi; (a) 40 μm pixel with absorber layer [14] (b) 25 μm pixel with absorber and independent reflector layer [15].	4
Figure 1.3: Representative drawing of a microcantilever thermopile detector [15].	5
Figure 1.4: SEM image of the 320x240 pyroelectric FPA developed by Raytheon [20].	6
Figure 1.5: Simplified diagram for process steps: (a) Pixel before Post-CMOS processing (b) DRIE etching of the oxide gaps using Metal-3 layer as mask (c) Metal layer stripping and pixel releasing by TMAH etching of the silicon handle wafer.	7
Figure 1.6: SEM image of a suspended low-cost uncooled detector pixel with 70 μm pitch.	8
Figure 1.7: Cross sectional drawing of a wafer level vacuum packaged low-cost infrared sensor die.	9
Figure 1.8: Image of the miniature camera electronics developed in MikroSens [26].	9
Figure 1.9: Thermal equivalent circuit of a microbolometer detector.	11
Figure 2.1: The electrical model of the microbolometer type uncooled thermal detectors characterized in this chapter [25].	15
Figure 2.2: Measured I-V data with the fitted curve. Fitting is done over 200 data points.	17
Figure 2.3: Measured temperature-voltage characteristic of 70 μm detector for different bias currents.	18
Figure 2.4: I-V curves of suspended and non-suspended detectors that are measured under vacuum environment. The deviation of suspended I-V curve shows the degree of thermal isolation.	20
Figure 2.5: Simplified diagram of absorption measurement method.	22
Figure 2.6: Absorption spectrum of the 70 μm pixel pitch low-cost microbolometer detector. Average absorption is found to be 78 % within the 7 μm -14 μm wavelength range. Test is conducted by Bilkent UNAM Center.	22
Figure 2.7: Conceptual spectrum for flicker and thermal noise [31].	24
Figure 2.8: Transient characteristic of the RTS noise [35].	25
Figure 2.9: Conceptual Lorentzian noise frequency spectrum for RTS and Flicker noise [38].	26
Figure 2.10: NSP method illustrated; (a) Data sequence is mapped on to a scatter plot revealing impact of the RTS noise. (b) Hypothetical scatter plot of a Gaussian noise process, which is differing from RTS process by single level clustering [39].	27
Figure 2.11: Detector noise measurement configuration.	28
Figure 2.12: Noise setup preamplifier circuit.	29
Figure 2.13: Measured gain spectrum of the noise amplifier.	29

Figure 2.14: Noise setup biasing circuit.....	30
Figure 2.15: Input referred voltage noise spectral density of the preamplifier when no detectors are present.	31
Figure 2.16: Measured noise of a 110 k Ω discrete resistor given with the theoretical noise floor. Noise floor for the measurement and theory is equal to 45 nVHz.....	32
Figure 2.17: Measured noise of a discrete diode given with the theoretical noise floor.	32
Figure 2.18: Measured noise spectrum of the detector Sample #1 given with the theoretical floor.....	33
Figure 2.19: Measured noise spectrum of the detector Sample #2 given with the theoretical floor.....	34
Figure 2.20: Measured noise spectrum of the detector Sample #3 given with the theoretical floor.....	35
Figure 2.21: Transient measurement result of a 110 k Ω discrete resistor. Red dot shows the center of mass for the scattered samples.	36
Figure 2.22: Noise Scattering Pattern (NSP) plot for the 110 k Ω discrete resistor transient measurement. Red dot shows the center of mass for the scattered samples.....	37
Figure 2.23: Transient measurement result of discrete diodes	37
Figure 2.24: Noise Scattering Pattern (NSP) plot for the discrete diode transient measurement. Red dot shows the center of mass for the scattered samples.....	38
Figure 2.25: Transient measurement result of detector set Sample #1.....	38
Figure 2.26: Noise Scattering Pattern (NSP) plot for the Sample #1 transient measurement. Red dot shows the center of mass for the scattered samples.....	39
Figure 2.27: Transient measurement result of detector set Sample #2.....	40
Figure 2.28: Noise Scattering Pattern (NSP) plot for the Sample #2 transient measurement. Red dot shows the center of mass for the scattered samples.....	41
Figure 2.29: Transient measurement result of detector set Sample #3.....	42
Figure 2.30: Noise Scattering Pattern (NSP) plot for the Sample #3 transient measurement. Red dot shows the center of mass for the scattered samples.....	42
Figure 2.31: Test setup for wafer level measurements.....	43
Figure 2.32: A photo of the PAV200 Probe Station, which is used in the probe tests.....	43
Figure 2.33: Wafer map for RTS noise measurements. Gray filled dies exhibit high level RTS noise activity while, yellow filled dies represent very low level or no RTS noise activity.....	44
Figure 3.1: Block diagram of first generation microbolometer detector array chip [25]. ...	48
Figure 3.2: A thermal image obtained from the sensor [25].	49
Figure 3.3: Noise injection paths in column readout circuits due to the supply bounce.	50
Figure 3.4: Block diagram of the test setup, which is used in testing 160x120 low-cost sensor chips.	52
Figure 3.5: An image of a test setup used in imaging and performance measurement.	53
Figure 3.6: Measured NETD histogram for the first design revision with F/1.0 optics.....	53
Figure 3.7: A thermal image obtained after the first design revision of the 160x120 low-cost sensor.	54
Figure 3.8: Average image noise over the array for the first design revision of the 160x120 low-cost sensor.....	55
Figure 3.9: Another sample image where the column noise is decreased by using median filtering technique.	55

Figure 3.10: Measured NETD histogram for the second design revision with F/1.0 optics.	57
Figure 3.11: Average image noise for the second design revision of the 160x120 low-cost sensor. The noise is averaged over 64 frames.....	57
Figure 3.12: Outdoor images obtained after the second design revision of the 160x120 low-cost sensor. (a) An image of recently driven cars (b) An image of humans along the outdoor elements.....	58
Figure 3.13: Average image noise over the array for the third design revision of the 160x120 low-cost sensor. The noise is averaged over 64 frames.....	59
Figure 3.14: Pixel and readout combined input referred noise histogram for the third design revision of the 160x120 low-cost sensor.....	60
Figure 4.1: Second generation low-cost sensor detector circuit along the DC voltage drops.	65
Figure 4.2: NETD vs. pixel pitch for two design parameter configurations. Blue line is drawn for first generation sensor pixels while red line is drawn for second generation pixels. Performance match is obtained by using 50 μm in the second generation design. .	66
Figure 4.3: Simplified model of the low-cost microbolometer pixel.....	67
Figure 4.4: Layout of the designed pixel.....	68
Figure 4.5: Cross sectional view of the designed pixel.....	68
Figure 4.6: Electrical model of the second generation low-cost detectors.....	69
Figure 4.7: Simulated I-V characteristic of the 50 μm detector.....	69
Figure 4.8: Simulated temperature-voltage characteristic of the 50 μm detector.....	70
Figure 4.9: Simulated voltage noise spectral density.....	71
Figure 4.10: Simulated temperature curve of the 50- μm detector for 3 μW applied power. Black squares indicate the simulated data points while orange line indicates the fitted curve.	72
Figure 4.11: Simulated temperature distribution along the pixel after 0.4 seconds of heating.....	73
Figure 4.12: (a) Pixel absorber physical model. (b) Transmission line model of the absorber layers [41].....	74
Figure 4.13: Simulated absorption curve. Average absorption is found to be 77 % within the range.....	74
Figure 4.14: Measured I-V data with the fitted curve for 50 μm detector. Fitting is done over 200 data points.....	75
Figure 4.15: Pixel and readout combined input referred noise histogram for 50 μm pixels utilized in a sensor FPA.....	76

LIST OF TABLES

TABLES

Table 2.1: Extracted parameters from the measured I-V curve.....	17
Table 2.2: Temperature sensitivity of diode detectors for different bias currents.....	19
Table 2.3: RMS voltage noises for DSA measurements.	35
Table 3.1: Readout opamps power dissipation table for the older design and the revised design.	51
Table 3.2: Test result comparison of three design revisions.	61
Table 4.1: Design parameters for 50 μ m pixel that is shown in Figure 4.3.	67
Table 4.2: Temperature sensitivities of 50 μ m diode detector for different bias currents. .	70
Table 4.3: Simulated thermal parameters for designed pixel.	72
Table 4.4: Extracted parameters from the measured I-V curve.....	75

CHAPTER 1

INTRODUCTION

Radiation in the infrared band can be sensed by two major types of detectors which, are classified as photonic detectors and thermal detectors.

Photonic detectors are composed of low bandgap semiconductors. Incident photons cause electron excitation in semiconductor's band structure creating electron-hole (E-H) pairs. Amount of infrared light is determined by sensing these E-H pairs using electrical circuits. Besides, photonic excitation, thermal excitation is another E-H pair generating mechanism in photonic detectors. To suppress the unwanted thermal generation, infrared photonic detectors need to be cooled down to cryogenic temperatures (~77K) [1].

Another way to detect infrared radiation is using the uncooled thermal detectors. In uncooled detectors, absorbed infrared radiation heats the detector structure. Temperature change is measured by observing the temperature dependent electrical parameters of detector materials. The first thermal infrared detector was invented by S. P. Langley in 1880 [2]. After nearly a century, Honeywell produced the first monolithic uncooled infrared detector Focal Plane Array (FPA) that integrates the detector array and readout electronics on the same chip [3]. Today, uncooled detector arrays are chosen for many applications such as defense, thermography, space science, automotive, security surveillance and, other military and civil applications [4].

On the contrary to visible image sensors, conventional uncooled infrared sensors are fabricated using complex MEMS processes increasing the production cost. Higher costs of these infrared sensors make them mostly unsuitable for civilian and commercial applications.

The low-cost uncooled sensor fabrication technique developed at the METU-MEMS Center targeted the production of commercially affordable sensors by utilizing standard CMOS and non-complicated MEMS processes [5, 6, 7, 8]. The aim of this thesis is to characterize the microbolometer type infrared sensors that are fabricated using the low-cost process and improve the imaging performance while reducing the pixel pitch.

1.1. Uncooled Thermal Detectors

Working principle of uncooled thermal detectors is based on sensing the heating effect of infrared radiation. Temperature change due to the heating is measured by certain materials that have temperature sensitive electrical properties.

The detectors are classified according to their electrical response to the temperature change. Most widely known uncooled infrared detector types are thermopiles, pyroelectric detectors, and microbolometers. Sections 1.1.1, 1.1.2, and 1.1.3 explain these detector types respectively.

1.1.1. Microbolometers

Figure 1.1 shows the representative drawing of a microbolometer detector pixel [9]. The pixel consists of a suspended structure on the support arms. When the infrared radiation is received, the suspended structure absorbs the radiation and heats up. Temperature change due to heating is sensed by the detector material buried inside the absorber. Support arms provide necessary thermal isolation for better heating of the structure while establishing the electrical connection to the detector material.

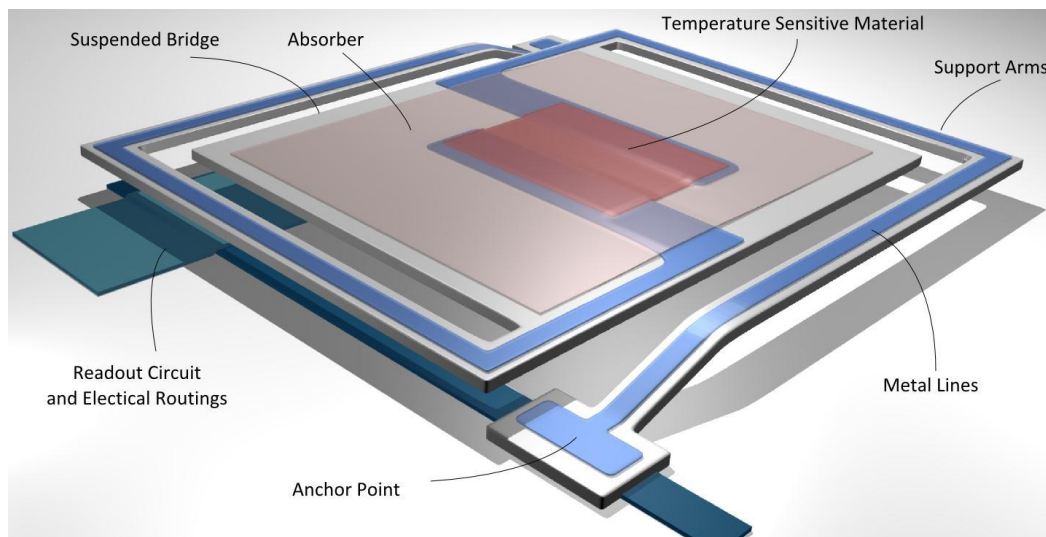
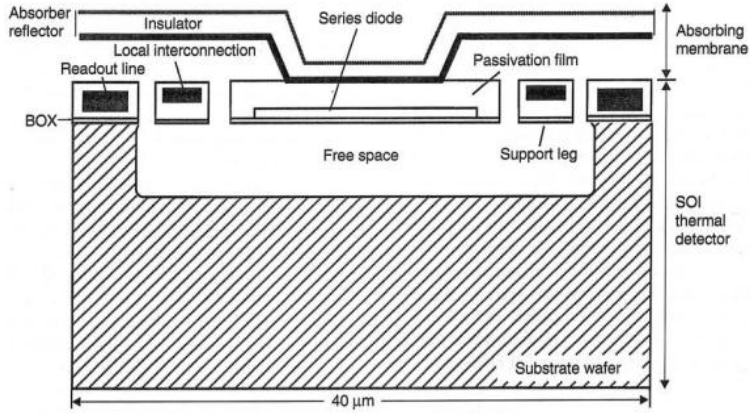


Figure 1.1: A representative drawing of a microbolometer detector pixel [9].

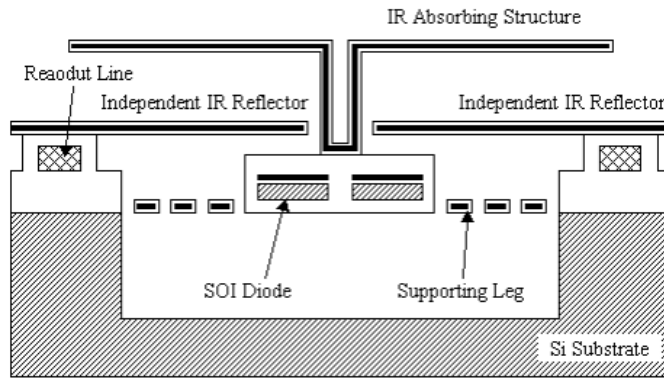
In microbolometers, the temperature sensitive material can be a resistor or diode. Temperature change is responded by electrical resistance change in case of a resistor detector, while temperature change is responded by forward voltage change in case of a diode.

Microbolometer active materials should exhibit high sensitivity to the temperature in order to detect radiant infrared light, which have a small power. One of the most popular detector materials used in microbolometers is Vanadium Oxide (VOX). VOX is selected because of its high Temperature Coefficient of Resistance (TCR) value and low resistance [10]. Different compositions of oxides such as VO_2 , V_2O_5 are used for obtaining different TCRs. It is reported that using Vanadium-Tungsten-Oxide can improve TCR and decrease sheet resistance [11]. Amorphous silicon (α -Si) is also a widely used detector material, which is selected because of its uniformity and compatibility with the CMOS production. Although, maximum TCR of 3 %/K is reported for α -Si, typical TCRs are between 1-2 %/K [12].

Another type of active materials that are used in microbolometers is silicon diode. The voltage drop across the forward-biased diode is sensitive to the temperature change. Therefore, by measuring the voltage across the diode, heating can be detected in microbolometers. Silicon diodes are easy to fabricate with the standard CMOS process making it desirable for cost effective microbolometer solutions [13]. Figure 1.2(a) shows the cross section of pixel with 40 μm pitch developed in Mitsubishi and used in a 320x240 FPA [14]. An extra absorber layer is employed within the pixel, in order to maximize the radiated area. Later, Mitsubishi developed a 640x480 FPA with a 25 μm pixel pitch [15]. Figure 1.2(b) shows the cross section for that pixel where an extra IR reflector layer is used for further increase in absorption, and longer support arms are implemented for better thermal isolation.



(a)



(b)

Figure 1.2: Cross sectional drawings of SOI Diode microbolometer pixels developed by Mitsubishi; (a) 40 μm pixel with absorber layer [14] (b) 25 μm pixel with absorber and independent reflector layer [15].

1.1.2. Thermopile Detectors

Thermopiles are thermal detectors that are composed of serially connected thermocouples. Figure 1.3 shows the representative drawing of a microcantilever thermopile detector [16]. Bimetallic junction ends of thermocouples are placed on the suspended side and the substrate side in an alternating fashion. When the infrared radiation is absorbed, suspended side of the detector gets heated and the substrate side remains cold. Due to the Seebeck Effect in bimetallic junctions, a voltage difference is observed between the thermopile terminals. The voltage difference is proportional to the temperature difference between the cold side and hot side.

The main advantage of thermopile detectors is that they can work under zero bias condition, which prevents self-heating and higher power dissipation. Another advantage of thermopiles is that they do not suffer from the flicker noise unlike other types of uncooled sensors [17]. Despite their advantages, thermopiles have very limited application areas because of their low responsivities and large pixel sizes. As a large format, a 128x128 thermopile FPA with 100 μm pixel pitch is reported [18]

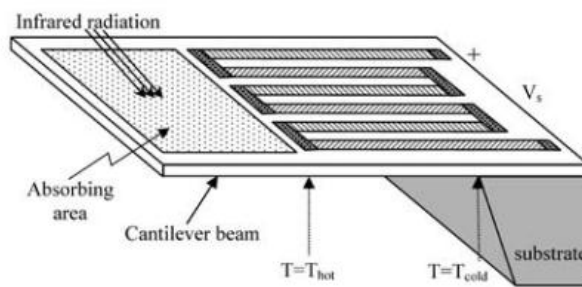


Figure 1.3: Representative drawing of a microcantilever thermopile detector [15].

1.1.3. Pyroelectric Detectors

Pyroelectric effect is the sudden charge induction on a pyroelectric material in response to a temperature change. All ferroelectric materials exhibit pyroelectricity. By utilizing this property of certain materials, temperature change can be sensed in uncooled infrared detectors [19]. Like thermopile detectors, pyroelectric detectors can work under zero bias condition without the self-heating problem. As a disadvantage, in pyroelectric detectors, incoming infrared radiation needed to be modulated to higher frequencies using a chopper. Figure 1.4 shows a Scanning Electron Microscope (SEM) image of a Raytheon 320x240 pyroelectric FPA with 50 μm pixel [20].

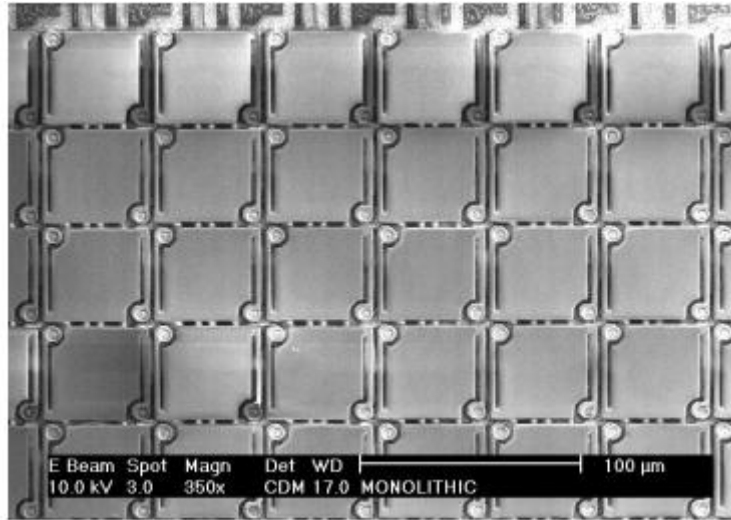


Figure 1.4: SEM image of the 320x240 pyroelectric FPA developed by Raytheon [20].

1.2. Low-Cost Uncooled Thermal Imaging

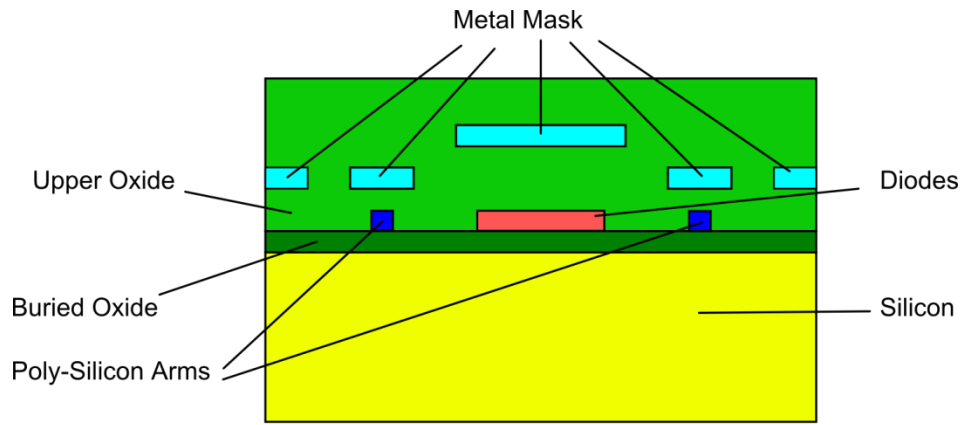
This section explains the low-cost uncooled thermal imaging technology, which constitutes the basis of the work in this study. Effort for developing low-cost infrared sensors was started in METU-MEMS Center [5, 6, 7, 8] and now it continues in the METU-MEMS spin-off company MikroSens [21].

Low-cost pixels investigated in scope of this thesis utilize silicon diodes as active materials and fabricated using Silicon-On-Insulator Complementary Metal Oxide Semiconductor (SOI-CMOS) and bulk micromachining processes. Section 1.2.1 explains the Post-CMOS process flow. Section 1.2.2 presents the vacuum packaging method used in low-cost infrared sensors. Finally, Section 1.2.3 gives information about the camera development works.

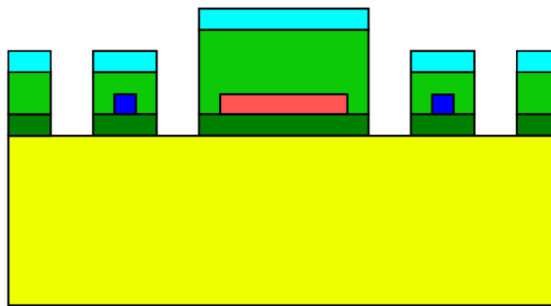
1.2.1. Detector Fabrication

Fabrication of low-cost microbolometer detector arrays consists of CMOS fabrication and Post-CMOS process flow. Monolithically integrated chip that includes the readout circuitry and pixel array is fabricated using the SOI-CMOS fabrication [22, 23, 24, 25].

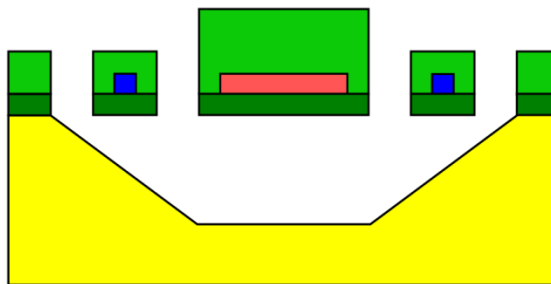
Figure 1.5 gives the Post-CMOS process flow in a simplified manner. The CMOS metal routing layers are used as mask for etching. Etching is done through the silicon handle wafer. Lastly, silicon handle wafer is etched using TMAH solution. The last step suspends the detector structure on the support arms providing thermal isolation [24]. Figure 1.6 shows a Scanning Electron Microscope (SEM) image for the suspended low-cost infrared sensor pixel structure.



(a)



(b)



(c)

Figure 1.5: Simplified diagram for process steps: (a) Pixel before Post-CMOS processing (b) DRIE etching of the oxide gaps using Metal-3 layer as mask (c) Metal layer stripping and pixel releasing by TMAH etching of the silicon handle wafer.

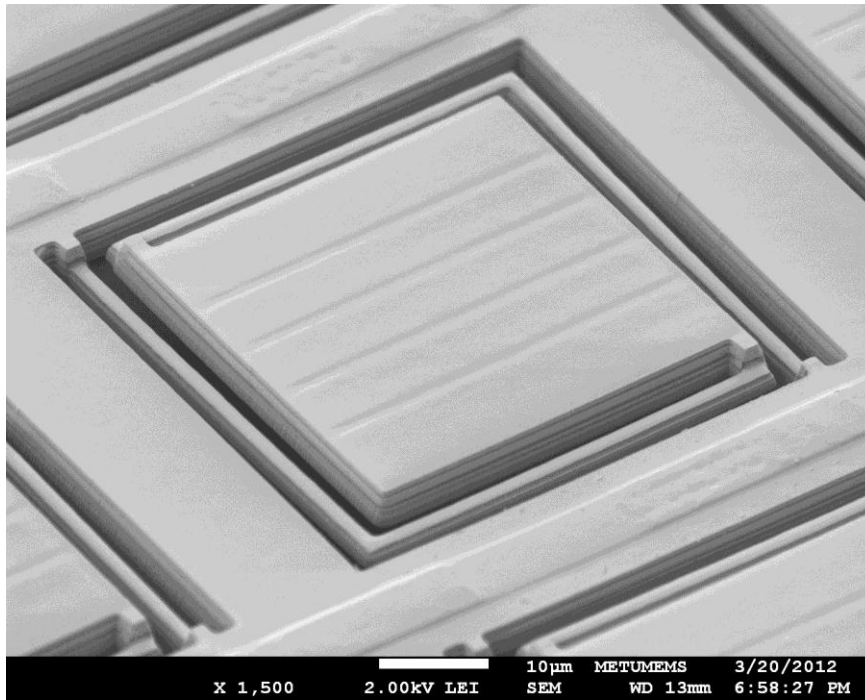


Figure 1.6: SEM image of a suspended low-cost uncooled detector pixel with 70 μm pitch.

1.2.2. Vacuum Packaging

Uncooled thermal detectors need to be working inside a vacuum environment in order to provide thermal isolation. Vacuum can be provided using motor pumps, which are bulky and quite power-hungry. In miniature camera systems, it is more convenient to provide vacuum by using vacuum packaging instead of pumps. Currently, there are two different approaches for vacuum packaging; individual vacuum packaging and wafer level vacuum packaging. The individual vacuum packaging technology uses a specific ceramic or metal package in order to provide vacuum environment for the sensor in it. The top of the package is sealed with an IR-transmitting material such as germanium. Although this method is used by most of the foundries for uncooled thermal imaging, the nature of packaging the dies one by one makes this process not suitable for low-cost systems. The second method, on the other hand, packages all the dies on a wafer simultaneously. A cap wafer is specifically prepared for this purpose as seen in Figure 1.7. This cap wafer is bonded hermetically to the detector wafer under vacuum environment. The uncooled thermal sensor die is encapsulated by the cap wafer and the bonding between the CMOS and cap wafers is done by a specific adhesive material. The vacuum quality is improved by using a vacuum getter, which chemically absorbs the remaining air atoms after the sealing.

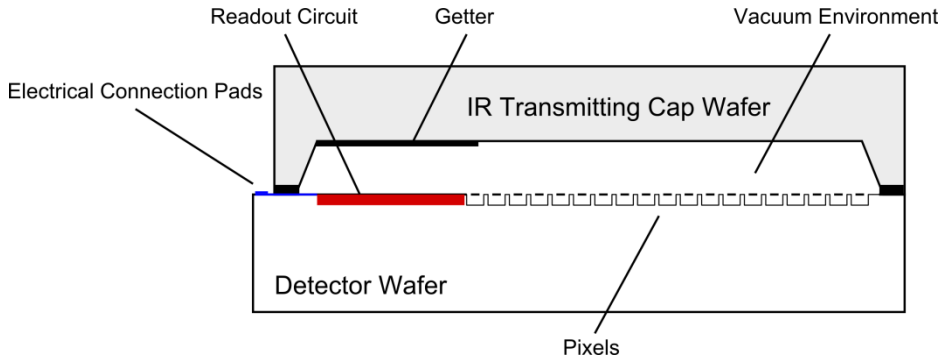


Figure 1.7: Cross sectional drawing of a wafer level vacuum packaged low-cost infrared sensor die.

1.2.3. Miniature Camera

Parallel to the growing commercial demand for infrared imaging, there is a trend towards to the miniaturization of IR camera systems. In order to meet this demand, a camera development work is conducted in scope of another thesis [26]. Figure 1.8 shows an image of the electronics for the implemented camera. The camera consists of four PCB modules. USB communication board establishes the interface between the camera and the PC. Digital interface board is responsible for programming and timing. Power board includes voltage regulators in order to power up circuits. Lastly, sensor interface board provides analog signals needed by the sensor and it includes the Analog-Digital Converter (ADC), which digitizes the analog image data. The miniature camera utilizes the vacuum packaged low-cost infrared sensor die developed in scope of this thesis.

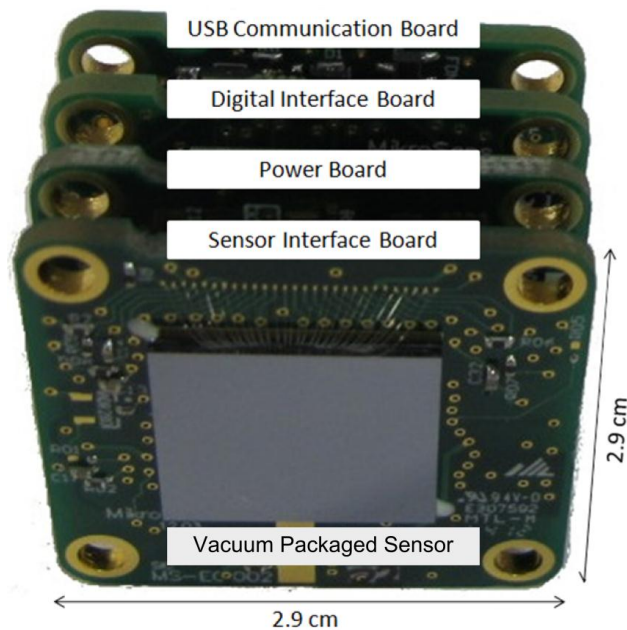


Figure 1.8: Image of the miniature camera electronics developed in MikroSens [26].

1.3. Performance Parameters

This section introduces the parameters that are used to evaluate low-cost uncooled microbolometer performance. Section 1.3.1 explains the temperature sensitivity (TC), which is an important parameter for detector performance. Section 0 derives the responsivity using the thermal model of the detector. Finally, Section 1.3.3 defines the Noise Equivalent Temperature Difference (NETD), which is a commonly used figure of merit for the infrared detectors.

1.3.1. Temperature Sensitivity (TC)

Temperature sensitivity is defined for diode type detectors as the amount of the change in the forward-voltage of current biased diode in response to the temperature change.

Drop on voltage of an forward biased diode is defined as in Equation (1.1) where the n_i is the ideality factor, k is the Boltzmann Constant, T is the temperature, q is the electron charge, I_D is the bias current, and I_S is the reverse saturation current [27].

$$V_F = n_i \frac{kT}{q} \ln \frac{I_D}{I_S} \quad (1.1)$$

Reverse saturation current (I_S) can be expressed as in Equation (1.2) where K is a constant between 2.5 and 5, E_g is the bandgap energy of silicon, which is about 1.12 eV [15].

$$I_S = KT^m e^{\frac{-E_g}{kT}} \quad (1.2)$$

Inserting Equation (1.2) and taking derivative of the forward voltage expression gives the temperature sensitivity (TC_D) as:

$$TC_D = \frac{dV_F}{dT} = \frac{k}{q} \ln \frac{I_D}{I_S} - m \frac{kT}{qT} - \frac{E_g}{qT} = - \frac{m \frac{kT}{q} + \frac{E_g}{q} - V_F}{T} \quad (1.3)$$

The Equation (1.3) simplifies to the Equation (1.4) by inserting nominal values of E_g , k , q and T .

$$TC_D = \frac{dV_F}{dT} = - \frac{0.025m + 1.12 - V_D}{q} \quad (1.4)$$

1.3.2. Responsivity

Responsivity of a detector is defined as the amount of electrical signal change per unit received infrared radiation power. Electrical signal can be in current or voltage form depending on the type of detector. Equation (1.5) defines the responsivity for a voltage type output detector where ΔV_{out} is the change in output signal and P_{inf} is the incident radiation power [28].

$$R = \frac{\Delta V}{P_{inf}} \quad (1.5)$$

As it is explained in Section 1.1.1, in microbolometer, incident infrared radiation causes a temperature change in the detector. The change in the temperature due to the received infrared radiation in microbolometers can be determined by using heat flow equation. Figure 1.9 shows the thermal equivalent circuit for a microbolometer detector [29].

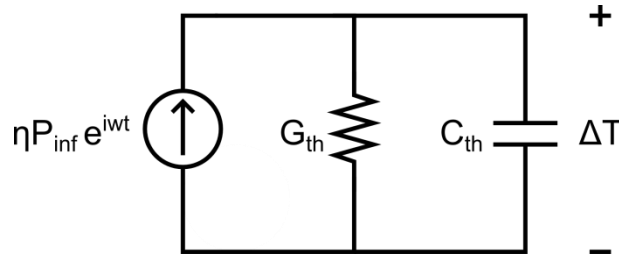


Figure 1.9: Thermal equivalent circuit of a microbolometer detector.

The heat flow equation for the circuit is given in Equation (1.6) where C_{th} is the thermal capacitance, G_{th} is the thermal conductance, ΔT is the temperature change, η is the absorption coefficient, P_{inf} is the power of the incident infrared light on to the absorbing region.

$$C_{th} \frac{d\Delta T}{dt} + G_{th} \Delta T = \eta P_{inf} e^{i\omega t} \quad (1.6)$$

Solving for the magnitude of temperature change ($|\Delta T|$) gives:

$$|\Delta T| = \frac{\eta P_{inf}}{G_{th} \sqrt{1 + (w\tau)^2}} \quad (1.7)$$

In Equation (1.7), τ is the time constant, which is defined in Equation (1.8). Time constant is an important performance parameter and it defines the limit of detector speed.

$$\tau = \frac{C_{th}}{G_{th}} \quad (1.8)$$

The voltage change in the detector output in response to temperature change can be found using Equation (1.9) where TC is the temperature sensitivity.

$$\Delta V = TC_D \cdot |\Delta T| \quad (1.9)$$

Inserting Equation (1.7) in Equation (1.9) gives:

$$\Delta V = \frac{TC_D \eta P_{inf}}{G_{th} \sqrt{1 + (w\tau)^2}} \quad (1.10)$$

The responsivity is derived in Equation (1.11) by using Equation (1.5) and Equation (1.10) together.

$$\mathcal{R} = \frac{TC_D \eta}{G_{th} \sqrt{1 + (w\tau)^2}} \quad (1.11)$$

1.3.3. Noise Equivalent Temperature Difference (NETD)

Noise Equivalent Temperature difference (NETD) is defined as the amount of target blackbody temperature change that causes an electrical signal change in the detector side that is equal to the detector internal Root Mean Square (RMS) noise. In other words, NETD represents the minimum target temperature difference that detector can be resolved. Equation (1.12) gives the NETD expression [30].

$$NETD = \frac{4(F/\#)^2 V_n}{A_D \mathcal{R} T \left(\frac{\Delta p_{target}}{\Delta T_{target}} \right)_{\lambda_2-\lambda_1}} \quad (1.12)$$

In the NETD expression, $F/\#$ is the F-number of the optics, V_n is the total detector RMS noise, A_D is the area of the detector absorbing region, \mathcal{R} is the detector responsivity, T is the integrated transmission of the optics along the transmission atmosphere for the wavelength region λ_1 to λ_2 and, the $(\Delta p_{target}/\Delta T_{target})_{\lambda_2-\lambda_1}$ is a constant, which is defined as the change in power per unit area (Δp_{target}) radiated by a blackbody per temperature change in the target (ΔT_{target}) integrated for the wavelength region λ_1 to λ_2 .

1.4. Research Objectives and Thesis Organization

The main goal of this research is to characterize diode type low-cost uncooled microbolometer detectors, develop infrared imagers with improved performance, and add functionality to be used in commercial applications. The specific and more detailed objectives can be listed as follows:

1. Performance of the low-cost infrared sensors is limited by several factors. These factors should be determined by detailed characterization tests of detectors. Care should be taken when selecting the characterization methods.
2. Noise of the low-cost infrared detectors should be characterized deeply. A convenient test setup should be developed in order to make accurate measurements. Noise measurement results should be analyzed properly.
3. Readout electronics of the low-cost infrared sensor FPAs should be improved for better performance and functionality. Image quality should be as high as possible and noise impact should be decreased in order to make sensor usable in commercial applications. Also, improved FPAs should dissipate less power and remain stable under shifting environment temperature.
4. A new generation of low-cost infrared pixel with a smaller pitch should be designed in order to decrease the cost further and comply with the smaller optics. Designed pixel should be characterized by simulations and tests.

Organization of the thesis as follows;

Chapter 2 gives information about the detailed characterization tests of the low-cost pixel with 70 μm pitch that is previously developed at the METU-MEMS center. Characterization includes the measurement of performance parameters and detailed analysis of the noise. Chapter 3 presents improvements that have been made on the readout electronics of the 160x120 70 μm pixel pitch FPA, which is developed in the work [25]. Outcomes of three design revisions are explained along the test results. Chapter 4 explains the design process of the second generation low-cost infrared sensor pixels. Optimization of the pixel parameters is presented along the simulation and test results. Finally, Chapter 5 summarizes the work done in this study and mentions the ongoing work.

CHAPTER 2

PIXEL CHARACTERIZATION OF FIRST GENERATION LOW-COST INFRARED SENSORS

This chapter focuses on the detailed tests and characterization of the microbolometer type uncooled thermal detectors of the first generation low-cost infrared sensors developed in [25]. Figure 2.1 shows the electrical model of the microbolometer type uncooled thermal detectors characterized in this chapter. The first generation sensor arrays incorporate 70 μm pitch detector pixels, which are arranged in 160x120 focal plane array (FPA) resolution. Each detector is made of 4 serially connected diodes, which are used as the active material of the detector. So the absorbed infrared power heats up the detector mass and the diode voltage changes. The readout integrated circuit (ROIC) engaged together with the detector FPA in order to sense this change, amplifies it, and creates an analog video signal by multiplexing each detector in the FPA.

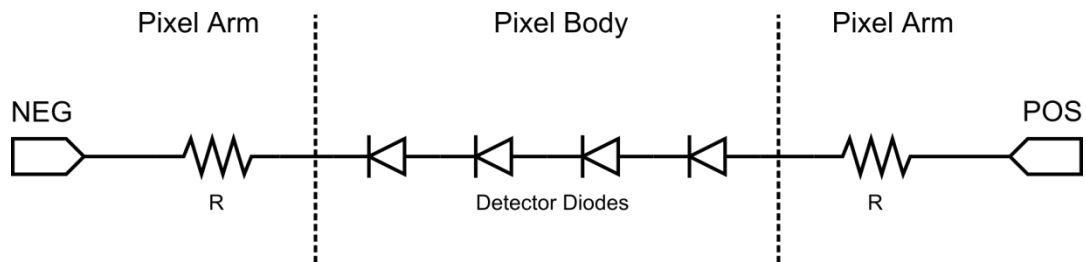


Figure 2.1: The electrical model of the microbolometer type uncooled thermal detectors characterized in this chapter [25].

The detailed characterization of the detectors is the first main step of designing high performance sensors. Section 2.1 summarizes electrical I-V characterization measurements, which is the first step of the whole characterization process. The microbolometer type uncooled thermal detectors characterized in this chapter use SOI diodes as the active material, which is temperature sensitive in order to sense the absorbed infrared power. The temperature sensitivity of the detectors is measured and the results are summarized in Section 2.2. The thermal conductance is the measure of the thermal isolation of the detector mass from the environment. The thermal conductance is one of the main performance limiting parameters of the microbolometer type uncooled thermal detectors as discussed in Section 1.3. Section 2.3 gives the developed characterization methods in order to precisely measure the thermal conductance of the detectors. The test results are also discussed in the same chapter. Section 2.4 presents the results of the optical absorption measurement. Optical absorption directly affects the detector responsivity.

Section 2.5 gives details about the detector noise characterization works conducted in the scope of this thesis. This section defines the major noise sources of the SOI diodes, which are the detector active material, and explains the reason of observing higher than expected noise in the previous works. Finally, Section 2.6 summarizes and concludes the detailed characterization test results conducted in the scope of this thesis.

2.1. Current-Voltage (I-V) Characterization

The current-voltage (I-V) curve is a detector characteristic, which reveals some parameters such as series resistance, detector drop-on voltage, ideality factor, and reverse saturation current, some of that are not provided by the CMOS foundry. These parameters are important while developing the readout circuits for detectors. I-V curve of the detector is obtained using the Agilent B1500A Semiconductor Parameter Analyzer. Detector parameters can be obtained by curve fitting from the I-V curve. Equation (2.1) gives the detector expression that is used in curve fitting.

$$V_F = n_i \frac{kT}{q} \ln \frac{I_D}{I_s} + R_{arm} \cdot I_{bias} \quad (2.1)$$

The parameters in Equation (2.1) are; number of series diodes (n_d), thermal voltage (V_T), diode ideality factor (n_i), detector bias current (I_{bias}), arm resistance (R_{arm}), and reverse saturation current (I_s). In the equation n_d , V_T , and I_{bias} are known parameters and R_{arm} , n_i and I_s are fitted parameters. Figure 2.2 shows the measured I-V data along the fitted curve. Table 2.1 shows the extracted parameters from the curve fitting. The results show that the ideality factor is 1.0088, which is very close to unity as expected, the reverse saturation current is 7.2×10^{-19} A, and the arm resistance is 7127 Ω .

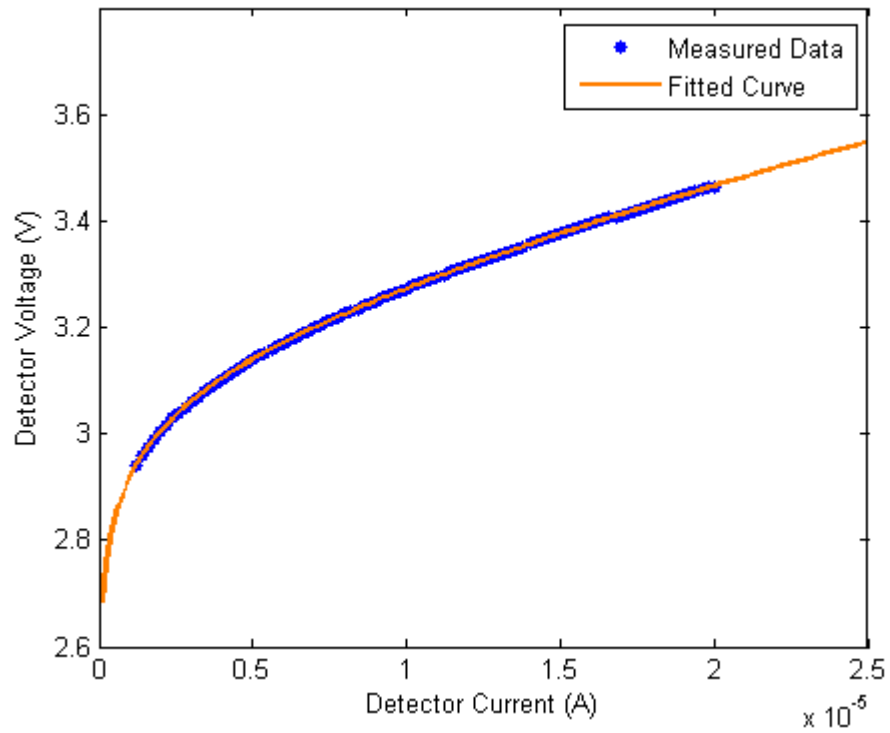


Figure 2.2: Measured I-V data with the fitted curve. Fitting is done over 200 data points.

Table 2.1: Extracted parameters from the measured I-V curve.

Parameter	Value
Ideality Factor (n)	1.0088
Reverse Saturation Current (I_s)	7.2×10^{-19} A
Arm Resistance (R_{arm})	7127 Ω

2.2. Temperature Sensitivity (TC) Measurement

Temperature sensitivity (TC) is measured by sweeping the detector temperature and observing the detector forward voltage under different bias currents. An environment chamber is used for sweeping the temperature. Detector samples are mounted on a ceramic substrate and placed inside the chamber. The true temperature is obtained by a temperature sensor that is mounted the same ceramic substrate with detector sample. Figure 2.3 shows the measured temperature-voltage characteristic of 70 μm detector for different bias currents.

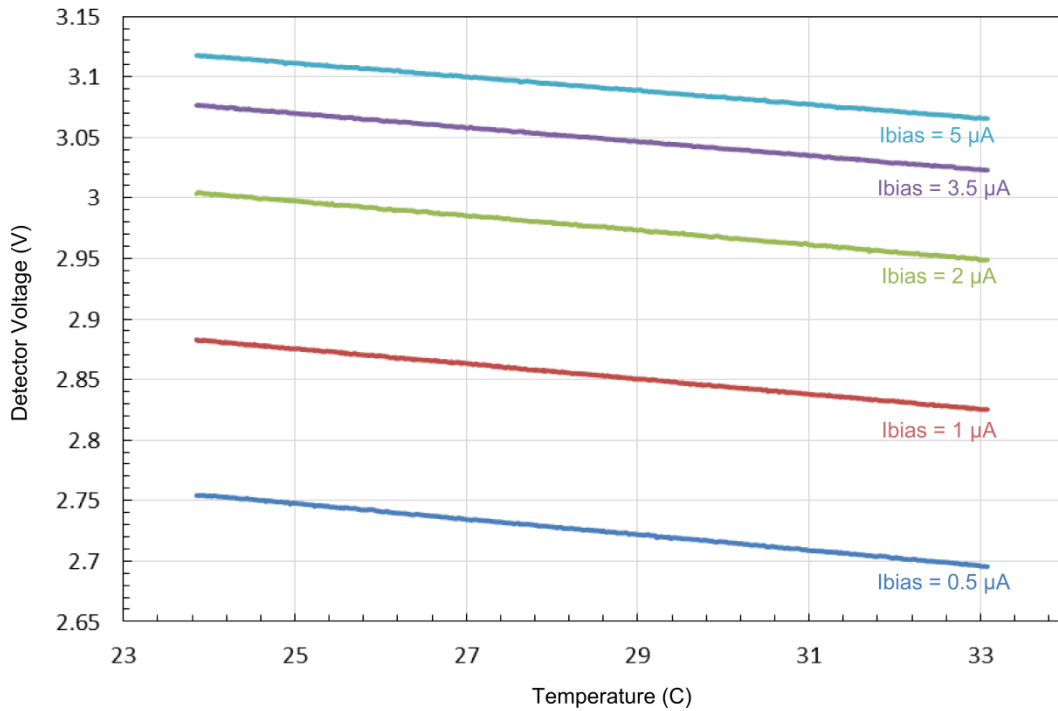


Figure 2.3: Measured temperature-voltage characteristic of 70 μm detector for different bias currents.

Table 2.2 shows the extracted TC data from the temperature-voltage measurements. TC data is obtained by linear curve fitting on temperature-voltage curves. It is observed that TC decreases with the increasing detector bias current. This relationship is compatible with the diode TC equation, which is explained in Section 1.3.

Table 2.2: Temperature sensitivity of diode detectors for different bias currents.

Detector Bias Current	Temperature Sensitivity (TC)
0.5 μA	-6.41 mV/K
1 μA	-6.24 mV/K
2 μA	-5.99 mV/K
3.5 μA	-5.81 mV/K
5 μA	-5.69 mV/K

2.3. Thermal Conductance Measurement

One of the most important properties that determine microbolometer performance is the thermal conductance, which is a measure of the thermal isolation of the pixel active mass from the environment. Thermal conductance of detector pixels is measured using the bias heating method, in which a bias current is applied on to the vacuumed detector that causes a temperature increase due to the electrical power dissipation [22]. Equation (2.2) gives the temperature change due to the bias heating where I_{bias} is the detector biasing current, V_{det} is the measured detector voltage, ΔT is the temperature change in the pixel, G_{th} is the thermal conductance, τ is the time constant, and t is the time.

$$\Delta T = \frac{V_{\text{det}} * I_{\text{bias}}}{G_{\text{th}}} (1 - e^{-t/\tau}) \quad (2.2)$$

In Equation (2.2), detector bias current is already known (I_{bias}) and V_{det} can be measured with a multimeter. The exponential decay term of the equation can be ignored when the electrical bias is continuously applied. This is assured by applying the electrical power for a duration of much larger than the thermal time constant (τ) of the detector. To obtain temperature difference (ΔT), temperature-voltage relation of detector can be used. Equation (2.3) gives that relation.

$$V_{\text{det}} = V_0 + \text{TC} * \Delta T \quad (2.3)$$

In Equation (2.3), V_{det} is the detector voltage measured after thermal settling, TC is the temperature sensitivity, and V_0 is the detector voltage before the thermal settling. Basically there are two methods to determine the initial voltage of the detector (V_0): The first one is to use a different non-suspended detector that does not heat up due to the electrical power

dissipation. This method, however, may result in small inconsistency because of the mismatch between the measured detectors.

The second method is to observe V_o on the same detector in atmospheric pressure. At the atmospheric pressure, thermal conductance of the detector increases to high levels. It should be noted that, even with high thermal conductance values, the detector under atmospheric pressure can still be heated up by the electrical power. Both methods described above are used during the thermal conductance measurements conducted in the scope of this thesis. The experience gained from the tests show that the first method results in more consistent results for variety of detector currents.

Figure 2.4 shows the I-V curves of suspended and non-suspended detectors that are measured in the vacuum environment. Vacuum level of the chamber during the test was 20 mTorr, which is measured by the vacuum sensor located in the vacuum chamber. Because of the negative temperature coefficient of diode, the I-V curve of suspended detector deviates from the non-suspended detectors' I-V curve at higher bias currents. The measured data in the Figure 2.4 results in thermal conductance value of 202 nW/K, which is comparable to the simulated value of 240 nW/K.

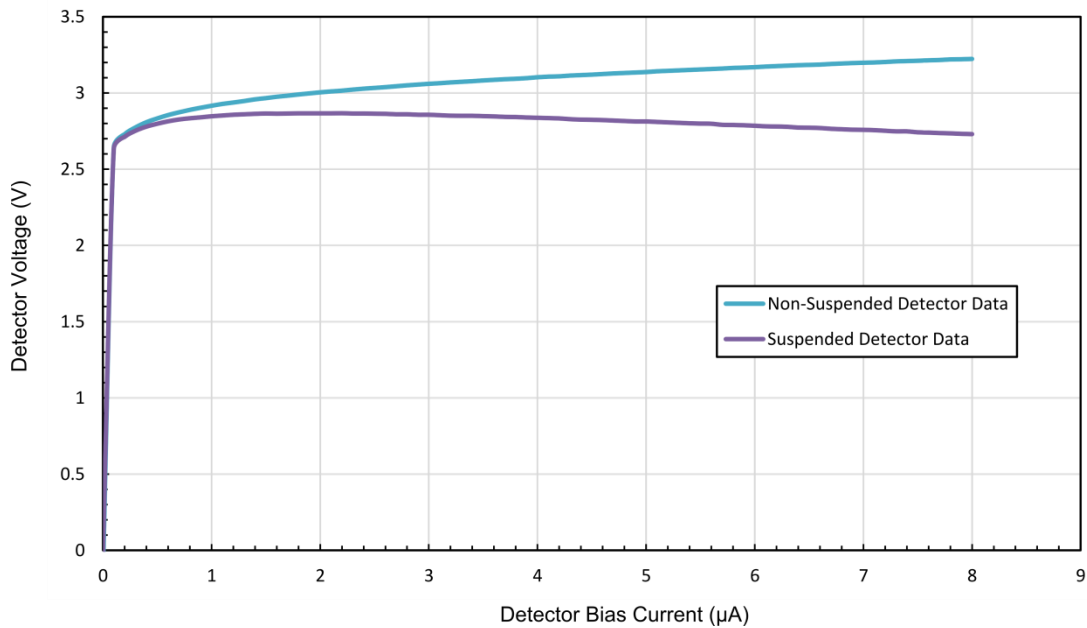


Figure 2.4: I-V curves of suspended and non-suspended detectors that are measured under vacuum environment. The deviation of suspended I-V curve shows the degree of thermal isolation.

2.4. Absorption Measurement

Absorption is a measure of the ratio of the absorbed thermal radiation to the total thermal radiation. The active area of the low-cost microbolometer pixel includes several layers that can absorb, reflect, and transmit the infrared radiation. One can determine absorbed energy by sending light and sensing reflected and transmitted light. From the Equation (2.4) absorbed energy can be obtained.

$$E_{absorbed} = E_{incident} - (E_{reflected} + E_{transmitted}) \quad (2.4)$$

In the absorption measurements, the Fourier Transform Infrared Spectroscopy (FTIR) method is utilized. In normal infrared spectroscopy, the target is illuminated with a single wavelength (monochromatic) light source and a transmission or reflection spectrum is obtained by sweeping source wavelength. In FTIR measurement, the light source is not monochromatic. Instead, it has a pulse characteristic in transient domain where its spectrum is wideband. Transmission or reflection spectrum is obtained by Fourier transforming the transient light pulse. With that method reflection can be obtained for each wavelength in a spectrum of interest [31]. Figure 2.5 shows the principle behind the method in a simplified manner. The active area of the 70 μm pixel pitch detector consists of a thick Silicon Dioxide absorber layer that is laid off on top of an Aluminum reflector metal layer. Below the reflector layer, CMOS detector diodes are placed. The purpose of the reflector layer is, directing the light rays into the absorber layer for the second time after the first incidence. By that way, absorption chance of the light is increased. So the incident radiation is either absorbed by the absorber or reflected by the reflector metal, and the reflected radiation is measured by the light sensor.

Figure 2.6 shows the spectral absorption measurement result that is conducted by Bilkent UNAM Center. The average absorption is found to be 78 % between the wavelengths 7 μm to 14 μm .

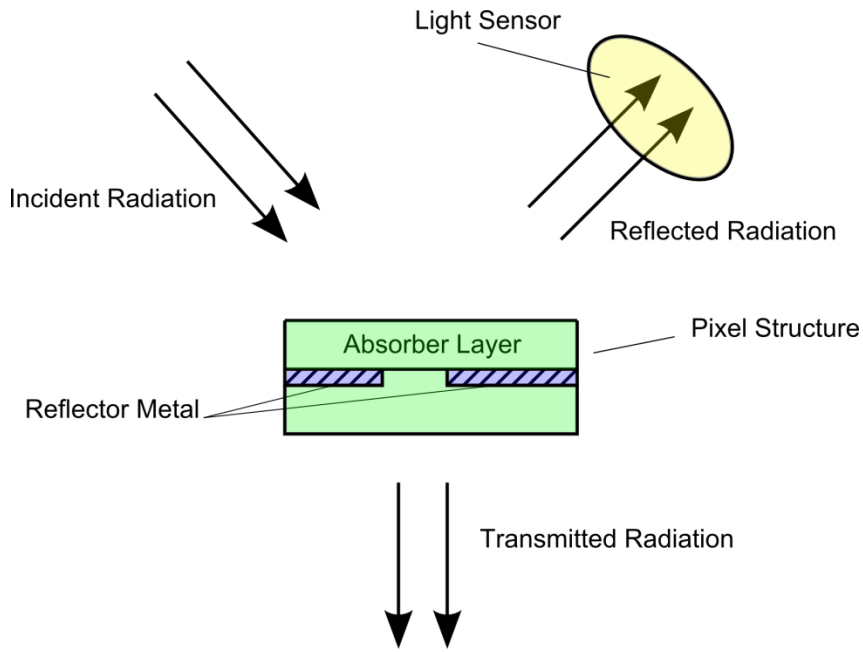


Figure 2.5: Simplified diagram of absorption measurement method.

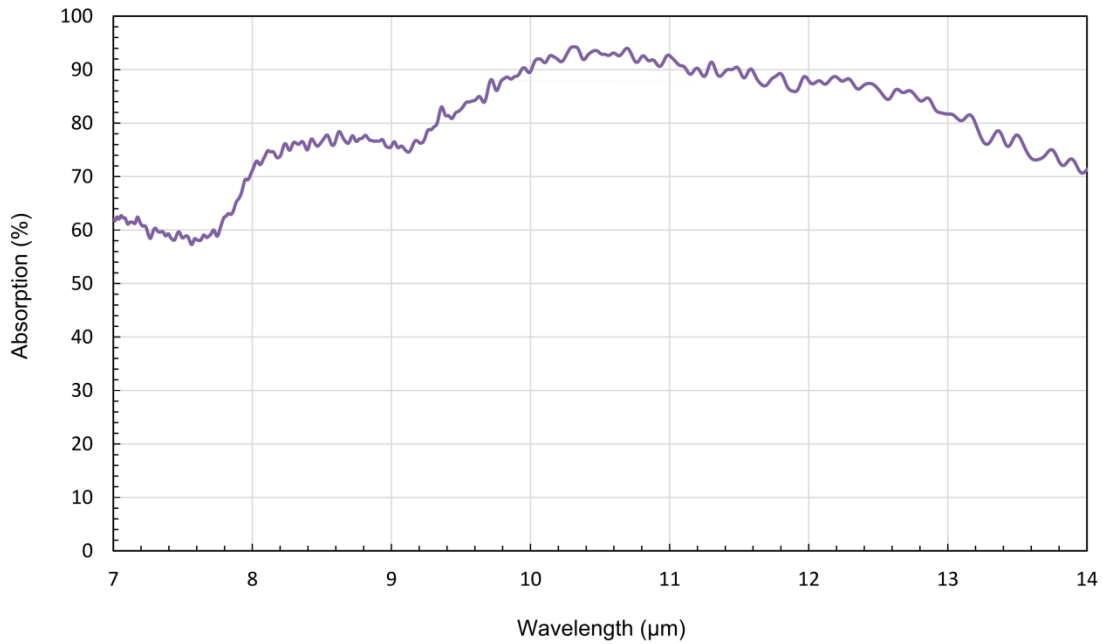


Figure 2.6: Absorption spectrum of the 70 μm pixel pitch low-cost microbolometer detector. Average absorption is found to be 78 % within the 7μm-14 μm wavelength range. Test is conducted by Bilkent UNAM Center.

2.5. Detector Noise Characterization

This section explains the noise characterization, theory, and analysis of 70 μm detector pixels. White noise, flicker noise, and RTS noise mechanisms are inspected. Especially, RTS noise is investigated in depth due to its predominance in low-cost microbolometer detectors.

2.5.1. Theory

Noise is one of the most important performance determining factors in infrared imagers. Major noise types observed in microbolometers are thermal noise (Johnson noise), shot noise, flicker (1/f) noise, and Random Telegraph Signal (RTS) noise.

Thermal noise (Johnson noise) is caused by the random motion of electrons in a conductor. Ideally, thermal noise has a constant power density in all spectrum, namely it is a white noise mechanism. Equation (2.5) gives the power spectral density of the thermal noise where k_b is the Boltzmann constant, T is the temperature, R is the resistance, and Δf is the unit frequency [32].

$$V_n^2 = 4k_b TR\Delta f \quad (2.5)$$

Shot noise is another white noise mechanism that occurs at the pn junction devices. Shot noise is caused by the statistical nature of the charge carriers. Equation (2.6) gives the power spectral density of the shot noise in terms of current. In the equation q is the unit electron charge, I_D is the pn junction bias current and Δf is the unit frequency [32].

$$i_n^2 = 2qI_D\Delta f \quad (2.6)$$

Another noise mechanism that is observed in pn junction devices is Flicker noise (1/f noise) [33]. At silicon interfaces, single crystal structure is getting broken inducing extra energy states other than normal energy states. The trapping and de-trapping of charge carriers in these energy bands causes a fluctuation in current. This fluctuation presents itself as flicker noise. Differently from the white noise, flicker noise has a power spectrum that inversely depends to the frequency. Equation (2.7) gives the formula for flicker noise in pn junction diodes [15]. Here K is the flicker noise parameter, which cannot be easily determined due to its dependence on several other parameters such as junction area, process quality, and doping concentration [34].

$$v_n^2 = \frac{K}{f} \Delta f \quad (2.7)$$

When the flicker noise and white noise are both present in a device, the corner frequency (f_c) becomes a useful parameter. Figure 2.7 explains the spectral characteristic of noise when flicker and white noise are present. Below the corner frequency, the dominated noise source is flicker noise. Above the corner frequency, white noise becomes significant. The value of noise power density above corner frequency is called white noise floor.

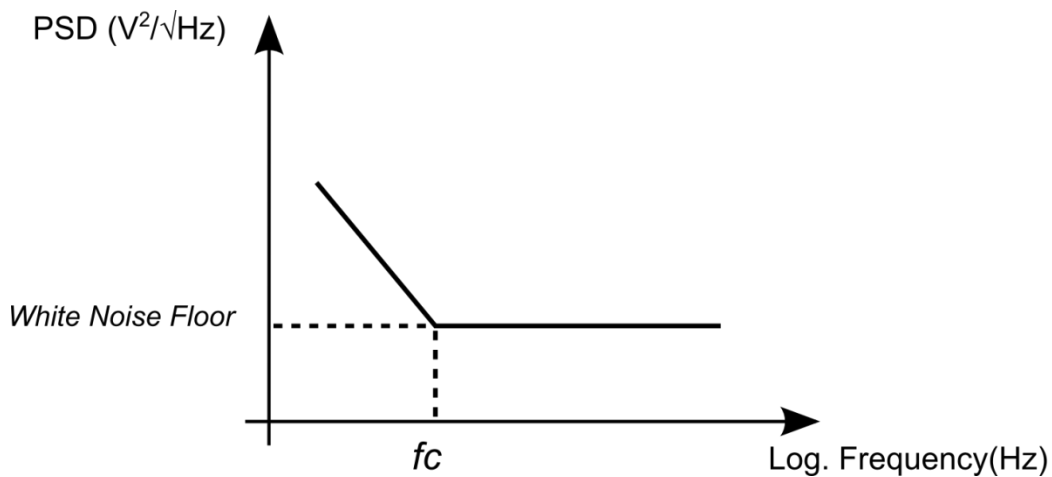


Figure 2.7: Conceptual spectrum for flicker and thermal noise [31].

Besides the flicker noise, there is another noise mechanism that is called Random Telegraph Signal (RTS) noise or burst noise [35]. Like the Flicker Noise, RTS noise is observed in the low side of the spectrum. Although the exact cause of RTS noise cannot be resolved yet, it is thought that RTS originates from carrier trapping/de-trapping in crystal defect sites [36]. RTS noise has a characteristic of level changing in the transient domain. Figure 2.8 illustrates this phenomenon. These levels can be two or more and they show a square wave characteristic, which differs from other noise mechanisms [35].

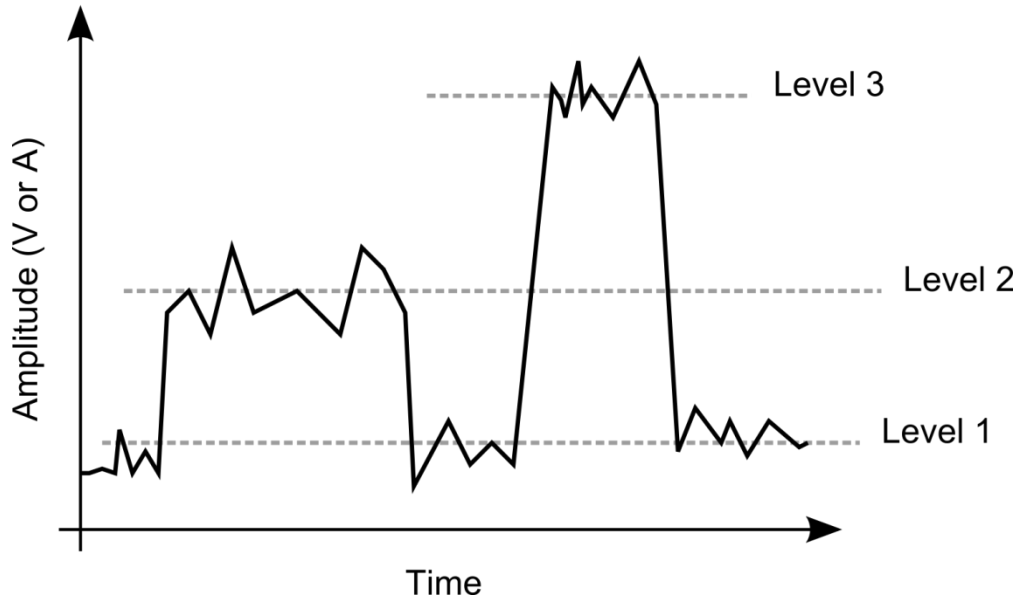


Figure 2.8: Transient characteristic of the RTS noise [35].

The occurrence of RTS level changes is characterized by observing the signal by high resolution acquisition system for a long time period. An RTS level change can occur in seconds, minutes, or even longer time durations. Shorter level changes cannot be differentiated from flicker noise spikes. Thus, in the frequency domain, RTS becomes significant at low frequency regions. Frequency domain representation of RTS noise is different from flicker and white noise. The spectral characteristic of RTS noise can be represented with Lorentzian Function [38]. Equation (2.8) gives the Lorentzian function for the voltage RTS noise. Here in this equation, τ is the average trapping duration and f is the frequency.

$$v_n^2 = \frac{4\tau}{1 + (2\pi f\tau)^2} \Delta f \quad (2.8)$$

Lorentzian spectrum corresponds to a flat region at the beginning of spectrum. This flatness causes a second corner frequency together with flicker noise. Figure 2.9 shows the conceptual spectrum characteristic of RTS noise. The frequency point f_0 represents the RTS corner frequency.

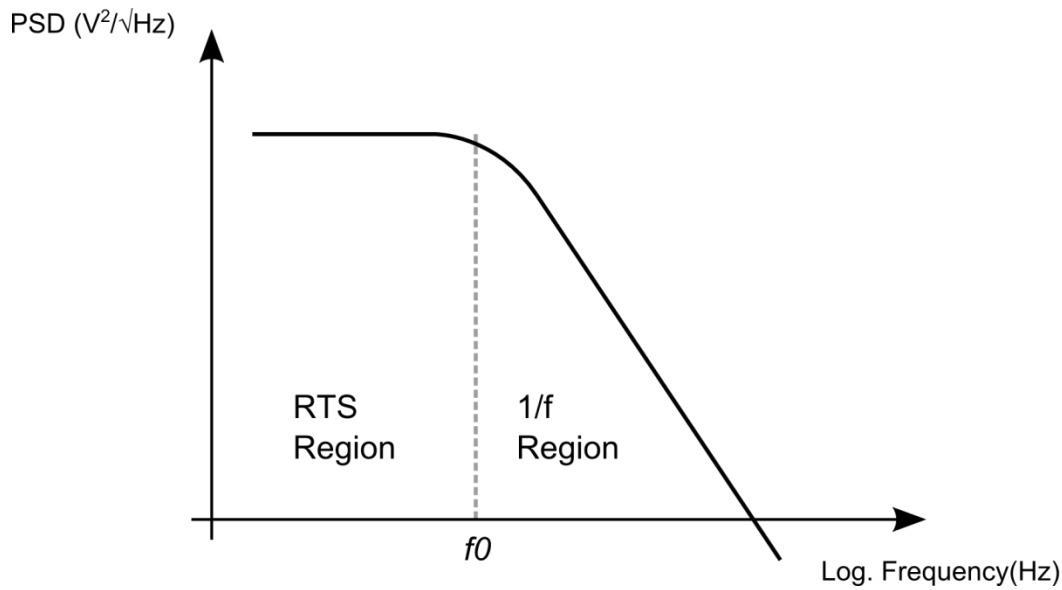


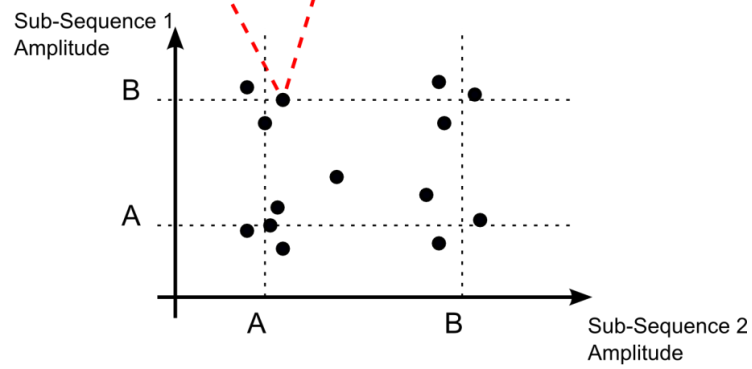
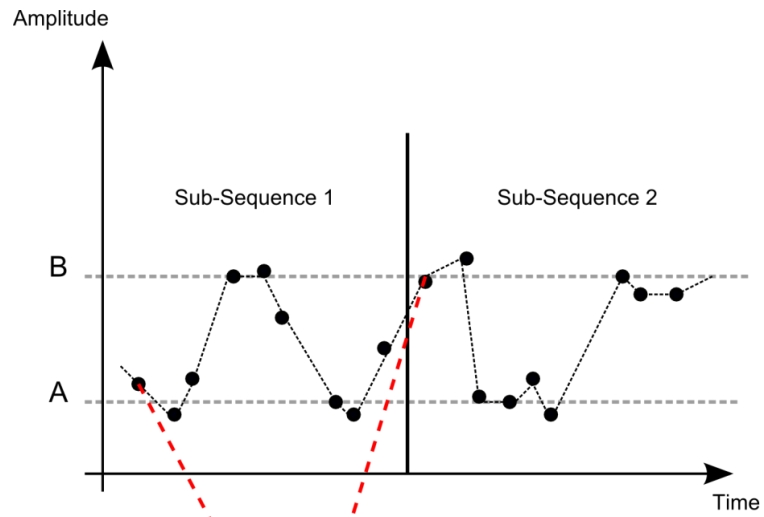
Figure 2.9: Conceptual Lorentzian noise frequency spectrum for RTS and Flicker noise [38].

RTS noise has a great impact on circuits working at low frequencies. RTS can be quantified by its corner frequency or integrated RMS noise power. However, due to its transient nature, it can be intuitive to quantify RTS by time domain methods. Noise Scattering Pattern (NSP) is an effective RTS quantification method, which is proposed in the work [39]. Figure 2.10 (a) illustrates the principle behind the NSP method. In order to apply NSP method, data should be digitized using a high resolution ADC. Obtained digital data sequence $s[x]$ with N data points is divided into two sub-sequences that have same number of data points;

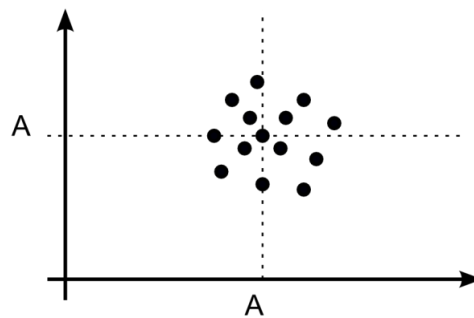
Sequence 1: $s_1[x] = s[m]$ where, $m=1, 2, \dots, N/2$

Sequence 2: $s_2[x] = s[k]$ where, $k=N/2 + 1, N/2 + 2, \dots, N$

Then, all data points from sequence 1 and sequence 2 are matched one by one eg. $s_1(1)$ to $s_2(N/2+1)$, $s_1(2)$ to $s_2(N/2+2)$ and so on. Each matched data points are plotted on a XY histogram, which is called scatter plot. The scatter plot reveals the levels that involved in the RTS noise process due to the clustering on certain points. Besides, the plot gives idea about level transition directions and level durations. Figure 2.10 (b) shows a scatter plot for a Gaussian distributed noise, which does not include RTS noise.



(a)



(b)

Figure 2.10: NSP method illustrated; (a) Data sequence is mapped on to a scatter plot revealing impact of the RTS noise. (b) Hypothetical scatter plot of a Gaussian noise process, which is differing from RTS process by single level clustering [39].

2.5.2. Test Setup

In order to obtain noise data two different measurement methods are utilized. Noise is both measured in time domain and frequency domain. In the time domain measurements, a low noise LTC2379 18-Bit ADC board is used and in the frequency domain measurements, Agilent 35670A Digital Signal Analyzer (DSA) is used. Figure 2.11 shows the used noise setup for the measurements. The battery and test setup circuit are placed into a Faraday cage, which is ground shielded and blocking interference from the environment.

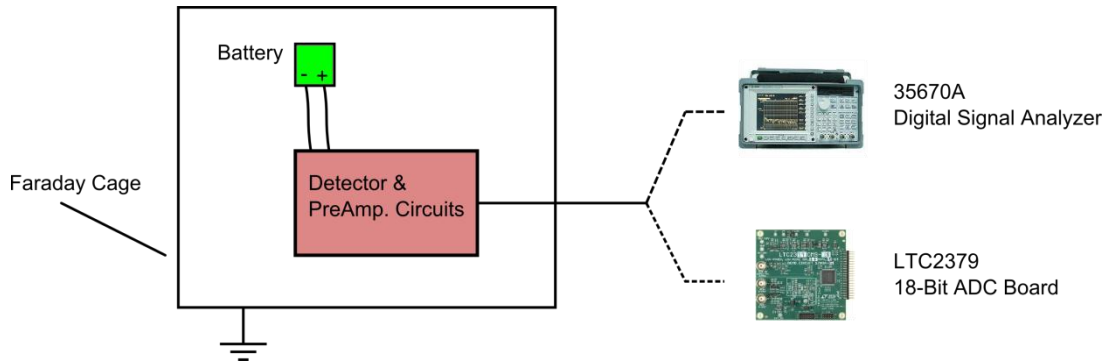


Figure 2.11: Detector noise measurement configuration.

A low noise amplifier circuit is implemented for amplifying detector signal. Amplification is needed in order to bring the amplitude of detector noise higher than the measurement device noise floor. Figure 2.12 gives the schematic for the amplifier circuit. In the preamplifier, two gain stages are used. This structure ensured the amplifier stability with the increased measurement bandwidth. Gain stages consist of a non-inverting connected NE5532 opamp, which have $5 \text{ nV}/\sqrt{\text{Hz}}$ input referred noise at 1 kHz [40]. Circuit is designed to have total gain 1100. Figure 2.13 gives the measured gain of the noise preamplifier against frequency. The amplifier circuit has a bandwidth of 50 kHz.

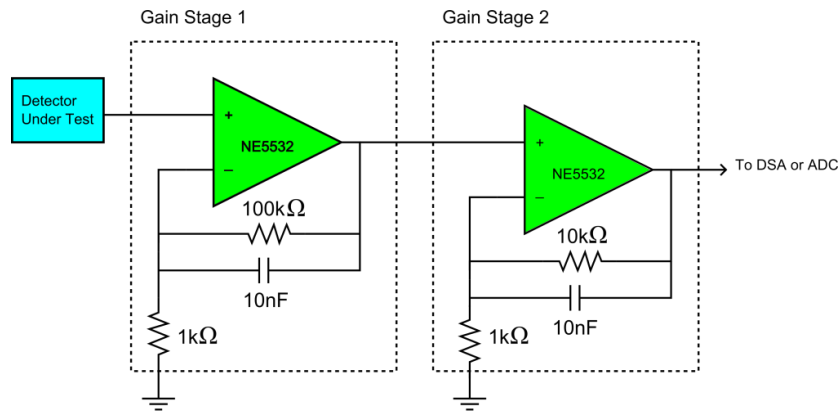


Figure 2.12: Noise setup preamplifier circuit.

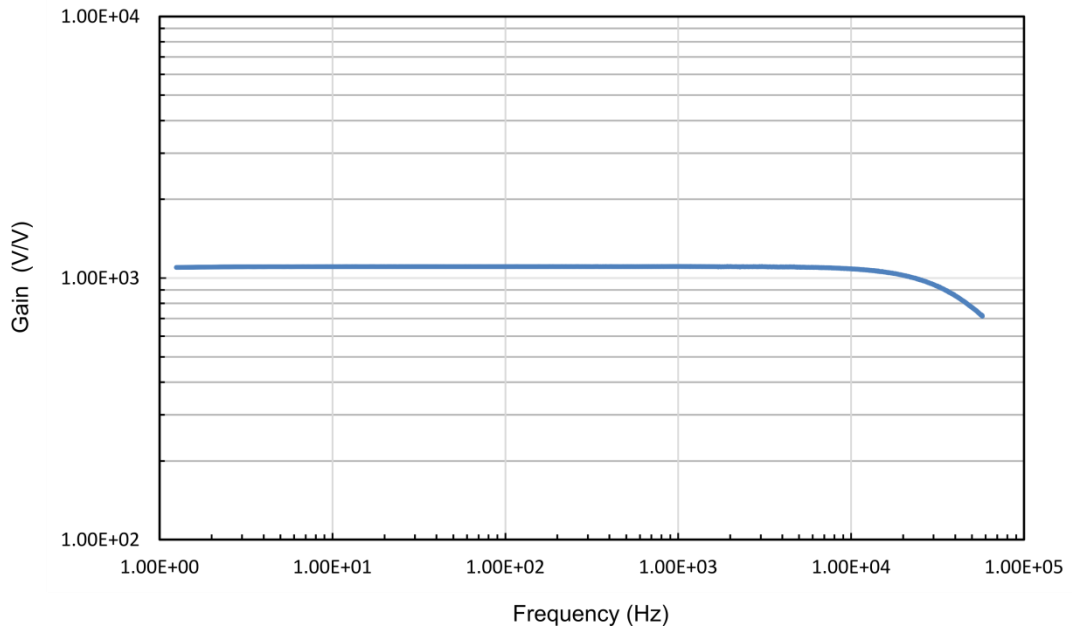


Figure 2.13: Measured gain spectrum of the noise amplifier

Detector biasing is another challenging issue for the noise measurement of diode detectors. Each current biased diode has a DC voltage drop of 0.7-0.8 Volts. For 70 μm detectors, four serially connected diodes adds up to a detector voltage of nearly 3.2-3.3V. This high DC voltage makes the detector signal difficult to read causing amplifier saturation. One way to alleviate this problem is using a DC blocking filter. The disadvantage of this method is limited bandwidth and amplifier saturation due to input leakage current of opamps. Figure 2.14 shows the detector biasing circuit that is used in the noise tests of 70 μm detectors. In the circuit, two detectors are used instead of one. These two detectors are biased with positive and negative battery voltages.

By that way, middle node of the two detectors came to the 0V, which does not saturate the amplifier output. Two potentiometers (R1 and R4 in Figure Figure 2.14) are used for adjusting the bias currents and resetting the DC offset of the measurement node. These potentiometers are selected to be lower values in order to decrease their noise contribution. R3 and R2 are also used for adjusting the bias currents and providing a linear voltage biasing. Due to parallel combination of two detectors in AC domain, measured noise is equivalent to the one detector noise divided by $\sqrt{2}$ in this method.

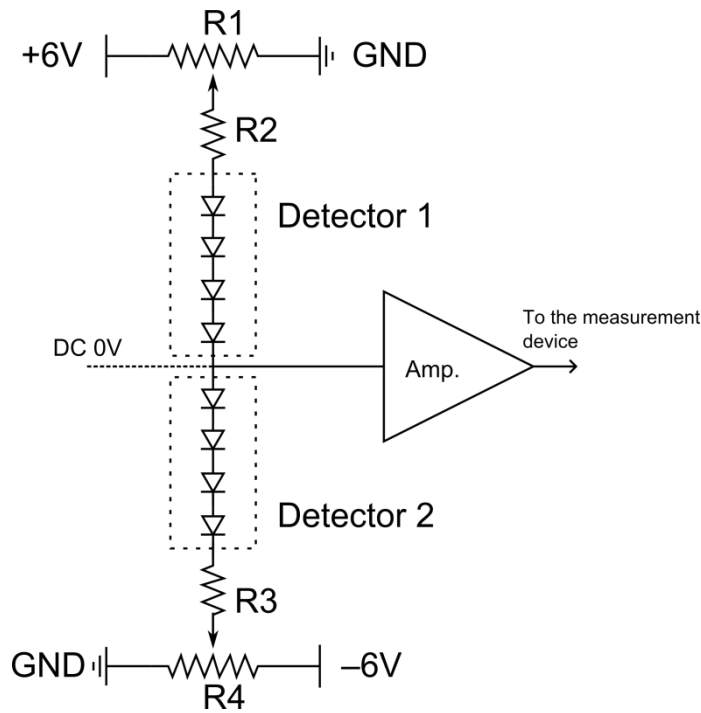


Figure 2.14: Noise setup biasing circuit.

2.5.3. Frequency Domain Measurement Results

Tests have been conducted using the setup that is introduced in Section 2.5.2. Detector measurement results are obtained and presented for the parallel combination of two detectors. Firstly, input referred noise of the noise setup has been measured. In this measurement, detectors are removed and replaced with shorting wires. By that way, noise of the biasing circuit is also included into overall input referred noise. Figure 2.15 gives the input referred voltage noise spectral density of the preamplifier circuit.

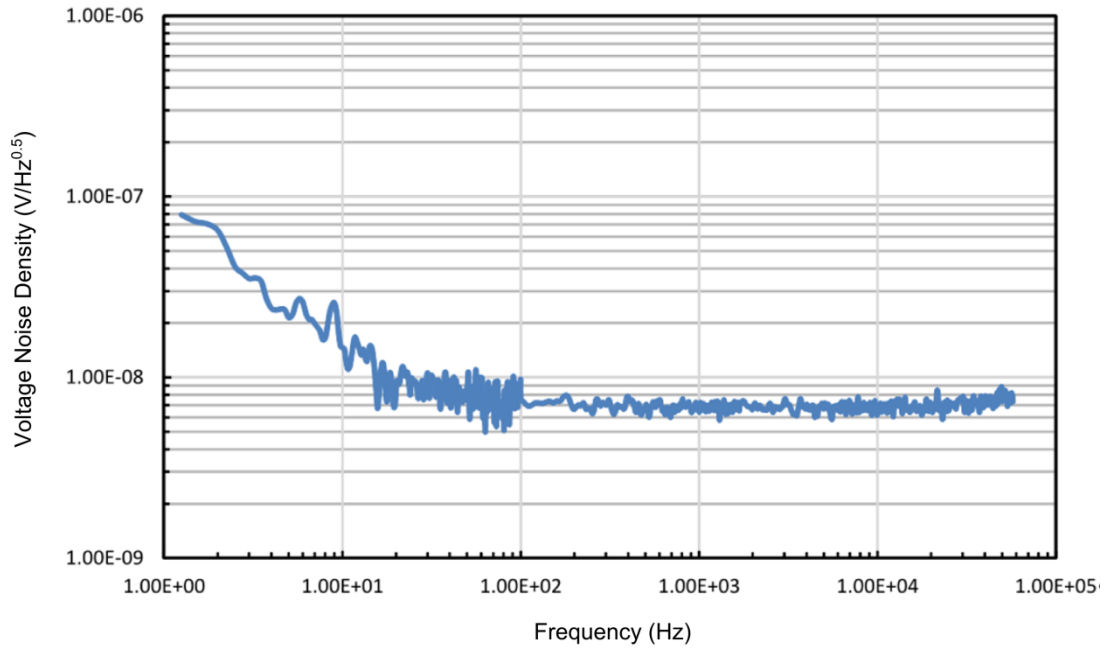


Figure 2.15: Input referred voltage noise spectral density of the preamplifier when no detectors are present.

In order to determine the reliability of noise setup, noise of an 110k Ω discrete resistor was measured. The 110k Ω resistance is obtained by replacing the detectors with 220 k Ω discrete resistors in the circuit, which is shown in Figure 2.14. Figure 2.16 gives the measured noise and theoretical noise floor for the tested resistor. Noise floor of the resistor is quite compatible with the theoretical floor that is about 45 nV/ $\sqrt{\text{Hz}}$. Noise floor is calculated for only the thermal noise component. The tested resistor has a flicker noise corner of nearly 800 Hz.

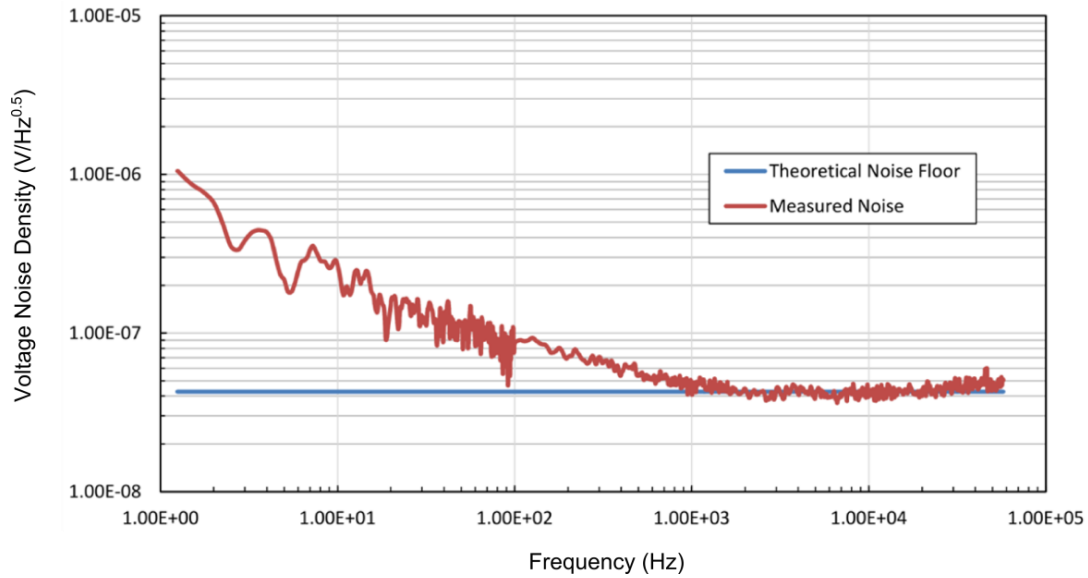


Figure 2.16: Measured noise of a 110 k Ω discrete resistor given with the theoretical noise floor. Noise floor for the measurement and theory is equal to $45 \text{ nV}/\sqrt{\text{Hz}}$.

Using the test setup, a set of discrete diodes is measured. In this measurement, 4 discrete diodes are connected serially mimicking the detector diodes. Discrete diodes are biased 2 μA , which is the same current used in the detector biasing of FPA chips. Figure 2.17 shows the measured noise and theoretical noise floor for the discrete diodes. Measured noise floor for discrete diode is $23 \text{ nV}/\sqrt{\text{Hz}}$, while theoretical noise floor is $16 \text{ nV}/\sqrt{\text{Hz}}$. For the theoretical noise of diodes only shot noise component is calculated.

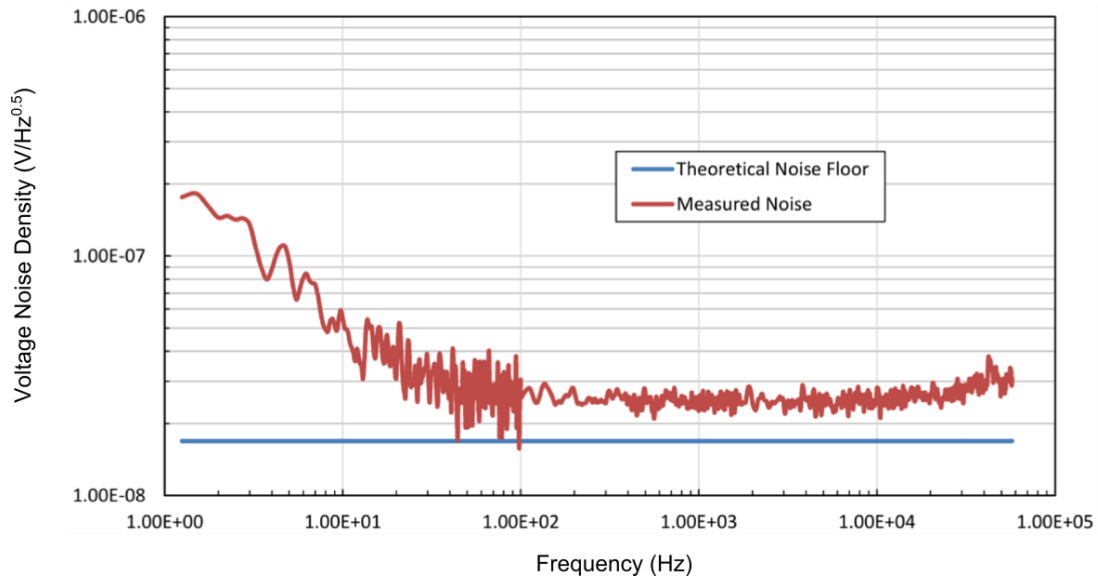


Figure 2.17: Measured noise of a discrete diode given with the theoretical noise floor.

After the discrete resistor and diode measurements, low-cost microbolometer pixel detectors are measured. In the measurement, non-suspended test detectors are used. The connection of detectors is made according to the Figure 2.14. Potentiometers are adjusted in order to pass 2 μA current from the detectors. Figure 2.18 shows the measurement result of the first set of the detectors (Sample #1).

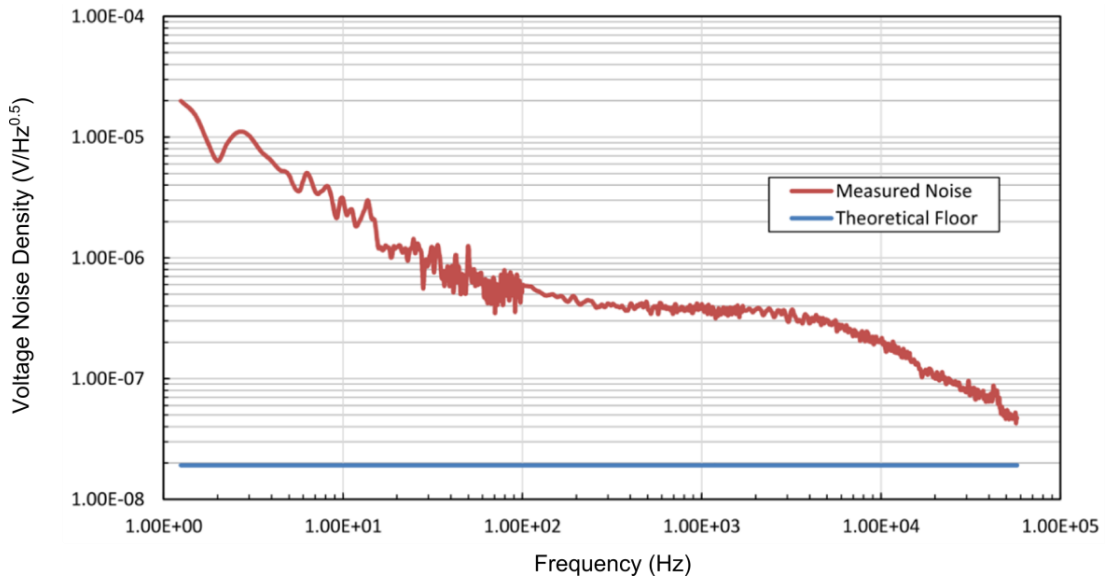


Figure 2.18: Measured noise spectrum of the detector Sample #1 given with the theoretical floor.

From the Figure 2.17 and Figure 2.18 it can be understood that detector samples have a noise characteristic that is different from the discrete diode. The noise spectrum of detector Sample #1 has a flat region after around 200 Hz, which defines the RTS noise corner. The $1/f$ noise corner is located at a frequency point higher than the 50 kHz which is limited by the measurement device (Dynamic Signal Analyzer).

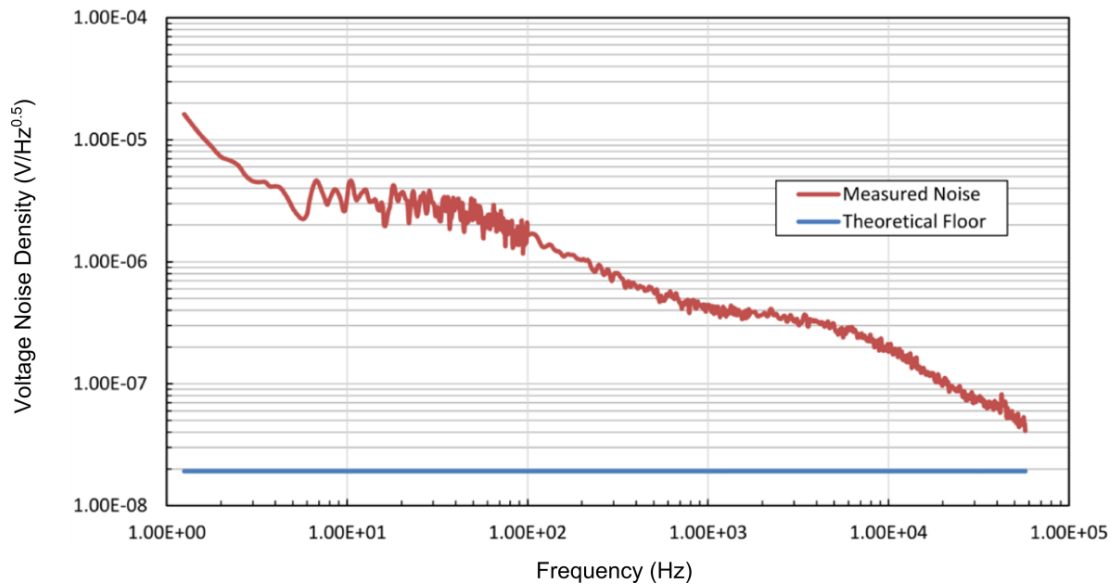


Figure 2.19: Measured noise spectrum of the detector Sample #2 given with the theoretical floor.

Figure 2.19 shows the measurement result of the second set of the detectors (Sample #2) together with the theoretical noise floor. Sample #2 has two flat regions implying that two different RTS noise processes involved. The corner frequency for these RTS floor is around 200 Hz. Again, the $1/f$ noise corner frequency is beyond the limit of the measurement device, which is 50 kHz.

Figure 2.20 shows the measurement result of the third set of detectors (Sample #3) together with the theoretical noise floor. This detector, differently from Sample #1 and Sample #2, does not have RTS flat regions and have a characteristic more similar to the resistor noise. Despite the smooth noise characteristic of Sample #3, its $1/f$ noise corner is at very high levels compared to the discrete diode noise. The corner frequency for that measurement is 800 Hz where the discrete diode has a corner frequency around 100 Hz.

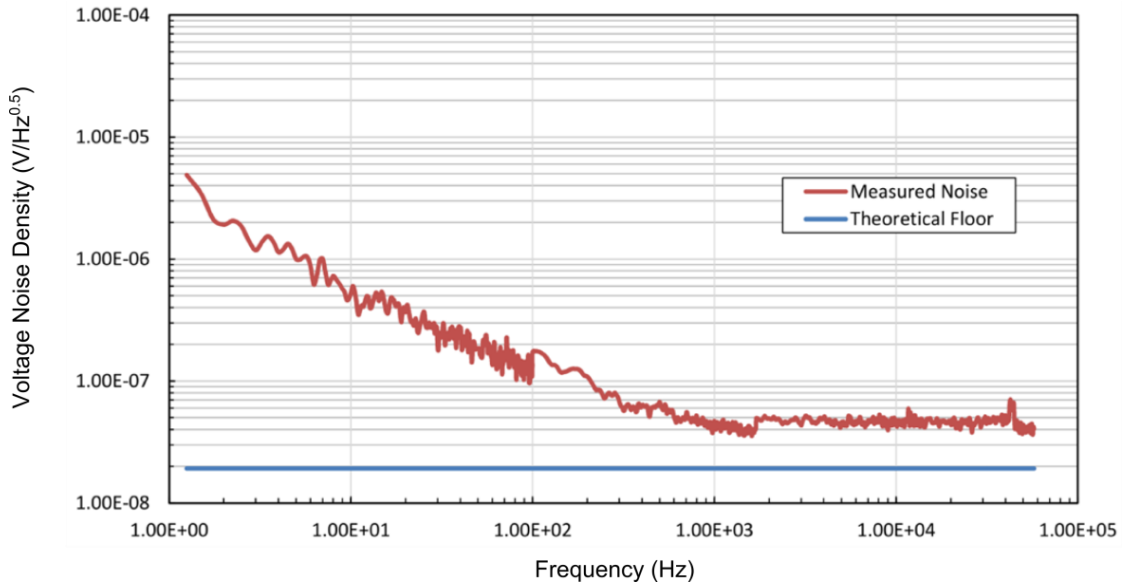


Figure 2.20: Measured noise spectrum of the detector Sample #3 given with the theoretical floor.

The noise voltage RMS is calculated for each measurement and given in the Table 2.3. Bandwidth for the RMS voltage noise is selected to be 10 kHz, which corresponds to 50 μ s integration time.

Table 2.3: RMS voltage noises for DSA measurements.

Sample	Measured RMS Noise (μ V _{RMS}) @ 10kHz Band	Theoretical RMS Noise (μ V _{RMS}) @ 10 kHz Band
110 k Ω	4.73	4.27
Discrete Diodes	2.54	1.69
Detector Sample #1	36.25	1.92
Detector Sample #2	44.16	1.92
Detector Sample #3	6.60	1.92

It can be observed from that 110k Ω can be measured with a good accuracy verifying the test setup. Discrete diode set have a measured noise higher than the theoretical value. This can be caused by the limitation of noise setup and the biasing circuit. The detector samples have much higher RMS voltage noises than the theoretical ones. The RMS voltages of detector samples are dominated by the RTS mechanisms that cause flat regions in the noise spectrum.

2.5.4. Time Domain Measurement Results

The transient measurements have been done on detector samples in order to understand the time domain characteristics of RTS noise mechanism. Transient measurements have been conducted using the ADC board setup that is introduced in Section 2.5.2. The LTC2379 16-bit, low noise ADC is utilized on the board. Detector noise signal is sampled with 500 kHz frequency. The sampled data is filtered in MATLAB using a 50-sample moving average filter to obtain a smoother data. The average values of measurements are extracted in order to cancel out the DC component. Noise Scattering Pattern (NSP) method is applied on transient measurement results for a better understanding of RTS characteristics of noise data. The NSP method is explained in Section 2.5.1 in detail.

Figure 2.21 shows the transient measurement result of detector set 110k Ω resistor. Figure 2.22 shows the NSP plot for the 110 k Ω resistor. The NSP dots are distributed normally around the average that is shown with a red dot on the figure. Average is found by calculating the center of mass of the scattered samples. Such a distribution is typical to the device noise measurements where the RTS is not the dominating noise process.

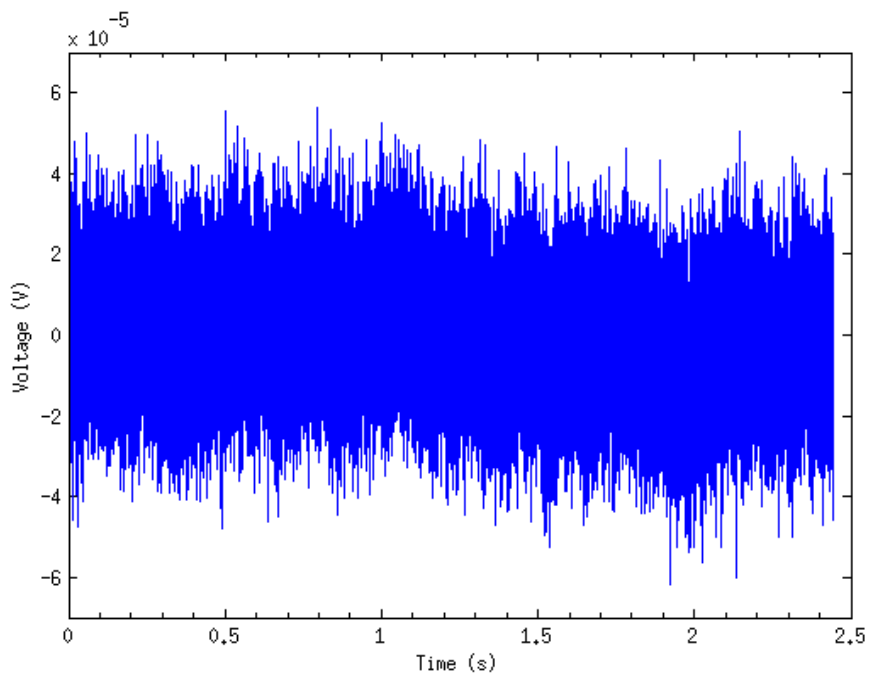


Figure 2.21: Transient measurement result of a 110 k Ω discrete resistor. Red dot shows the center of mass for the scattered samples.

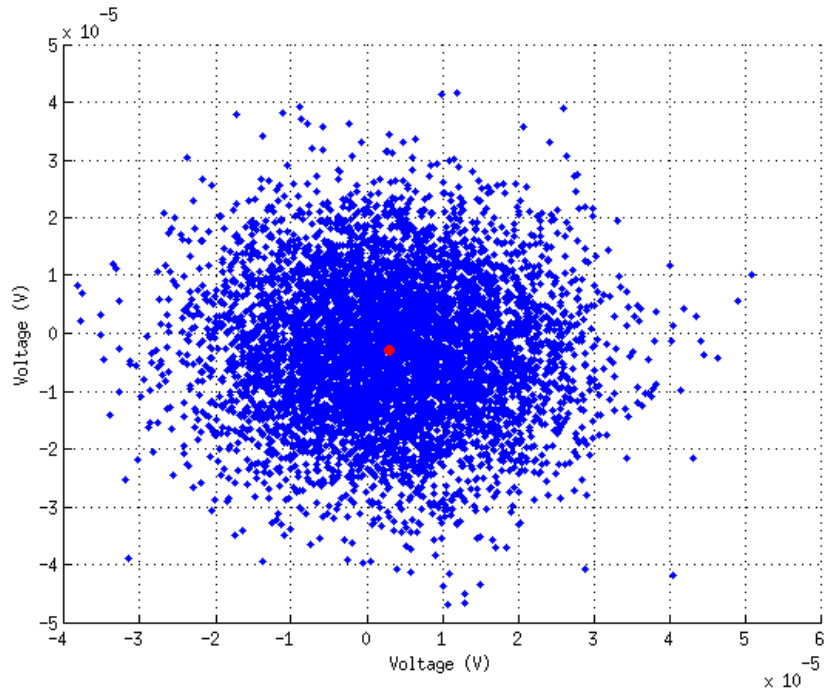


Figure 2.22: Noise Scattering Pattern (NSP) plot for the 110 kΩ discrete resistor transient measurement. Red dot shows the center of mass for the scattered samples.

Figure 2.23 shows the transient noise measurement result for discrete diodes. NSP plot for the discrete diodes is given in the Figure 2.24. In the measurement, 4 serially connected discrete diodes are utilized. Similar to the resistors, NSP characteristic of the diode measurement shows normal distribution around the average.

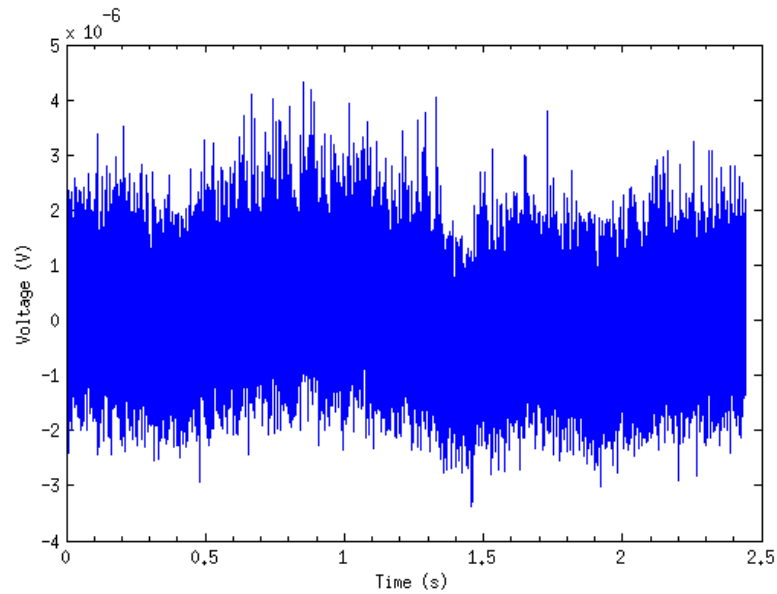


Figure 2.23: Transient measurement result of discrete diodes

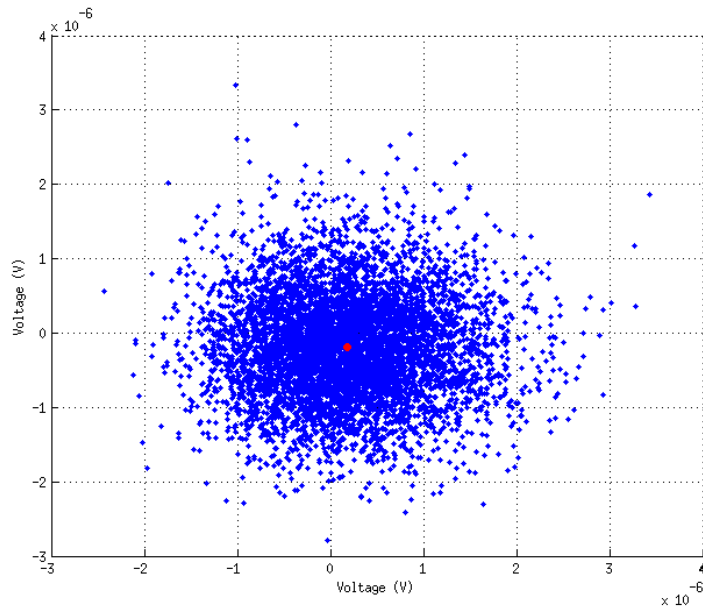


Figure 2.24: Noise Scattering Pattern (NSP) plot for the discrete diode transient measurement. Red dot shows the center of mass for the scattered samples.

After the measurements of discrete resistors and diodes, the 70 μm detector samples have been measured. Figure 2.25 shows the transient measurement result of detector set Sample #1. Figure 2.26 shows the NSP plot for the Sample #1 measurement.

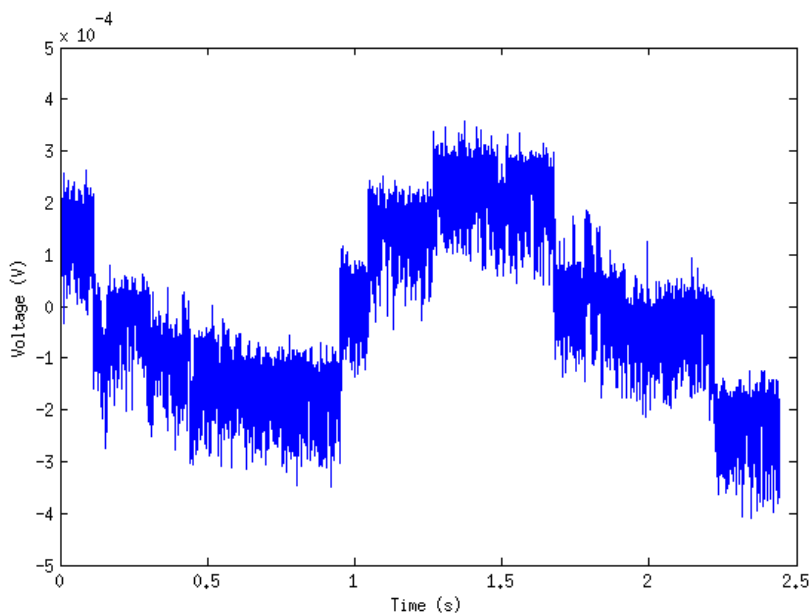


Figure 2.25: Transient measurement result of detector set Sample #1.

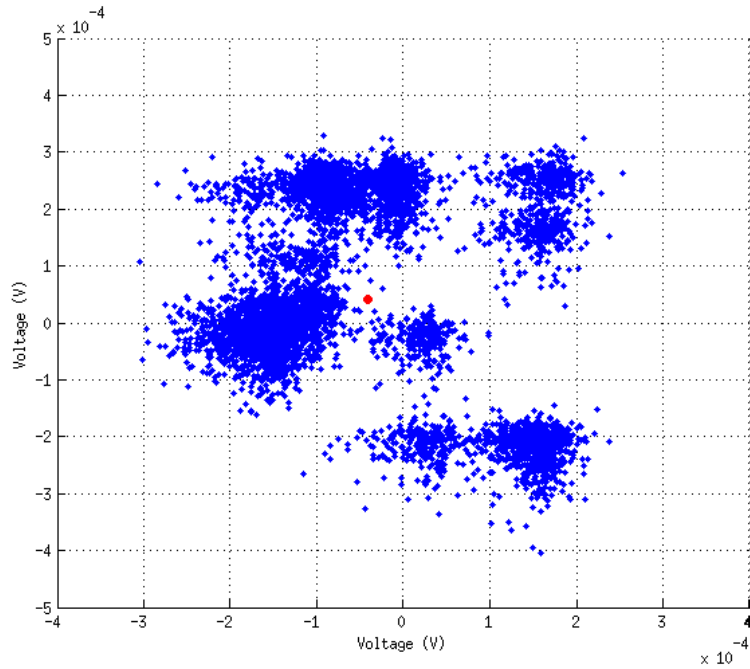


Figure 2.26: Noise Scattering Pattern (NSP) plot for the Sample #1 transient measurement. Red dot shows the center of mass for the scattered samples.

The transient characteristic of Sample #1 exhibits the several levels of RTS noise. The level changes occur in long time periods where their impact can be observed at the low frequency region of the spectrum. The level change time periods are observed in the range of milliseconds to minutes. The NSP plot reveals the levels that are involved in the RTS process. The biggest cluster is around $(0, -2 \times 10^{-4})$ coordinates, which implies the two main levels that are involved in RTS are $0V$ and $-2 \times 10^{-4} V$. The secondary levels are 2×10^{-4} and -1×10^{-4} , which constitute the second biggest cluster. Other clusters show the minor levels that are involved in the RTS noise process.

Figure 2.27 shows the transient measurement result of Sample #2. NSP plot for the sample is given in Figure 2.28. The Sample #2's RTS noise has a little different characteristic from the Sample #1 where the levels are more distinct and transitions are sharper. In the NSP plot the levels can be observed. The vertical clustering around the X-axis voltage $0.5 \times 10^{-4} V$ shows that, this voltage is the major level.

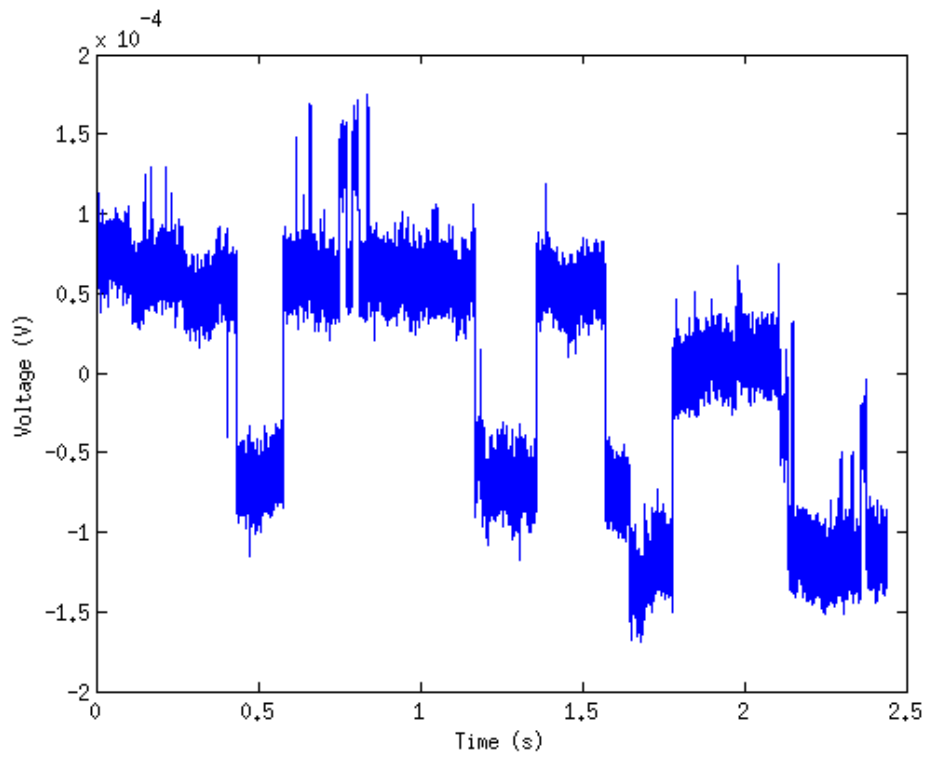


Figure 2.27: Transient measurement result of detector set Sample #2.

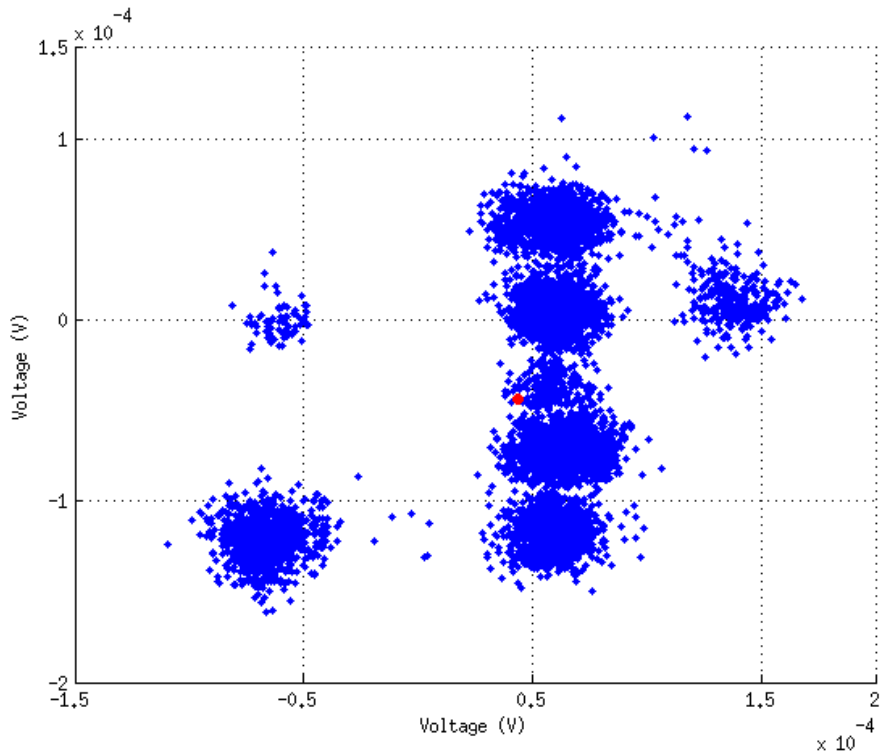


Figure 2.28: Noise Scattering Pattern (NSP) plot for the Sample #2 transient measurement. Red dot shows the center of mass for the scattered samples.

Figure 2.29 shows the transient measurement result of Sample #3. NSP plot for the sample measurement is given in Figure 2.30. Differently from Sample #1 and Sample #2, Sample #3's RTS noise characteristic exhibits smoother level transitions with fewer amplitudes. In the NSP plot two major clusters can be observed that are related to two major levels involved in the RTS noise process. These two clusters are not distinctly apart from each other implying that Gaussian noise has a higher impact than the RTS noise on the overall noise.

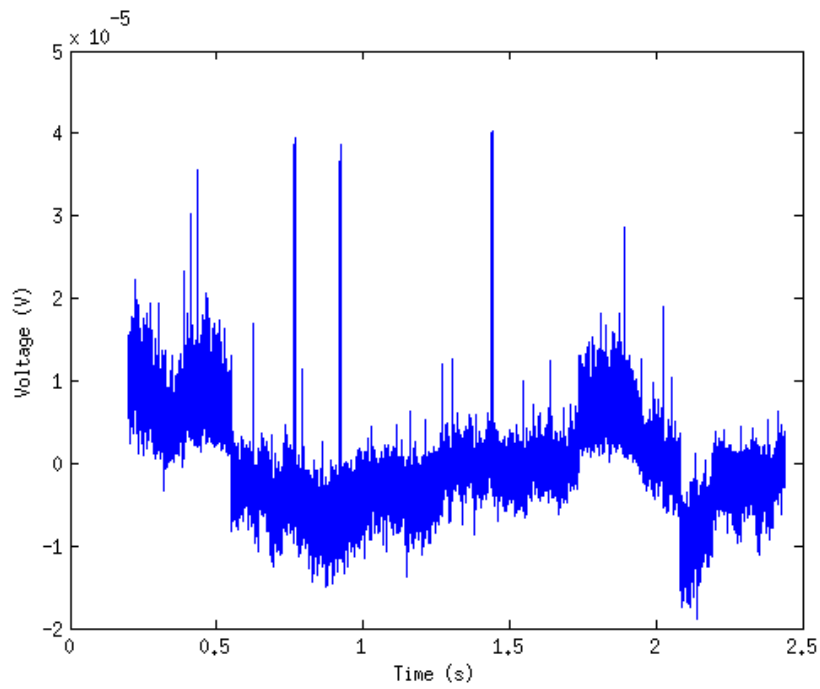


Figure 2.29: Transient measurement result of detector set Sample #3.

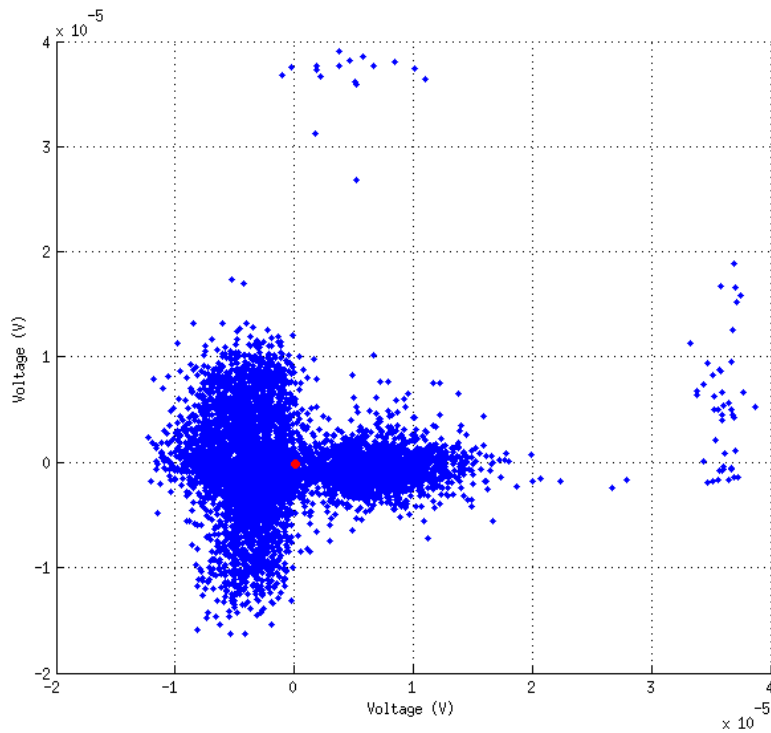


Figure 2.30: Noise Scattering Pattern (NSP) plot for the Sample #3 transient measurement. Red dot shows the center of mass for the scattered samples.

2.5.5. Wafer Level RTS Noise Test

In the previous section transient noise measurements of individual 70 μm detector samples have been conducted. These measurements gave idea about the nature of RTS noise process that is observed in the detectors. In this section, wafer-level measurement results of detector samples have been shown. With the wafer level measurements, the distribution of the RTS noise impact through the wafer is obtained. Figure 2.31 shows the test setup that is used in the measurements. The detectors are probed using the PAV200 Probe Station. Figure 2.32 gives a photo of the PAV200 Station while testing.

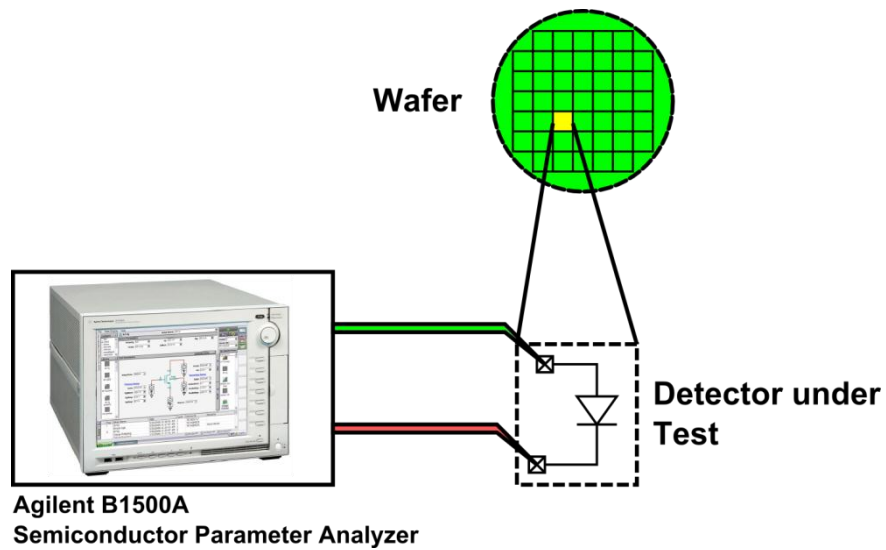


Figure 2.31: Test setup for wafer level measurements.

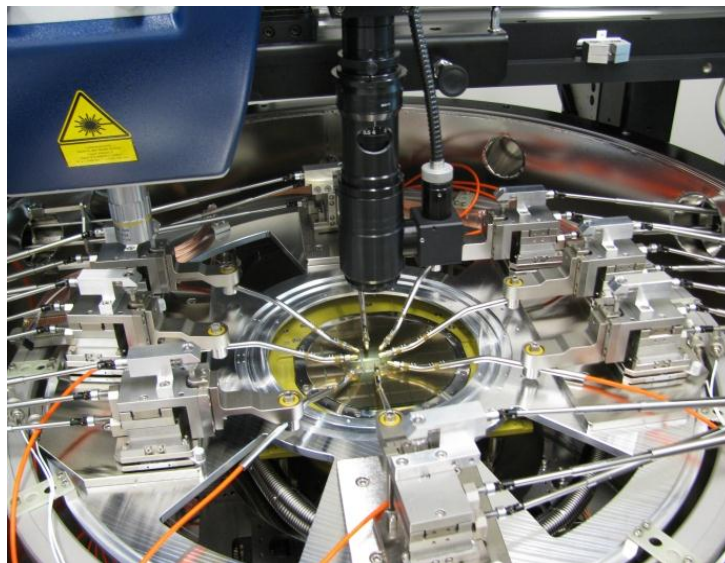


Figure 2.32: A photo of the PAV200 Probe Station, which is used in the probe tests.

Agilent B1500A Semiconductor Parameter Analyzer is used as the measurements device, which can bias detectors with current and observe voltage in the time domain. The RTS noise performance of the measured wafer is evaluated using the Noise Scattering Pattern (NSP) method.

Figure 2.33 gives the wafer map obtained from the measurements. The gray filled dies have a RTS predominant noise characteristic while yellow filled dies have a little or very low RTS impact. The distribution of dies along the wafer is quite random without posing any pattern.

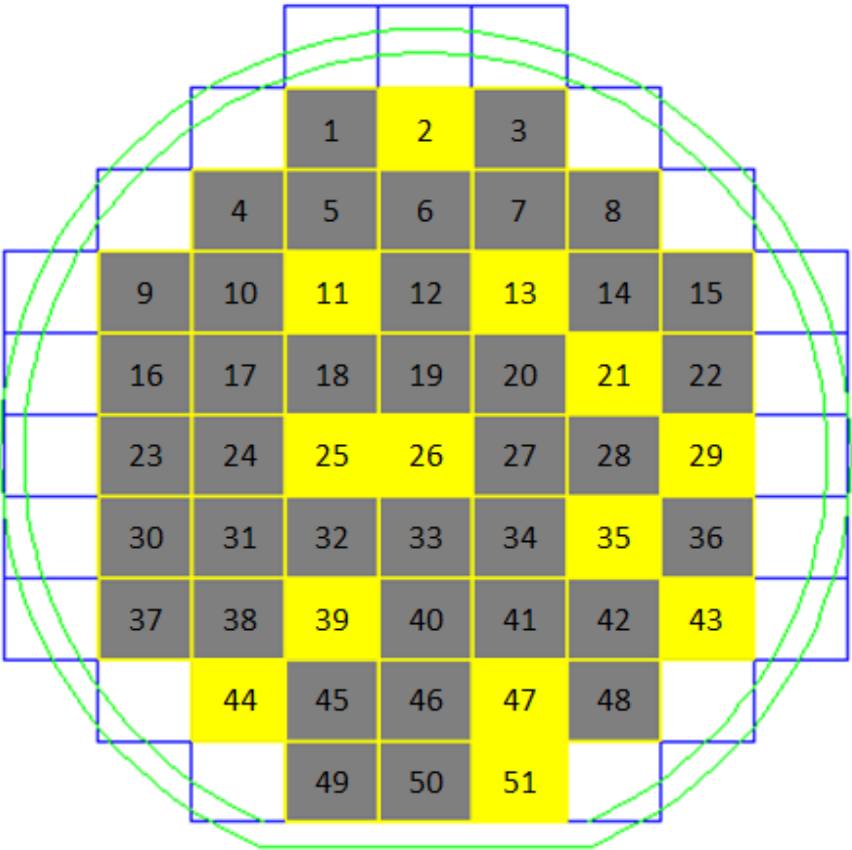


Figure 2.33: Wafer map for RTS noise measurements. Gray filled dies exhibit high level RTS noise activity while, yellow filled dies represent very low level or no RTS noise activity.

2.6. Conclusion

In this chapter, the performance of 70 μm low-cost microbolometer detectors is characterized with several tests. The characterization tests include I-V curve tests, temperature coefficient (TC) measurement, thermal conductance (Gth) measurement, and noise measurement. Parameters extracted from the I-V curve and arm resistance is found to be 7127 Ω . TC is measured using a chamber and found -6 mV/K for 2 μA bias current. Thermal conductance is found 202 nW/K while the simulated value is 240 nW/K. The absorption is measured using FTIR method. Average absorption is found to be 78 %.

Finally, the noise is characterized. In noise characterizations both frequency domain and time domain measurement methods are utilized. Spectral characteristics of detector noise are obtained by frequency domain measurements. The RTS type noise process is found to be predominant degrading factor of detector performance. RTS noise impact is evaluated in the time domain measurements using the Noise Scattering Pattern (NSP) method. Along the die level tests, a wafer level test has been also done for detectors. A wafer map is obtained for the distribution of the detectors according to their RTS noise impact.

CHAPTER 3

DEVELOPMENT AND TESTS OF FIRST GENERATION LOW-COST SENSOR ARRAY READOUT ELECTRONICS

This chapter presents the development efforts of first generation low-cost uncooled microbolometer readout electronics, which incorporate 70 μm pitch detector pixels in QCIF (160x120) FPA arrangement.

The first 70 μm pixel pitch low-cost detectors are designed, characterized, and realized in previous works conducted at the METU-MEMS Center. Despite its very limited performance, first infrared imaging could be possible with the 128x128 FPA presented in [24]. The QCIF (160x120) resolution infrared imaging FPA developed in [25], which had better performance values than previous works making it suitable for certain commercial applications.

In scope of this thesis, further improvements have been achieved on readout electronics of 70 μm detector arrays in order to increase their performance. These improvements targeted the performance limiting issues that are described in Chapter 2. The QCIF sensor array in [25] constituted a basis, and improvements have been made in the scope of this thesis as design revisions by altering the readout electronics architecture. Three successive design revisions have been undertaken and each of them has been tested after their CMOS fabrication.

Section 3.1 gives information about the details of the 160x120 sensor array, which is previously developed in [25]. Section 3.2 presents the first design revision of the 160x120 sensor array and the test results. This revision aims to decrease overall system noise and chip power dissipation. Section 3.3 presents the second of first design revision of the 160x120 sensor array and the test results. This design revision aims to eliminate the column noise caused by the Random Telegraph Signal (RTS) noise. Section 3.4 presents the third design revision of the 160x120 sensor array and the test results. This design revision aims to fix temperature drift and system noise problem, which are observed in the previous design revision. Finally, Section 3.5 summarizes the revisions of the 160x120 sensor array and compares their outcomes.

3.1. First Generation 160x120 Low-Cost Sensor

First generation low-cost sensor consists of a 160x120 (QCIF) 70 μm pixel pitch FPA and integrated readout electronics, which is developed at the METU-MEMS Research and Application Center [25]. Chip is fabricated using the standart CMOS technology enabling the monolithic integration of readout electronics and the pixel array. Figure 3.1 shows the top-level placement of chip blocks. The chip has 80 analog column readouts for processing the analog signals where each two pixel columns is read by column readout. Vertical, horizontal, and output scanners are digital circuits, which are responsible for scanning the detector array. Vertical scanner selects the detector row to be powered up for the signal integration and readout. Horizontal scanner multiplexes the two detector column signal outputs into a readout channel input. The output scanner passes the integrated detector signal, which is ready at the end of the readout channel, to the chip analog output [25].

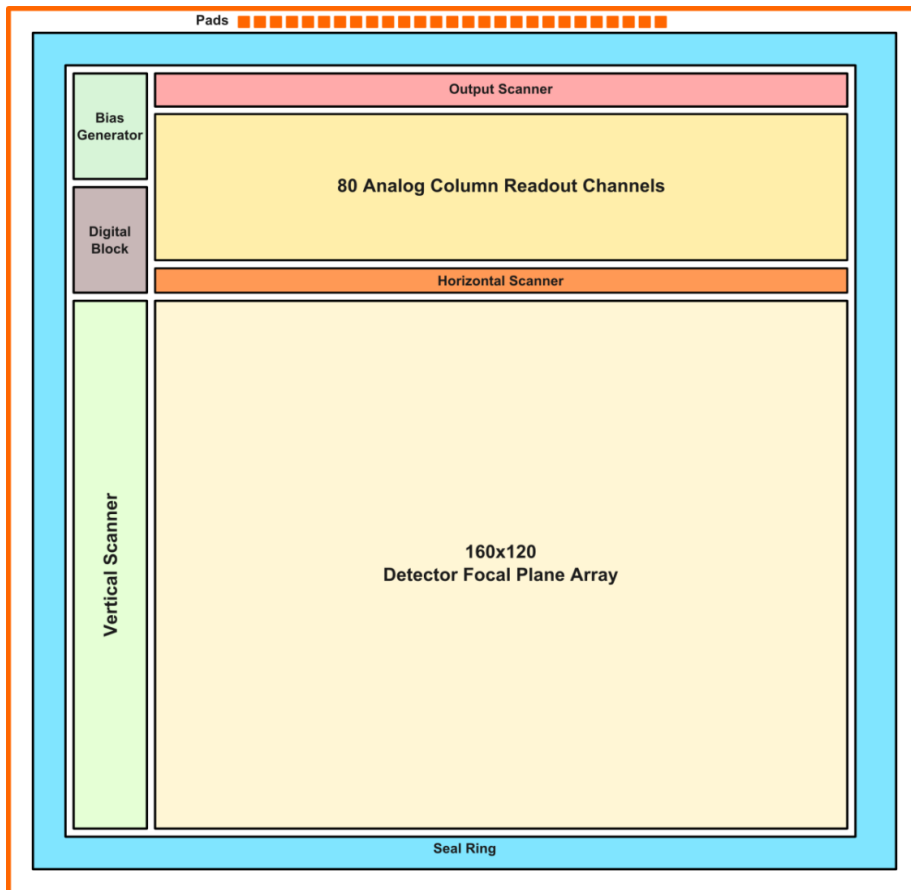


Figure 3.1: Block diagram of first generation microbolometer detector array chip [25].

The timing of all digital circuits is generated by the digital block. Digital block is also responsible for serial programming of the chip. Programming enables the flexible changing of the chip options [25].

Analog circuits at the readout channels need bias voltages and currents for proper operation. These voltages and currents are generated by the bias generator block. Bias generator consists of Digital to Analog Converters (DACs) that can be programmed via the serial digital interface (SPI).

Infrared response was obtained from first generation 160x120 70 μm pixel pitch sensors successfully [25]. The peak NETD for the measurement is 350 mK for F/1.0 optics. Figure 3.2 shows a thermal image obtained from the sensor [25].



Figure 3.2: A thermal image obtained from the sensor [25].

3.2. First Design Revision for 160x120 Low-Cost Sensor

As explained in the previous section, the 160x120 low-cost microbolometer detector array can perform imaging with a sufficient quality. Despite its success, it brought various drawbacks that limit its performance. In this section, the first revision effort for the 160x120 detector array is explained. Since, low-cost detector is designed to be used in portable camera systems power dissipation is a vitally important parameter. Besides, high power operation tends to degrade the system noise performance and increase the dissipated heat. Section 3.2.1 explains the power dissipation optimization with the simulation results. Section 3.2.2 presents the test setup and results for the revised chip.

3.2.1. Power Dissipation Optimization

The biggest part of the low-cost infrared sensor's total power dissipation is the contribution of analog readout circuits. High power dissipation at the analog readout is related to the image noise due to the phenomenon that is called supply bounce. Figure 3.3 shows the electrical representation of the noise injection paths.

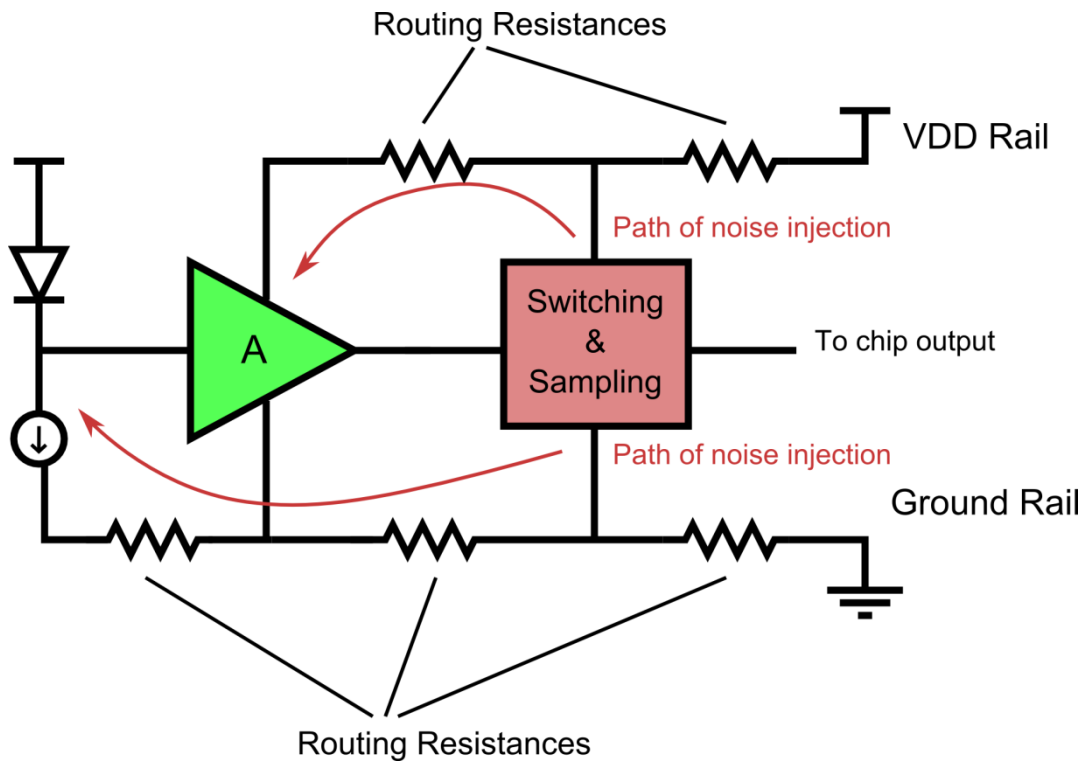


Figure 3.3: Noise injection paths in column readout circuits due to the supply bounce.

The column readout consists of analog circuits in order to process analog signals. The power need of these blocks is supplied by the VDD and GND rail routings that have finite resistances. The analog blocks draw transient currents from the supply during certain readout switching times. These transient currents bounce the supply and injected as noise to the more sensitive regions of readout circuit. The most sensitive part of the readout is the detector front-end where the injected noise is amplified and presented to the output with the highest gain. Because, the transient currents increase, the supply bounce tends to have higher impact when the blocks have higher power dissipations.

In the analog readout of the sensor FPA, the dominating power sink is the Operational Amplifier (Opamp) circuits. With the first revision, power dissipation is reduced by changing the circuit topologies of the opamps in the column readout. Power dissipation is simulated for the older and newer design. Table 3.1 shows the power dissipation simulation results for the opamps used in the column readout. The total power dissipation

for the single column readout is decreased to 25 mW from 132 mW with the new design revision.

Table 3.1: Readout opamps power dissipation table for the older design and the revised design.

	First Stage Opamp Power Dissipation	Second Stage Opamp Power Dissipation	Opamp Power Dissipation (1 Readout)	Total Opamp Power Dissipation (80 Readout)
First Version	825 μ W	825 μ W	1650 μ W	132 mW
Revised Version	175 μ W	138 μ W	313 μ W	25 mW

3.2.2. Test Setup & Results

Figure 3.4 shows the block diagram of the test setup. Data gathering and programming of the chip is done by a PC. A Field Programmable Gate Array (FPGA) is used as a core controller, which establishes the interface between the PC and test setup blocks. The analog image data at the chip output is digitized using a 14-bit A/D converter (ADC) and the digital image data is sent to PC using the FPGA. The timing of the ADC and the image sensor chip is performed by the FPGA. Imaging sensor chip also needs analog bias voltages for the operation of its analog circuits. These analog bias voltages are fed by a D/A converter, which is programmed by the FPGA. FPGA is also used for the digital programming of the imaging sensor chip features. The power need of blocks is supplied by the power regulators block.

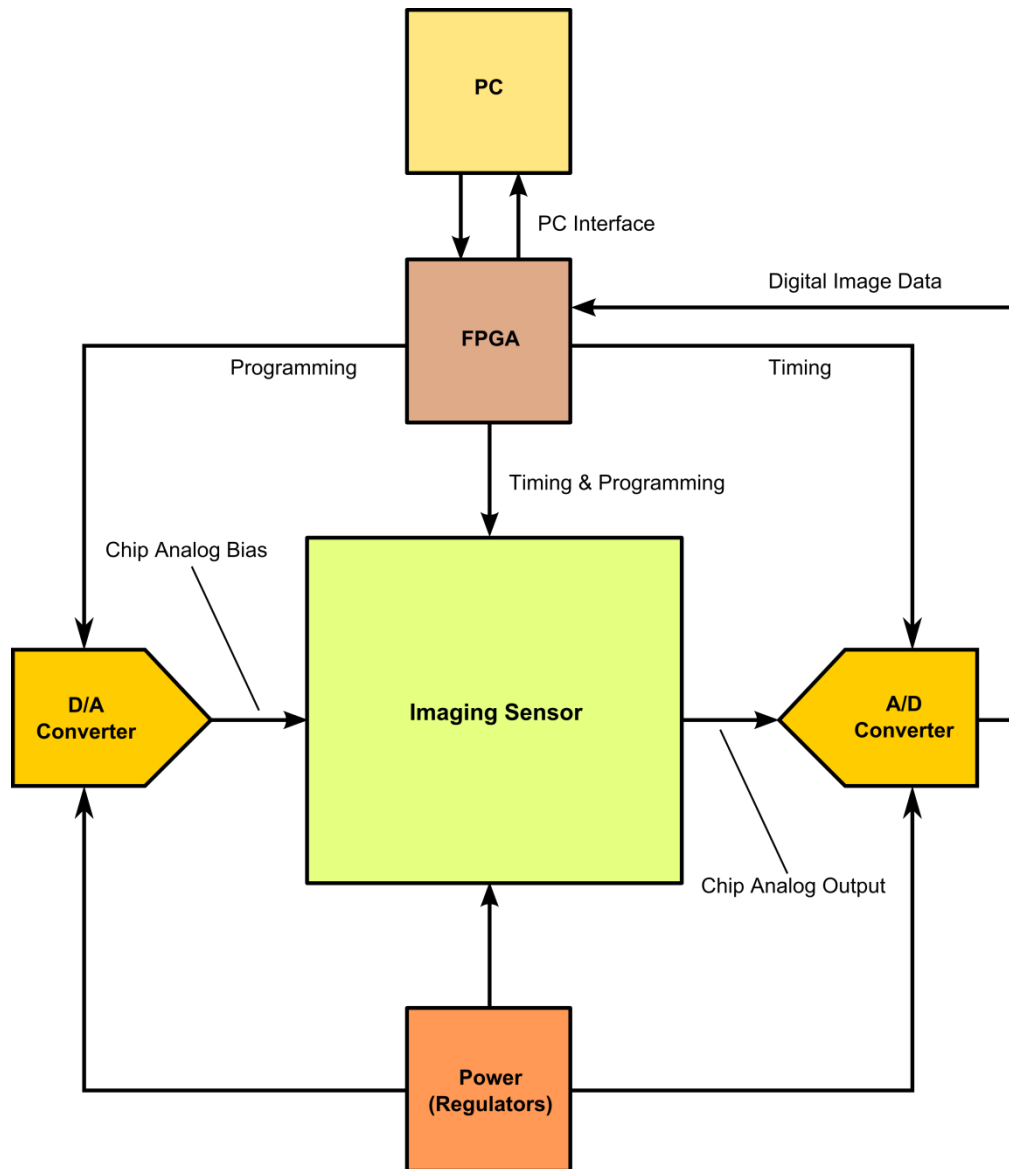


Figure 3.4: Block diagram of the test setup, which is used in testing 160x120 low-cost sensor chips.

Figure 3.5 shows an image of the testing environment that is used for imaging and performance measurement. The vacuumed dewar encloses the imaging sensor and test electronics. Figure 3.6 shows the NETD distribution where the peak NETD measurement is 279 mK with F/1.0 optics. The total power dissipation of 50 mW at 30 fps frame rate is obtained. Thus, the test results show that implemented revisions are effective in increasing the performance.

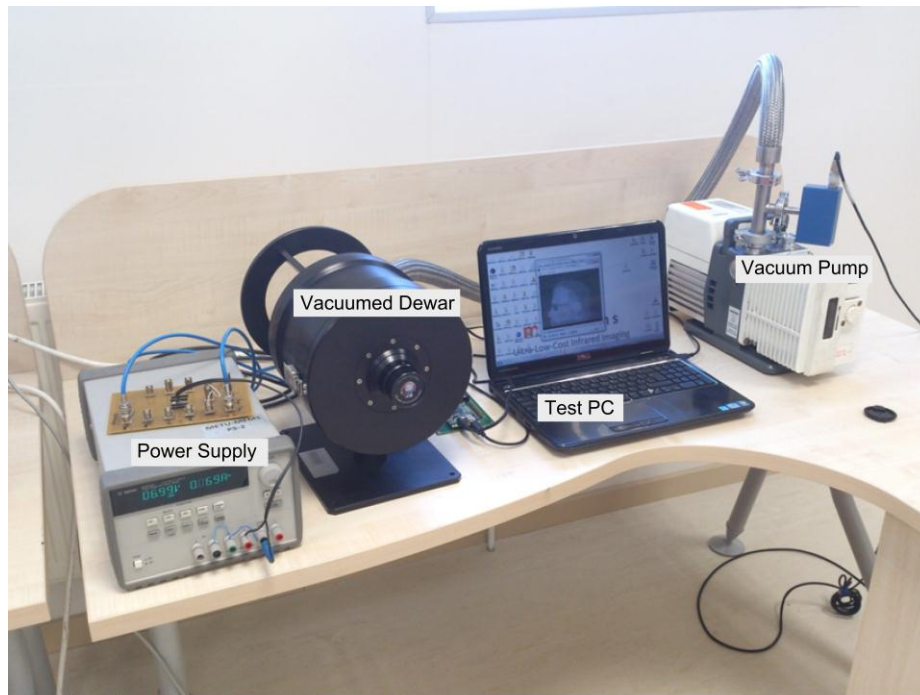


Figure 3.5: An image of a test setup used in imaging and performance measurement.

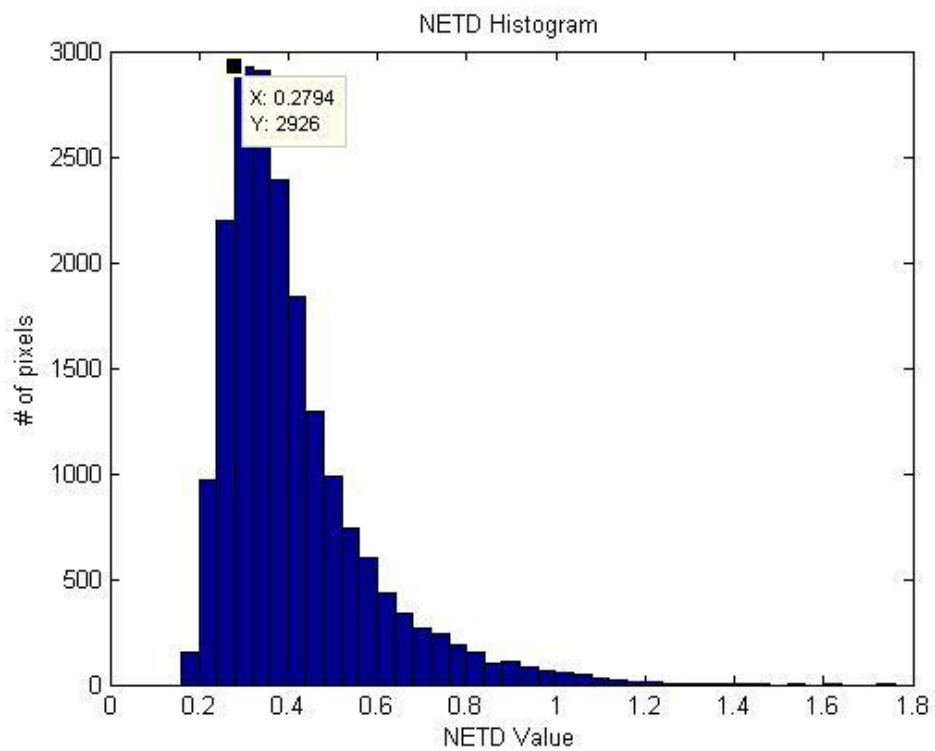


Figure 3.6: Measured NETD histogram for the first design revision with F/1.0 optics

Figure 3.7 shows an image obtained by the sensor. In the images, the impact of the RTS noise on the detectors can be observed as salt and pepper type features. The most prominent feature that degrades the image quality is the vertical line noise or namely the column noise. Figure 3.8 shows the average noise distribution over the array as an image that reveals the column noise impact. In the image shown in Figure 3.9, column noise is decreased by applying the median filtering technique on the still image.

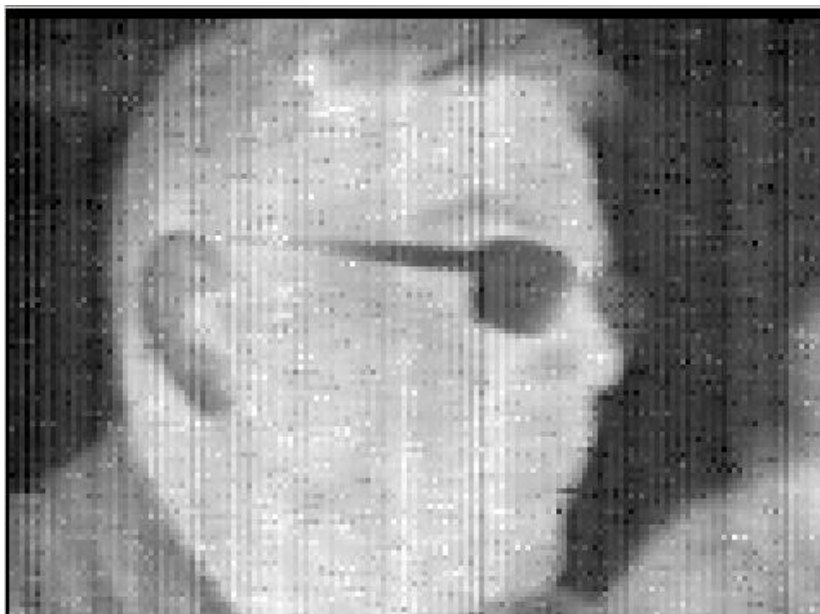


Figure 3.7: A thermal image obtained after the first design revision of the 160x120 low-cost sensor.

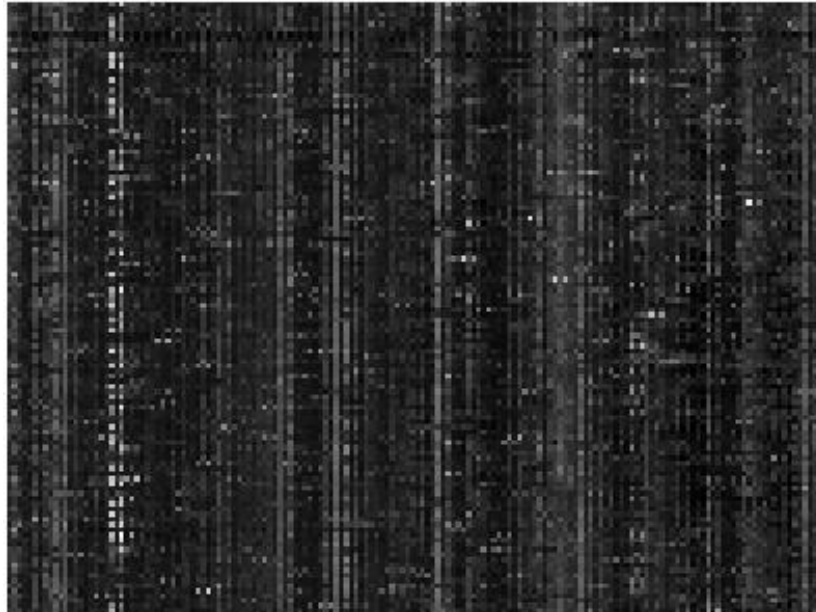


Figure 3.8: Average image noise over the array for the first design revision of the 160x120 low-cost sensor.



Figure 3.9: Another sample image where the column noise is decreased by using median filtering technique.

3.3. Second Design Revision for 160x120 Low-Cost Sensor

This section introduces the second design revision, which is made on the low-cost 160x120 70 μm pixel pitch FPAs. First design revision of the sensor brought a performance increase. Specifically, noise performance of the readout is improved with the decreased power dissipation as shown in Section 3.2.2.

The second design revision also targets the performance decrease due to the noise. The most evident performance flaw observed in the older sensors is the column noise. The RTS type noise mechanism is the column-wise noise dominating factor due to the used referencing method. In this revision, the reference signal generation scheme is changed, in order to decrease the impact of RTS type noise. By that way, column noise is greatly reduced.

The tests of fabricated dies are conducted using test setup that is presented in Section 3.2.2. Figure 3.10 shows the NETD histogram for this revised design. Measured peak NETD value is found to be 280 mK with F/1.0 optics.

It is observed from the chip output signal that vertical column noise is largely eliminated when it is compared to the test results of previous designs. Figure 3.11 shows the average noise distribution along the array. The average noise distribution is obtained by averaging 64 consecutive frames. Figure 3.12 shows the outdoor thermal images that are obtained using the sensor.

In the tests there are two observations have been made as the side effects of the developed reference signal generation scheme. These are the detector voltage drift, and the vertical noise. Voltage drift is caused by the temperature variations of FPA chip. Vertical noise is caused by the common mode noise that is injected into the detector front-end. In order to decrease the temperature drift, the sensor array chip is mounted on a thermoelectric cooler (TEC), which supplies a constant temperature environment. Common mode noise is reduced by careful design of test setup electronics.

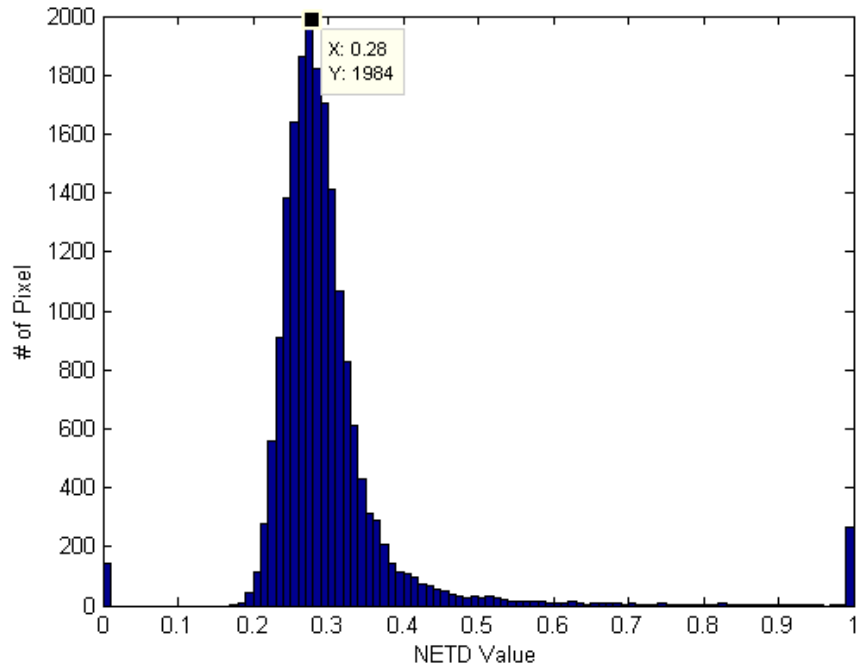


Figure 3.10: Measured NETD histogram for the second design revision with F/1.0 optics.

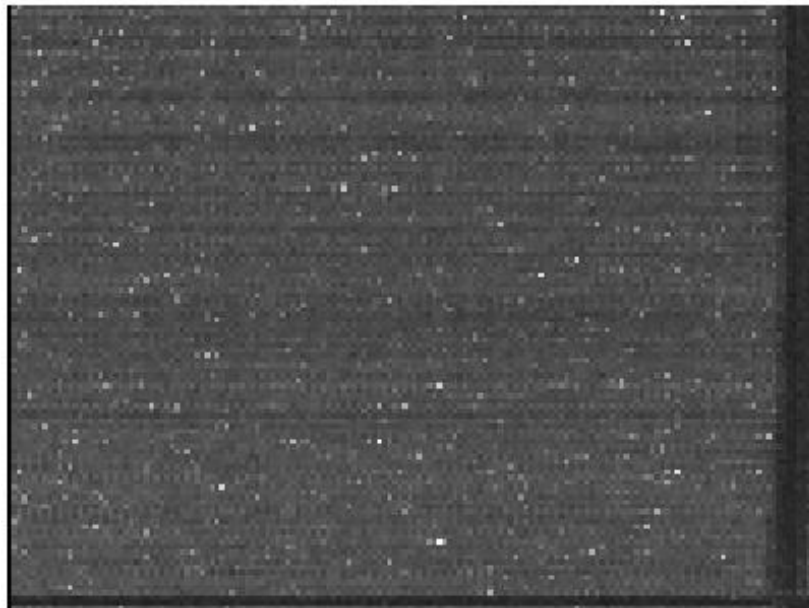


Figure 3.11: Average image noise for the second design revision of the 160x120 low-cost sensor. The noise is averaged over 64 frames.



(a)



(b)

Figure 3.12: Outdoor images obtained after the second design revision of the 160x120 low-cost sensor. (a) An image of recently driven cars (b) An image of humans along the outdoor elements.

3.4. Third Design Revision for 160x120 Low-Cost Sensor

This section introduces the third design revision of first generation low-cost microbolometer sensors. The second revision targeted the vertical column noise, which has a great impact on image data. This modification eliminated the vertical noise largely. On the other hand, temperature drift and increased horizontal line noise are observed as drawbacks after the revision.

Third design revision is intended to alleviate system noise effects and temperature drift problem. Reference signal of the sensor is effective in cancelling the temperature variations effects and common mode noise. In the third design revision, multiple reference signals are generated on the sensor and they are averaged in order to decrease the common noise generated by individual reference signals.

The tests of the revised design are conducted using the setup that is introduced Section 3.2.2. Image is obtained from the sensor array without infrared response. Infrared imaging can be possible after the MEMS post-processing.

Figure 3.13 shows the average noise distribution over the array, which is obtained by averaging 64 frames. It can be observed that, both vertical noise and horizontal noise is not present in the image output. The white dots on the image indicate the pixels with higher noise contribution. Additionally, no voltage drift occurred in the detector signal with the changing temperature. Figure 3.14 shows the input referred pixel noise histogram. Input referred noise includes both the pixel noise and the readout noise. The measured peak input referred noise for the pixels is found to be $12.5 \mu\text{V}_{\text{RMS}}$.



Figure 3.13: Average image noise over the array for the third design revision of the 160x120 low-cost sensor. The noise is averaged over 64 frames.

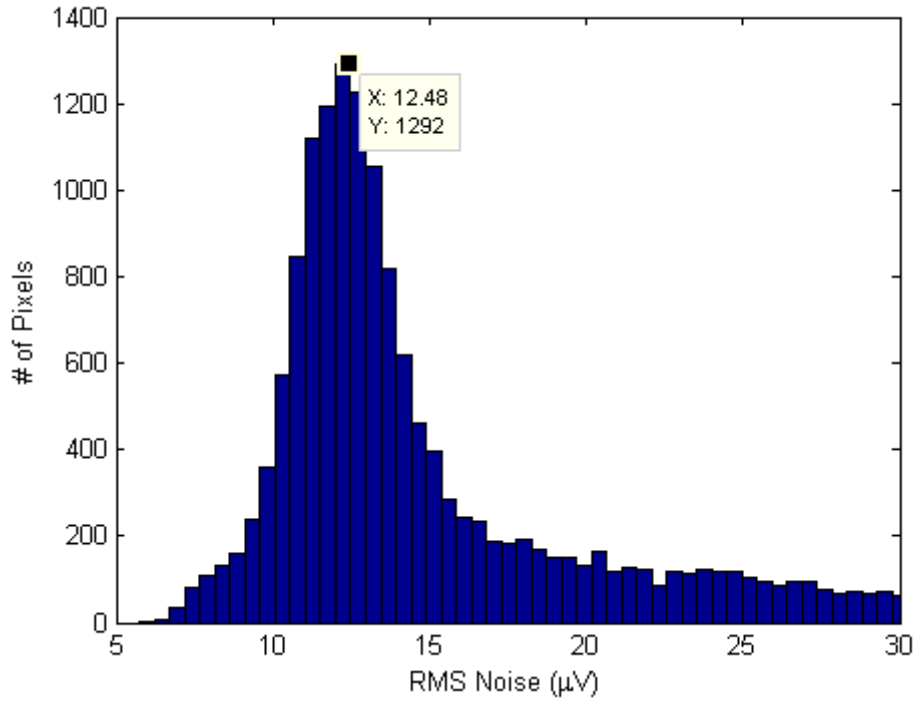


Figure 3.14: Pixel and readout combined input referred noise histogram for the third design revision of the 160x120 low-cost sensor.

3.5. Summary of Revisions

In this chapter, three design revisions of 70 μm pixel pitch 160x120 low-cost microbolometer arrays are presented. Each revision is tested after their CMOS fabrication. Table 3.2 gives a comparison for three revisions.

The improved microbolometer arrays explained in this Chapter are utilized in the miniature camera that is developed in scope of another thesis [26].

Table 3.2: Test result comparison of three design revisions.

	Previous Work [25]	First Design Revision	Second Design Revision	Third Design Revision
Readout Power Dissipation	High	Medium	Medium	Medium
Noise Characteristic	High column noise	High column noise	Row noise	No column or row noise
Temperature Stability	Good	Good	Poor	Good
System Noise Immunity	Good	Good	Poor	Medium
Measured Peak NETD Performance (F/1.0 Optics)	350 mK	280 mK	280 mK	Will be measured after Post-CMOS processing.

CHAPTER 4

DEVELOPMENT OF SECOND GENERATION LOW-COST INFRARED SENSORS

In order to develop small and portable infrared camera systems, the dimensions of the infrared sensor arrays needed to be decreased. Smaller sensor arrays have reduced cost-per-die and they comply with smaller optics. From that point, in the second generation low-cost infrared sensors pixel pitch is decreased to 50 μm which was 70 μm in the first generation sensors. This chapter explains the development process of second generation low-cost infrared sensors with 50 μm pixel pitches.

Size reduction in the pixel has many challenges. The total area that captures the infrared light decreases with the decreasing pitch. The smaller pixel means, shorter support arms, which decreases the thermal isolation. Section 4.1 explains the design process of the pixel parameters for 50 μm low-cost sensor pixel. Pixel is optimized without degrading the performance that is obtained in first generation low-cost infrared sensors.

The designed pixel is simulated in order to assess its performance. Section 4.2 presents the simulation results for the pixel. Simulations include electrical, thermal, and optical characterizations. Section 4.3 shows the test results of the pixel developed throughout this chapter. Sensor FPA tests are explained along the single-pixel tests. Finally, Section 4.4 concludes the chapter by summarizing the design process and tests of second generation low-cost infrared sensors.

4.1. Pixel Optimization and Design

This section explains the optimization second generation low-cost sensor pixel. Section 4.1.1 explains the optimization of detector diode number. Section 4.1.2 explains the optimization calculations of the pixel pitch. Finally, Section 4.1.3 presents the CMOS layout of designed pixel.

4.1.1. Diode Number Optimization

Diode is the temperature sensing element that is used in low-cost infrared sensors. Number of serially connected diodes has a direct effect on detector performance. Each diode added to the detector circuit increase the overall temperature sensitivity linearly. The main limiting factor in increasing the diode number is the voltage headroom. A diode has a drop of nearly 0.8V in the CMOS process that is used in the fabrication of low-cost infrared sensors.

In the second generation low-cost sensors, diode number is selected to be 5, which was 4 in the first generation low-cost sensors. Figure 4.1 shows the overall detector circuit with voltage drops. Detector circuit consists of serially connected detector diodes and a biasing current source. Overall circuit is biased with 5V and cannot be increased further due to the process limit. Total voltage drop on detector diodes is 4V and the remaining 1V drops on the current source. Increasing diode number further decreases the voltage drop on current source and makes it inoperable.

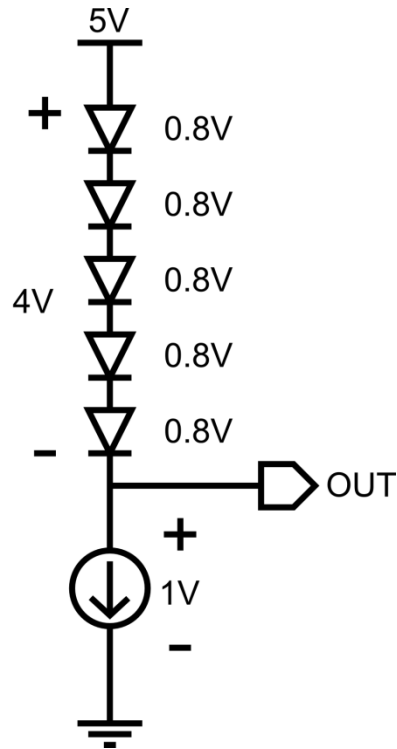


Figure 4.1: Second generation low-cost sensor detector circuit along the DC voltage drops.

4.1.2. Pixel Pitch Optimization

Figure 4.3 shows the shape of the low-cost microbolometer pixel from the top view. The pixel consists of a body that is suspended on arms. The pixel body contains the detector diodes and works as a light absorber. Diodes in the pixel body need to be connected to the circuits. Support arms establish electrical connection of detector diodes while ensuring the mechanical stability of the structure. Polysilicon is used as the electrical interconnect layer because of its low thermal conductance, which increases the detector responsivity. The gap between body, arms, and the wall works as a thermal isolator and provides etch opening for the Post-CMOS MEMS processes.

The main goal of the optimization process is reducing the pixel size without degrading the performance that is achieved in the first generation sensors. This can be done by changing other parameters. As explained in Section 4.1.1, diode number is selected to be 5, which is limited by the electronics. Arm width is selected to be $1.5 \mu\text{m}$ in this design according to the MEMS process limit. Figure 4.2 shows how pixel pitch affects the performance for the different diode number and arm width parameters. Blue line is drawn for first generation pixels while red line is drawn for second generation pixels. The performance of first generation $70 \mu\text{m}$ pixels is achieved at $50 \mu\text{m}$ pixel pitch with newly designed parameters. From that point, pixel pitch for second generation sensors is selected to be $50 \mu\text{m}$. Table 4.1 presents design parameters for the second generation pixel.

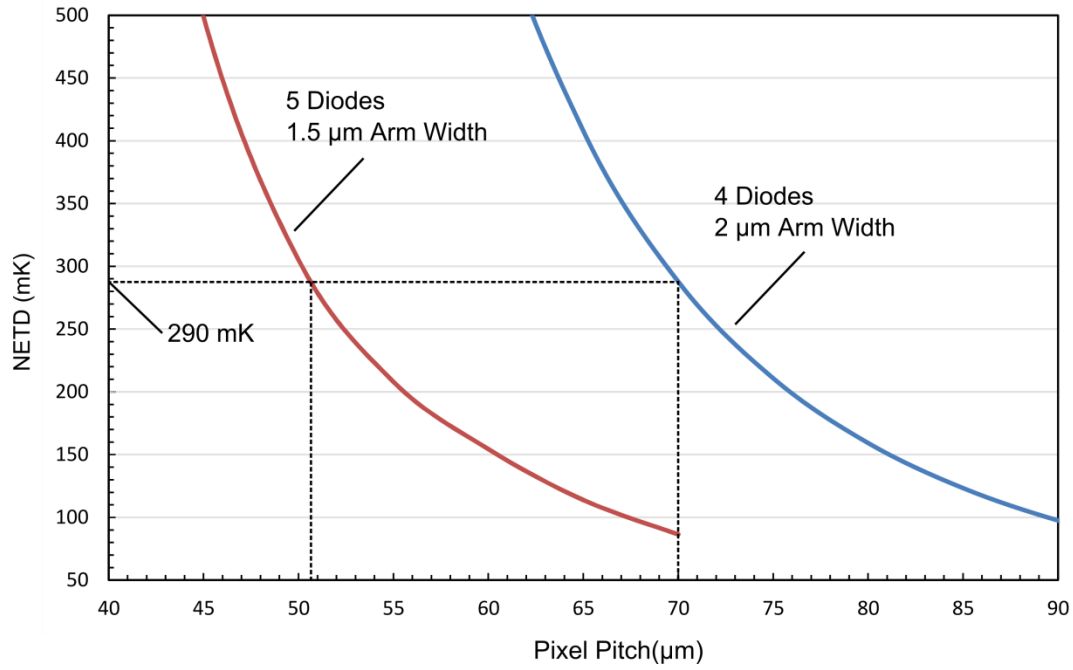


Figure 4.2: NETD vs. pixel pitch for two design parameter configurations. Blue line is drawn for first generation sensor pixels while red line is drawn for second generation pixels. Performance match is obtained by using 50 μm in the second generation design.

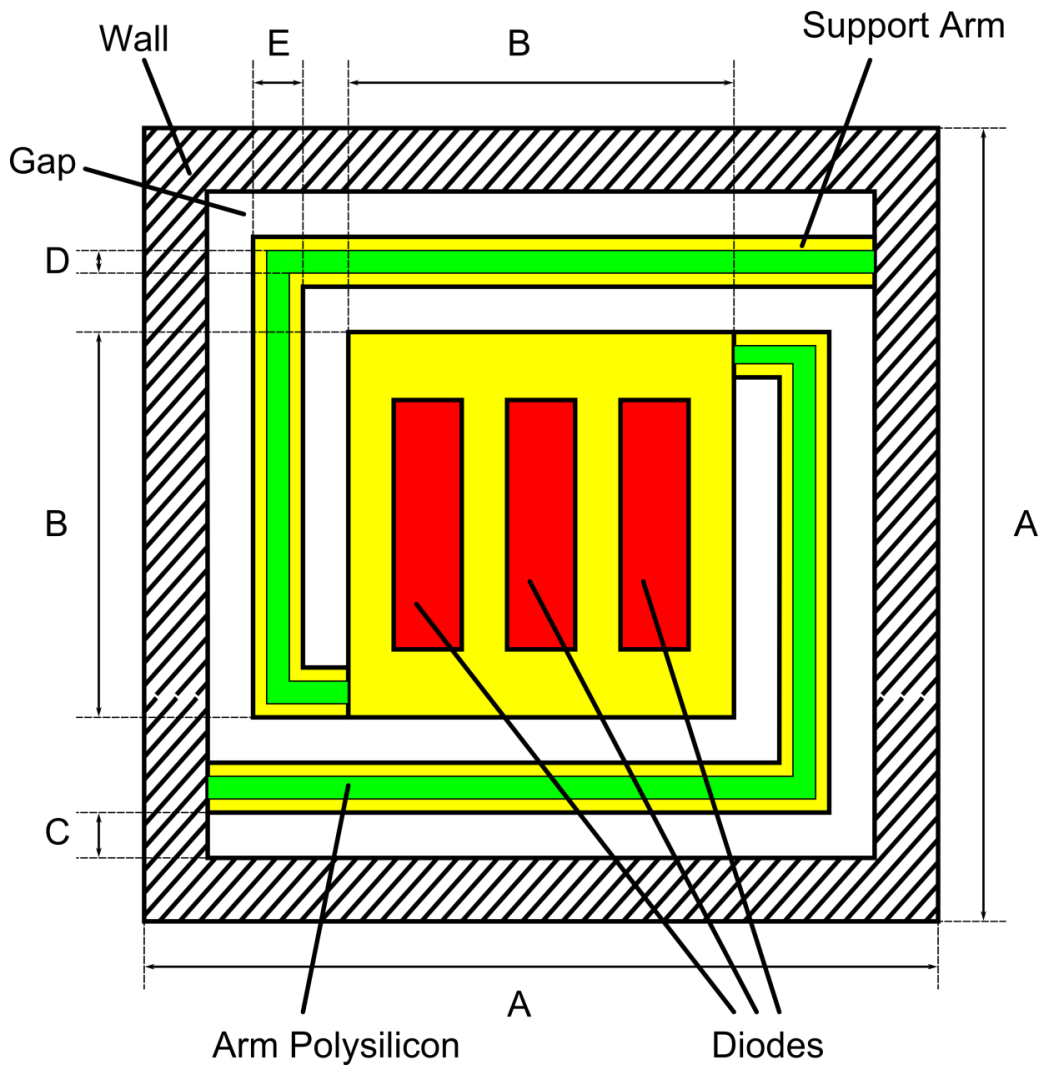


Figure 4.3: Simplified model of the low-cost microbolometer pixel.

Table 4.1: Design parameters for 50 μm pixel that is shown in Figure 4.3.

Dimension Parameter	50- μm Detector Pixel
Pixel Pitch (A)	50 μm
Pixel Body Width (B)	34 μm
Etch Gap (C)	1.5 μm
Polysilicon Interconnect Width (D)	0.5 μm
Support Arm Width (E)	1.5 μm

4.1.3. Pixel Layout Design and Cross Section

Figure 4.4 shows the CMOS layout of designed pixel according to the optimized parameters. The pixel body includes 6 diode devices and 5 of them are intact within the detector circuit. In future, diode number of detector circuit can be increased to 6 by a simple, cost effective design revision. Figure 4.5 shows the cross section of pixel along the CMOS layer thicknesses.

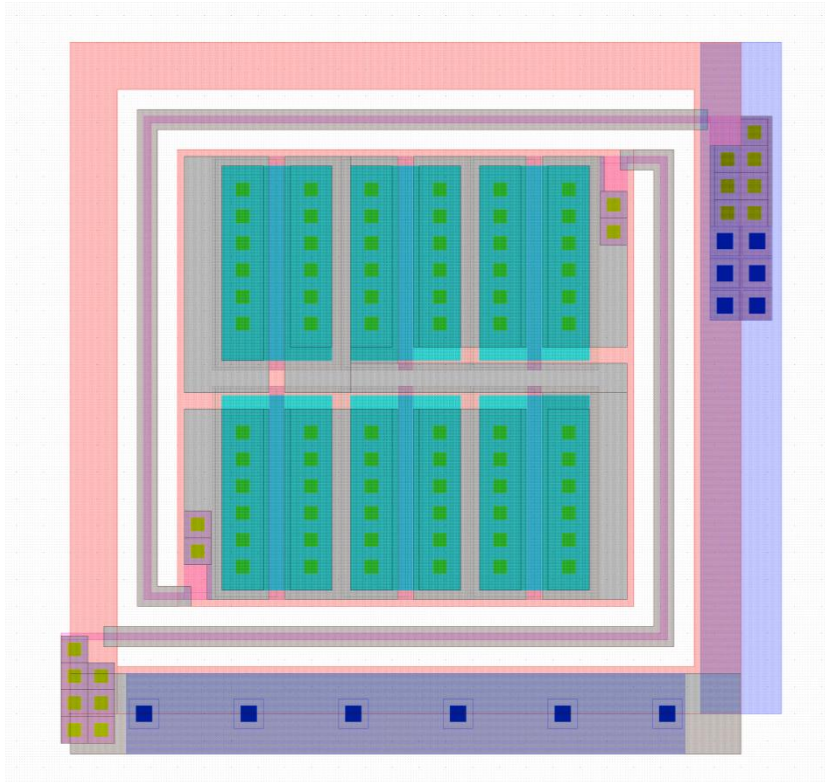


Figure 4.4: Layout of the designed pixel.

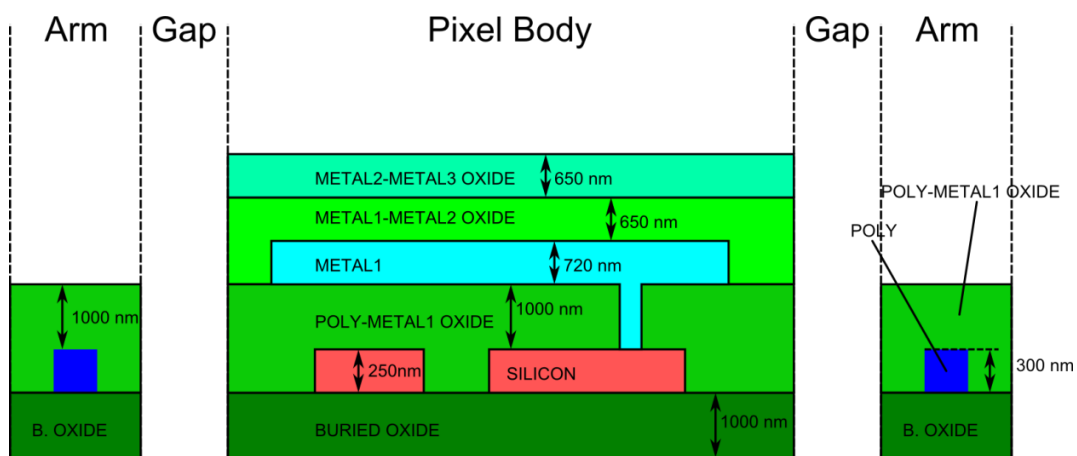


Figure 4.5: Cross sectional view of the designed pixel.

4.2. Pixel Simulations

This section presents the simulation results for second generation detector pixels. Sections 4.2.1 through 4.2.3 show the simulations to find current-voltage (I-V) curve, temperature sensitivity (TC) and noise floor parameters. Section 4.2.4 gives the results of thermal simulations where the FEM simulator is employed. Section 4.2.5 explains the absorption calculations that are conducted by using Cascaded Transmission Line (CTL) method.

4.2.1. Electrical Simulation

In order to obtain current-voltage (I-V) characteristics, detector is simulated electrically using SPICE. Figure 4.6 shows the detector electrical model that is used in the simulations. Pixel model consists of serially connected 5 detector diodes and parasitic arm resistances. Total calculated arm resistance ($2R$) for $50\text{-}\mu\text{m}$ detectors is $9570\ \Omega$. Figure 4.6 shows the simulated I-V curve of $50\ \mu\text{m}$ detector. Detector current shows a sharp turn at the diode turn on voltage, which is about 4V .

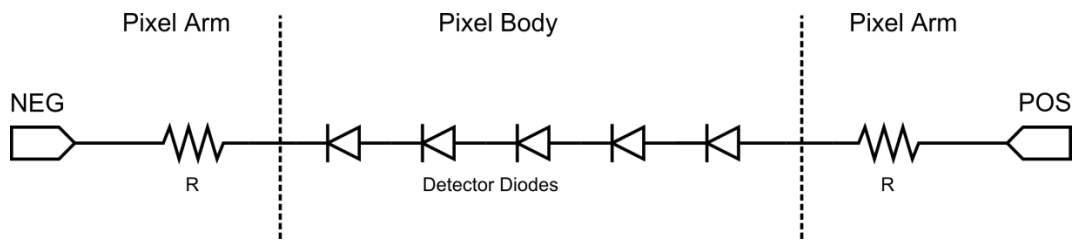


Figure 4.6: Electrical model of the second generation low-cost detectors.

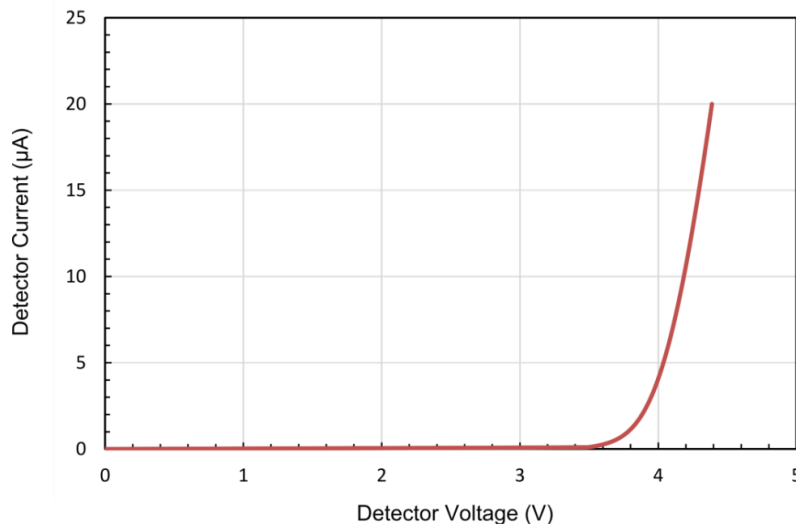


Figure 4.7: Simulated I-V characteristic of the $50\ \mu\text{m}$ detector.

4.2.2. Temperature Sensitivity Simulation

Temperature-voltage characteristics are simulated in order to determine temperature sensitivity (TC) of the diode detectors. Figure 4.8 shows temperature-voltage simulation results of the detector voltage for the second generation low-cost sensor pixel for different bias currents. Extracted TC values are given in the Table 4.2.

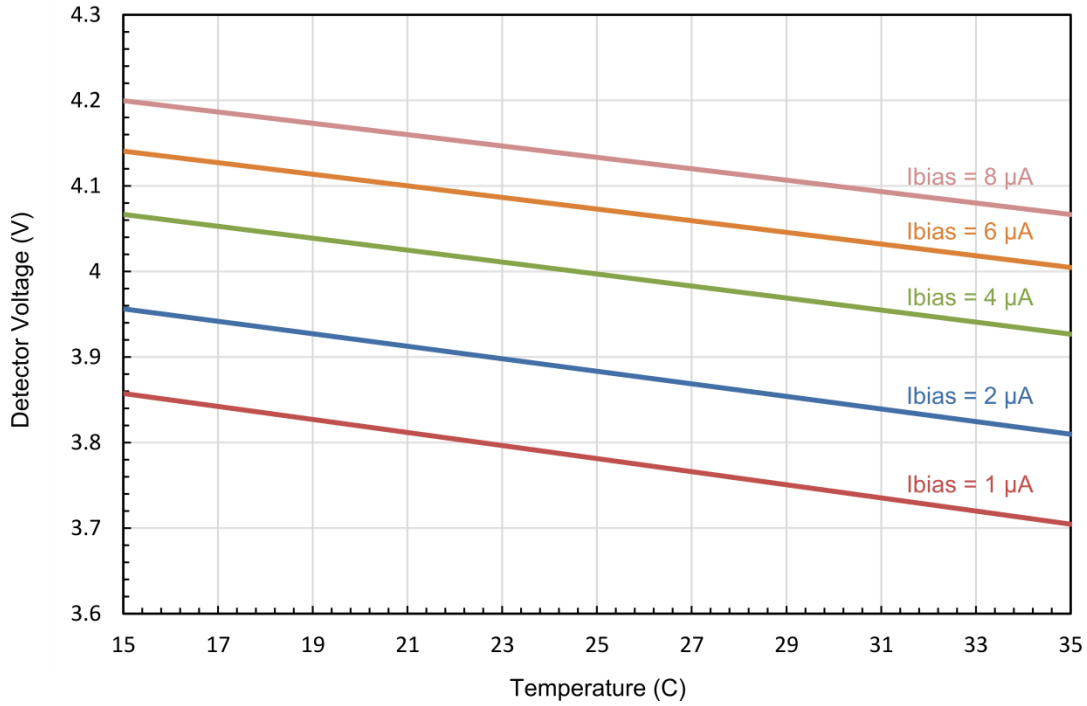


Figure 4.8: Simulated temperature-voltage characteristic of the 50 μm detector.

Table 4.2: Temperature sensitivities of 50 μm diode detector for different bias currents.

Detector Bias Current	Temperature Sensitivity (TC)
1 μA	-7.64 mV/K
2 μA	-7.32 mV/K
4 μA	-7.00 mV/K
6 μA	-6.80 mV/K
8 μA	-6.65 mV/K

4.2.3. Noise Simulation

Voltage noise spectral density of the second generation low-cost sensor is simulated using the SPICE simulator. The electrical model in the Figure 4.6 is used. Simulation includes only shot noise and thermal noise components. Simulation does not include the flicker noise component since the device flicker noise parameters are not provided by the CMOS foundry. Figure 4.9 shows the noise voltage density. Simulated noise floor is found to be $21 \text{ nV}/\sqrt{\text{Hz}}$ at 10 kHz frequency.

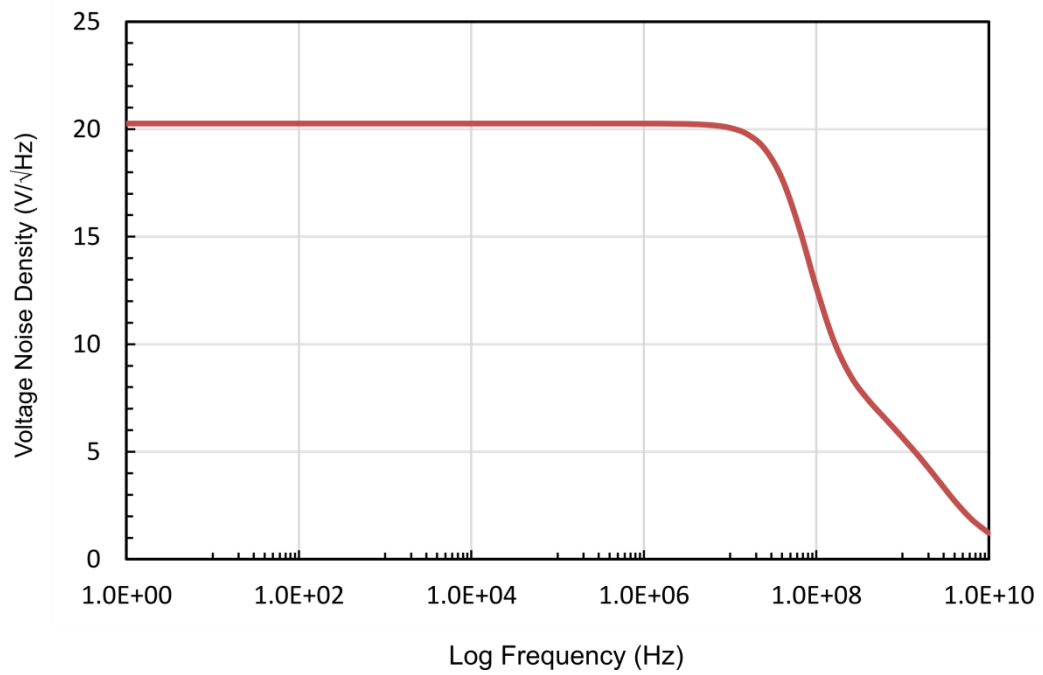


Figure 4.9: Simulated voltage noise spectral density.

4.2.4. Thermal Simulation

Designed pixel is thermally simulated in order to determine the thermal conductance (Gth), thermal capacitance (Cth) and, time constant (τ) of 50- μm pixel. In the simulations, the Coventorware FEM (Finite Element Model) simulator software is employed. Figure 4.10 shows the simulated temperature change against time for 3 μW applied heating power. A curve is fitted on to the simulated data points, in order to obtain thermal parameters.

Table 4.3 presents the extracted thermal conductance (Gth), thermal capacitance (Cth), and time constant data (τ). Figure 4.11 shows the temperature profile along the pixel after 0.8 seconds of heating.

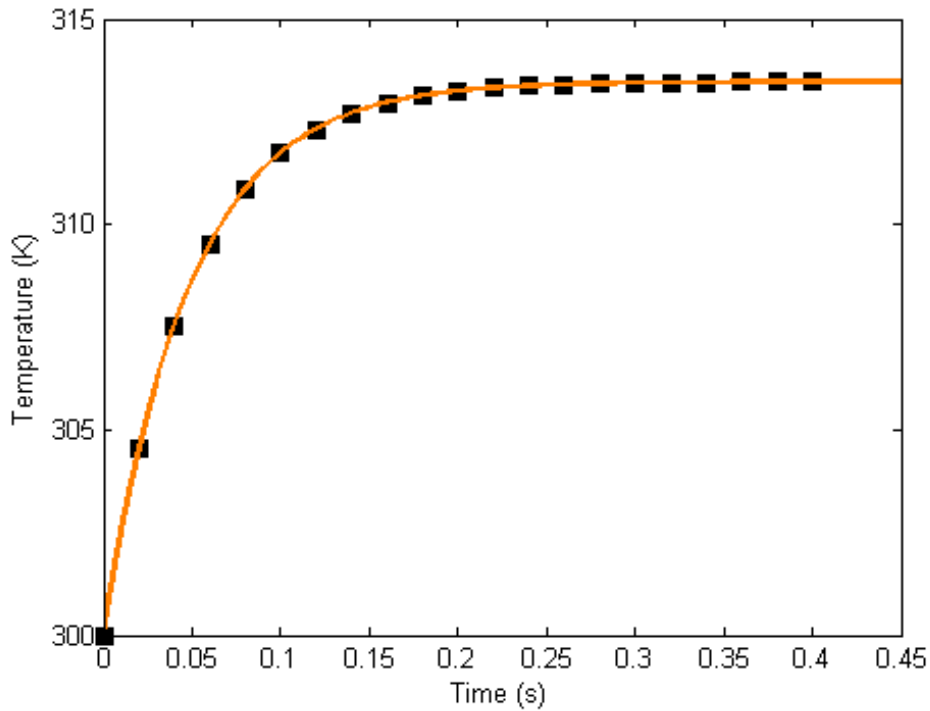


Figure 4.10: Simulated temperature curve of the 50- μm detector for 3 μW applied power. Black squares indicate the simulated data points while orange line indicates the fitted curve.

Table 4.3: Simulated thermal parameters for designed pixel.

Thermal Conductance (Gth)	Thermal Capacitance (Cth)	Time Constant (τ)
222 nW/K	11 nJ/K	48.8 ms

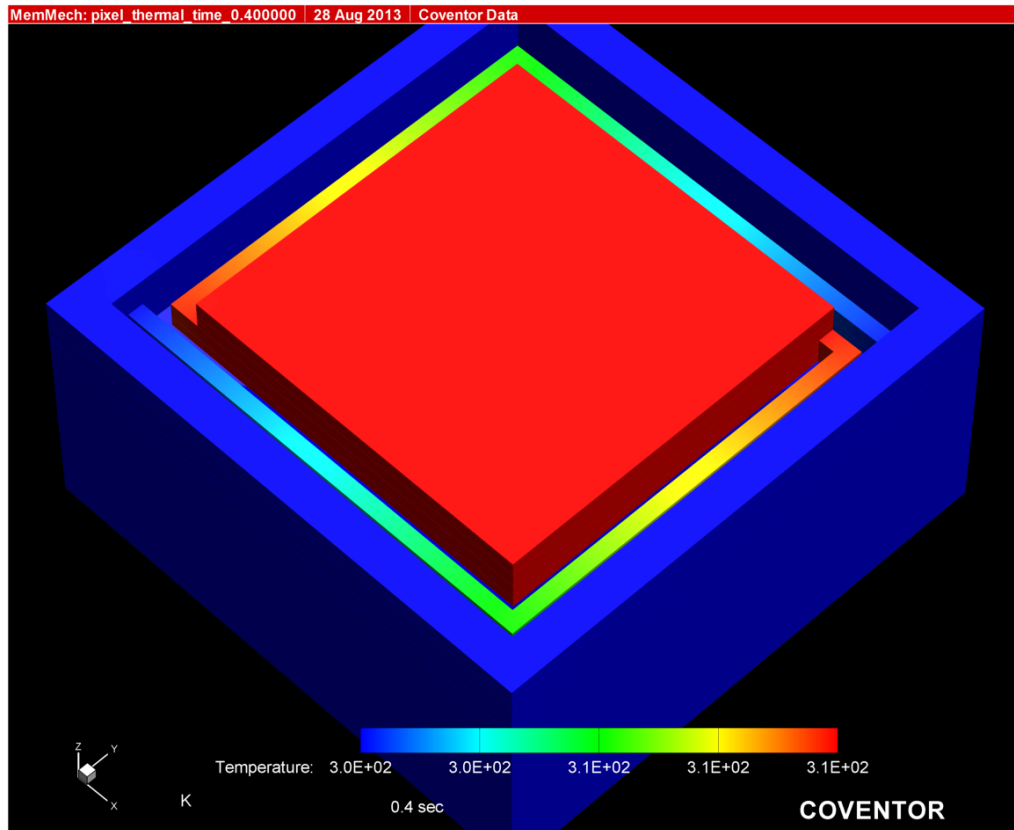
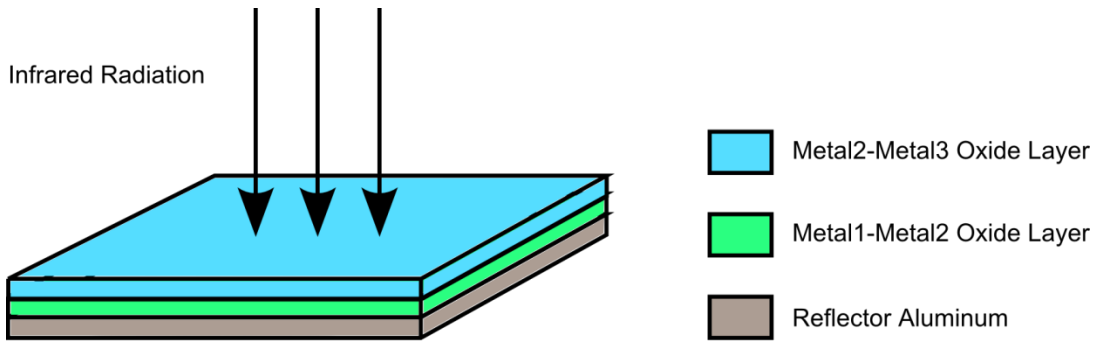


Figure 4.11: Simulated temperature distribution along the pixel after 0.4 seconds of heating.

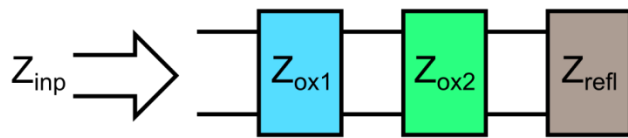
4.2.5. Optical Simulation

The absorption of the designed pixel is determined with optical simulation. In optical simulation Cascaded Transmission Line (CTL) method is used [41, 42]. In CTL method, pixel is modeled as a transmission line where the pixel layers are impedance elements.

Figure 4.12 shows the modeling of low-cost microbolometer pixel according to the CTL method. Absorbing region of the pixel consists of two CMOS oxide layers and a reflector aluminum layer as shown in Figure 4.12(a). Oxide layers are used as absorbing bodies and aluminum layer is used as a reflector in order to increase the amount of absorbed light. Layers are modeled as in Figure 4.12(b). Figure 4.13 shows the simulated spectral absorption for 7-14 μm wavelength range. Simulated average absorption is found to be 77 % for second generation low-cost sensor pixels.



(a)



(b)

Figure 4.12: (a) Pixel absorber physical model. (b) Transmission line model of the absorber layers [41].

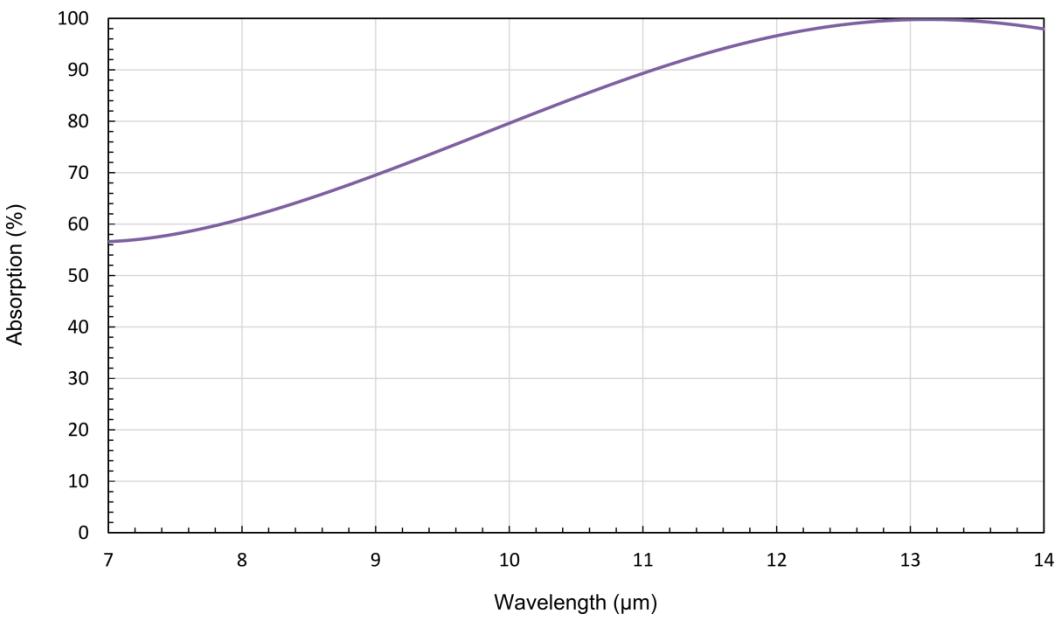


Figure 4.13: Simulated absorption curve. Average absorption is found to be 77 % within the range.

4.3. Test Results

This section the test results of the second generation low-cost infrared sensors. Section 4.3.1 presents the results of single pixel I-V tests and Section 4.3.2 presents the results of the FPA tests.

4.3.1. Single Pixel I-V Test

I-V curve of the detector is obtained using the Agilent B1500A Semiconductor Parameter Analyzer. When measuring the I-V curve, bias current is swept and detector voltage is observed. Figure 4.14 shows the I-V curve obtained from the 50 μm detector and Table 4.4 gives the fitted diode parameters.

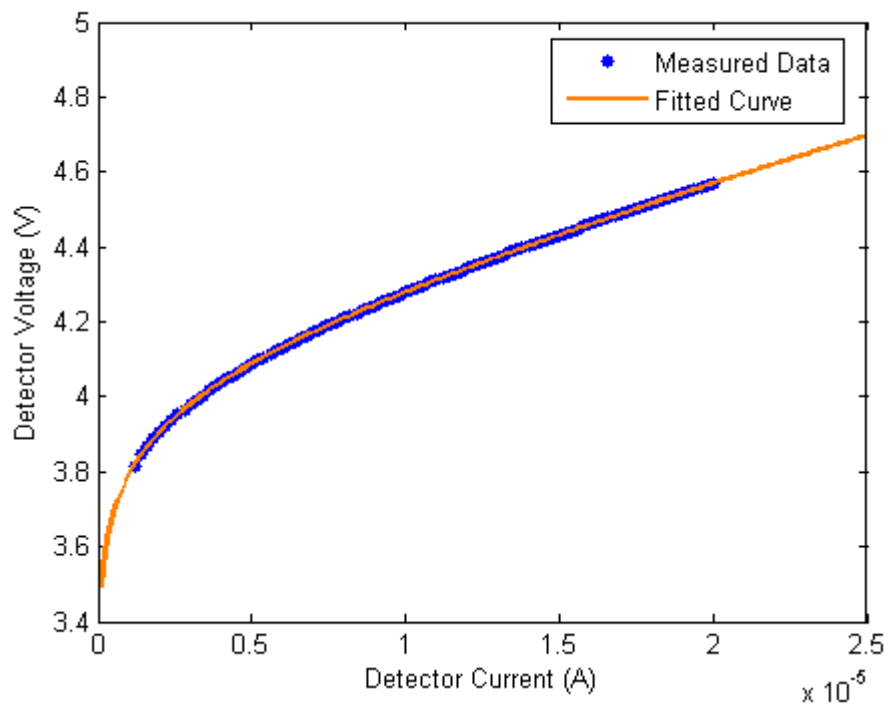


Figure 4.14: Measured I-V data with the fitted curve for 50 μm detector. Fitting is done over 200 data points.

Table 4.4: Extracted parameters from the measured I-V curve

Parameter	Value
Ideality Factor (n)	1.04
Reverse Saturation Current (I_s)	6.6×10^{-19} A
Arm Resistance (R)	19665 Ω

4.3.2. FPA Sensor Tests

The second generation 50 μm detector pixels are utilized in a QCIF (160x120) sensor array, which is recently developed by MikroSens [43]. Detectors are tested for noise using the sensor FPA integrated readout electronics. Figure 4.15 shows the pixel noise histogram. The measured peak input referred noise for the pixels is found to be $9.8 \mu\text{V}_{\text{RMS}}$. Infrared imaging could be possible after MEMS processing of the chip

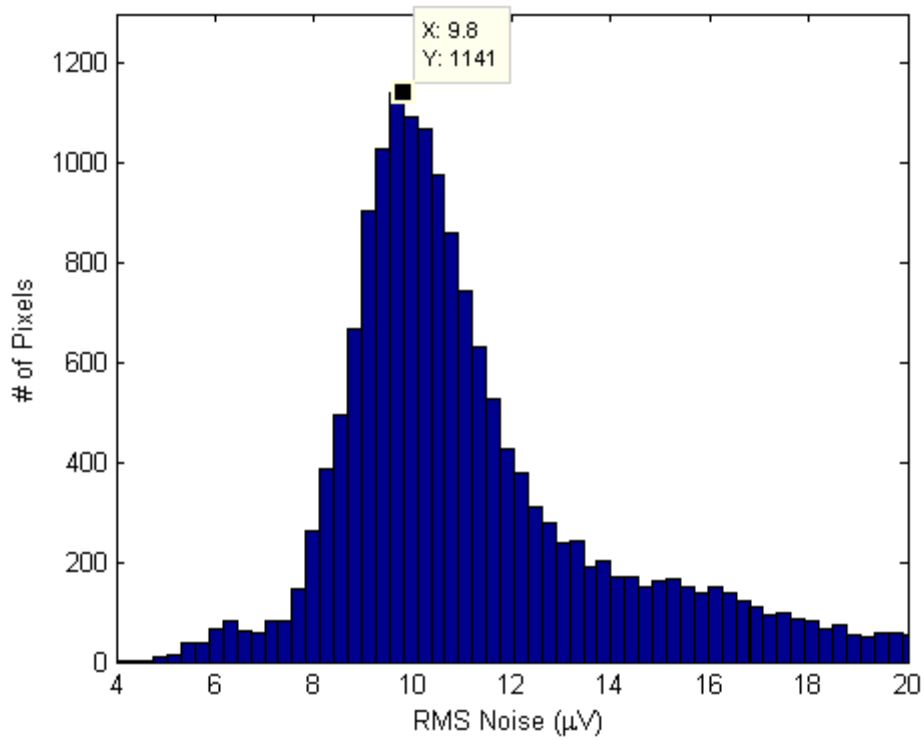


Figure 4.15: Pixel and readout combined input referred noise histogram for 50 μm pixels utilized in a sensor FPA.

4.4. Conclusion

This chapter explained the development process of second generation low-cost infrared sensor pixel. In the second generation design, pixel pitch is reduced to 50 μm from 70 μm without degrading the performance. The pixel is designed to have 50 μm pitch, 1.5 μm arm length and 5 detector diodes. The expected NETD is determined as 290 mK.

The designed pixel is simulated electrically in order to obtain I-V characteristic, temperature sensitivity (TC) and noise parameters. The thermal parameters are simulated using Coventorware Finite Element Method (FEM) simulator and thermal conductance (Gth) is found as 222 nW/K. Absorption is also simulated using Cascaded Transmission Line (CTL) method and found as 77 % within the 7-14 μm wavelength range

Designed 50 μm pixels are utilized within an FPA chip, which has QCIF (160x120) resolution. Compared to first generation FPA designs, the second generation FPA has improved features such as analog output buffer, 3.3V digital pads and smaller die size.

Lastly, implemented pixels are tested. I-V curve of the pixel is obtained and electrical parameters of the detector are extracted by curve fitting. Next, the second generation sensor FPA is characterized. The peak input referred noise of pixels is found to be 9.8 μV_{RMS} including the readout electronics.

CHAPTER 5

CONCLUSIONS AND FUTURE WORK

The research conducted in scope of this study involves the detailed characterization of low-cost infrared detectors and development of sensor electronics and pixels with improved performance figures.

The major achievements in this study can be listed as follows:

1. Previously developed 70 μm pixel is characterized with numerous tests to better understand the nature of low-cost infrared detector. I-V curve is obtained and electrical parameters are extracted. Tests continued with the thermal characterizations to determine temperature sensitivity (TC) and the thermal conductance (Gth). Pixel is optically characterized using Fourier Transform Infrared Spectroscopy (FTIR) method and average absorption is found 77 % for 7-14 μm wavelength range.
2. Test setup electronics are developed in order to characterize the detector noise. With that setup, diode detectors are biased and their noise is amplified. Noise tests of the detectors are conducted in frequency domain and time domain. 4 set of sample detectors are measured in detail and it is observed that the RMS noises values are in a range from 6.6 μV_{RMS} to 45 μV_{RMS} , which is dominated by the Random Telegraph Signal (RTS) noise. Time domain tests are conducted in order to further characterize the RTS noise and it is observed that it has a great influence on the overall detector noise and performance. Spectral characteristics of RTS is investigated and it is shown that Lorentzian spectrum in the frequency domain is associated with the RTS level transitions in the time domain.
3. The 160x120 low-cost infrared sensor developed in a previous work is investigated and its drawbacks are studied [25]. New methods to increase imaging performance are implemented and tested. These revisions can be summarized as follows:
 - a. High power dissipation is an unwanted drawback, which degrades the sensor functionality and the performance due to the self-heating as well as increased noise in the system. The power consumed by the opamps is decreased to 25 mW from 132 mW by changing analog readout opamp topologies. An NETD value of 280 mK is measured in imaging tests.
 - b. A column noise issue is observed in the images obtained from previously designed sensors. It is determined that this column noise is caused by the RTS noise transitions in the reference signal. In the second revision, the reference signal scheme is changed. In the tests, it is observed that column noise is decreased at the cost of decreased thermal stability because of the

lack of the reference detectors. In imaging tests, a peak NETD value of 280 mK is measured.

- c. Finally in the third revision, temperature stability is improved together with the decreased column level RTS noise effects and the improved system noise immunity. The peak input referred pixel noise is measured as 12.5 μV_{RMS} in the infrared blind tests.
4. Previously developed low-cost infrared sensor pixels 70 μm pitch are investigated and their drawbacks are studied. The second generation of low-cost infrared sensor pixels is developed with 50 μm pitch. The pixel features are optimized without causing performance degradation as compared to first generation pixels. Simulations have been done in order to determine the performance values. Finally, developed pixel is tested within the FPA. In infrared blind tests, a peak input referred pixel noise is determined as 9.8 μV_{RMS} including the noise of readout electronics.

The future works needed to be studied can be listed as follows:

1. The origin of the RTS noise observed in the characterization test of low-cost infrared detectors should be determined clearly and a new process should be introduced in order to make detectors more noise free.
2. Low-cost infrared sensors should be implemented in another CMOS process in order to decrease feature size and to develop pixels with smaller size.
3. The infrared imaging tests of the 70 μm FPA developed in the third design revision should be done after its Post-CMOS MEMS processing.
4. Developed 50 μm low-cost pixels should be tested after its Post-CMOS MEMS processing.

REFERENCES

- [1] A. Rogalski, “*Infrared Photon Detectors*,” SPIE Press, 1995.
- [2] S. P. Langley, “The Bolometer and Radiant Energy,” *Proceedings of the American Arts*, Vol. 16, 1880.
- [3] R. A. Wood, “Uncooled Thermal Imaging with Monolithic Silicon Focal Planes,” *Proc. of SPIE*, Vol. 2020, 1993.
- [4] T. Breen, N. Butler, M. Kohin, C.A. Marshall, R. Murphy, T. Parker, N. Piscitelli, and R. Silva, “A Summary of Applications of Uncooled Microbolometer Sensors,” *Aerospace Conference*, Vol. 3, no., pp. 361-374, 1999.
- [5] S. Eminoglu, “Uncooled Infrared Focal Plane Arrays with Integrated Readout Circuitry Using MEMS and Standard CMOS Technologies,” Ph.D. Dissertation, Department of Electrical and Electronics Engineering, Middle East Technical University, 2003.
- [6] S. Eminoglu, M. Y. Tanrikulu, D. S. Tezcan, and T. Akin, “A Low-Cost Small Pixel Uncooled Infrared Detector for Large Focal Plane Arrays using a Standard CMOS Process,” *Proc. of SPIE*, Vol. 4721, pp. 111-121, 2002.
- [7] S. Eminoglu, D. S. Sabuncuoglu, M. Y. Tanrikulu, and T. Akin, “Low-Cost Uncooled Infrared Detectors in CMOS Process,” *Sensors and Actuators*, A109, 2003.
- [8] S. Eminoglu, M. Y. Tanrikulu, and T. Akin, “A Low-Cost 128×128 Uncooled Infrared Detector Array in CMOS Process,” *Journal of Microelectromechanical Systems*, Vol. 17, 2008.
- [9] M. Tepegoz, “A Monolithic Readout Circuit for Large Format Uncooled Infrared Detector Focal Plane Arrays,” Ph.D. Dissertation, Department of Electrical and Electronics Engineering, Middle East Technical University, 2010.
- [10] C. Chen, X. Yi, J. Zhang, and B. Xiong, “Micromachined Uncooled IR Bolometer Linear Array Using VO₂ Thin Films,” *International Journal of Infrared and Millimeter Waves*, Vol. 22, 2001.
- [11] Y. H. Han, K. T. Kim, H. J. Shin, S. Moon, and I. H. Choi, “Enhanced Characteristics of an Uncooled Microbolometer Using Vanadium–Tungsten Oxide as a Thermometric Material,” *Applied Physics Letters*, 86, 2005.
- [12] A. Heredia, F. J. De la Hidalga, A. Torres, and A. Jaramillo, “Low Temperature Electrical Properties of a Boron-Doped Amorphous Silicon Bolometer,” *Proc. of The Electrochemical Society*, 2003.

- [13] F. Niklaus, C. Vieider, and H. Jakobsen, "MEMS-Based Uncooled Infrared Bolometer Arrays – A Review," *Proc. of SPIE*, 2007.
- [14] T. Ishikawa, M. Ueno, K. Endo, Y. Nakaki, H. Hata, T. Sone, M. Kimata, and T. Ozeki, "Low-cost 320x240 Uncooled IRFPA Using Conventional Silicon IC Process," *Proc. of SPIE*, Vol. 3698, 1999.
- [15] M. Ueno, Y. Kosasayama, T. Sugino, Y. Nakaki, Y. Fujii, H. Inoue, K. Kama, T. Seto, M. Takeda, and M. Kimata, "640x480 Pixel Uncooled Infrared FPA with SOI Diode Detectors," *Proc. of SPIE*, Vol. 5783, 2005.
- [16] T. Akin, "CMOS Based Thermal Sensors," *Advanced Micro and Nanosystems Vol. 2*, Wiley, 2005.
- [17] M. C. Foote, T. R. Krueger, J. T. Schofield, D. J. McCleese, T. A. McCann, E. W. Jones, and M. R. Dickie "Space science applications of thermopile detector arrays," *Proc. of SPIE*, Vol. 4999, 2003.
- [18] T. Kanno, M. Saga, S. Matsumoto, M. Uchida, N. Tsukamoto, A. Tanaka, S. Itoh, T. Endoh, S. Tohyama, Y. Yamamoto, S. Murashima, N. Fujimoto, and N. Teranishi "Uncooled Infrared Focal Plane Array Having 128 x 128 Thermopile Detector Elements," *Proc. of SPIE*, Vol. 2269, 1994.
- [19] P. W. Kruse, "*Pyroelectric Arrays*" Chapter of: *Uncooled Thermal Imaging Arrays, Systems, and Applications*" SPIE Press, 2001.
- [20] P. Muralt, "Micromachined Infrared Detectors Based on Pyroelectric Thin Films," *Reports on Progress in Physics*, 2001.
- [21] "Turkish Start-Ups Enter Uncooled FPA and ROIC Markets," *Infrared Imaging News*, May 2012.
- [22] E. Alpman, "Development of Low-Cost Uncooled Infrared Detector Arrays in Standard CMOS and SOI-CMOS Processes," M.S. Thesis, Department of Electrical and Electronics Engineering, Middle East Technical University, 2005.
- [23] M. B. Dayanık, "Low-Cost High Performance Infrared Detectors in SOI-CMOS Technology," M.S. Thesis, Department of Electrical and Electronics Engineering, Middle East Technical University, 2007.
- [24] E. İncetürkmen, "A Low-Cost 128x128 Uncooled Infrared Detector Array in A Standard SOI CMOS Technology," M.S. Thesis, Department of Electrical and Electronics Engineering, Middle East Technical University, 2008.
- [25] D. Akçören, "A Low-Cost Uncooled Infrared Detector Array and Its Camera Electronics," M.S. Thesis, Department of Electrical and Electronics Engineering, Middle East Technical University, 2011.
- [26] C. Tüfekçi, "A Camera Electronics for Low-cost Microbolometer Type Infrared Detectors," M.S. Thesis, Department of Electrical and Electronics Engineering, Middle East Technical University, 2012.

- [27] M. Kimata, M. Ueno, M. Takeda, and T. Seto “SOI Diode Uncooled Infrared Focal Plane Arrays,” *Proc. of SPIE*, Vol. 6127, 2006.
- [28] J. D. Vincent, “*Fundamentals of Infrared Detector Operation and Testing*,” Wiley, 1990.
- [29] P. W. Kruse, “*Uncooled Thermal Imaging Arrays, Systems, and Applications*,” SPIE Press, 2001.
- [30] P. W. Kruse and D. D. Skatrud, “*Uncooled Infrared Imaging Arrays and Systems*”, Semiconductor and Semimetals, Vol. 47, Academic Press, 1997.
- [31] P. Griffiths and J. A. de Haseth, “*Fourier Transform Infrared Spectrometry (2nd ed.)*,” Wiley-Blackwell, 2007.
- [32] B. Razavi “*Design of Analog CMOS Integrated Circuits*,” International Edition, 2001.
- [33] T. G. M. Kleinpenning, “1/f noise in p-n junction diodes,” *Journal of Vacuum Science & Technology A: Vacuum, Surfaces, and Films*,” Vol. 3.1, pp 176-182, 1985.
- [34] F. N. Hooge, “1/f Noise Source,” *IEEE Transactions on Electron Devices*, Vol. 41, pp. 1926-1935, 1994.
- [35] P. R. Gray, and R. G. Meyer “*Analysis and Design of Integrated Circuits*,” Wiley, 1992.
- [36] K. H. Lundberg “Noise sources in bulk CMOS,” *Unpublished paper*, 2002
- [37] N. Zanolla, "Characterization and Modeling of Low-Frequency Noise in MOSFETs," Ph.D. Dissertation, European Doctorate Program in Information Technology, University of Bologna, 2009.
- [38] H. D. Xiong, “Low Frequency Noise and Charge Trapping in MOSFETs,” Ph.D. Dissertation, Department of Electrical Engineering, Vanderbilt University, 2004.
- [39] A. Konczakowska, J. Cichosz, and A. Szewczyk, “A New Method for Identification of RTS Noise,” *Technical Sciences*, Vol. 54, No. 4, 2006.
- [40] Texas Instruments, “NE5532 Datasheet,” 2009.
- [41] M. Y. Tanrikulu, F. Civitci, and T. Akin, “A New Method to Estimate the Absorption Coefficient for Uncooled Infrared Detectors,” *Proc. of SPIE*, Vol. 6940, 2008.
- [42] M. Y. Tanrikulu, “An Uncooled Infrared Microbolometer Detector Array Using Surface Micromachined MEMS Technology,” Ph.D. Dissertation, Department of Electrical and Electronics Engineering, Middle East Technical University, 2007.
- [43] MikroSens, “MS1650 Datasheet,” 2012.